FACULTY OF POLYMER TECHNOLOGY

Štefan VOLK

PA66 MATERIAL CARD CREATION IN MOLDEX3D SOFTWARE

Master’s Thesis

Slovenj Gradec, September 2023

FACULTY OF POLYMER TECHNOLOGY

PA66 MATERIAL CARD CREATION IN MOLDEX3D SOFTWARE

Master's Thesis

Student:	Štefan VOLK
Study programme:	Polymer Technology
Mentor:	Prof. Dr. Walter FRIESENBICHLER
Co-mentor:	Prof. Dr. Majda ŽIGON
Work mentor:	M. Mech. Eng. Martin KRAŠČEK

Slovenj Gradec, September 2023

IZJAVA

Podpisani Štefan Volk izjavljam, da:

- je bilo predloženo magistrsko delo opravljeno samostojno pod mentorstvom;
- predloženo magistrsko delo v celoti ali v delih ni bilo predloženo za pridobitev kakršnekoli izobrazbe na drugi fakulteti ali univerzi;
- soglašam z javno dostopnostjo magistrskega dela v knjižnici Fakultete za tehnologijo polimerov v Slovenj Gradcu. Na Fakulteto za tehnologijo polimerov neodplačno, neizključno, prostorsko in časovno neomejeno prenašam pravico shranitve magistrskega dela v elektronski obliki, pravico reproduciranja ter pravico ponuditi magistrsko delo javnosti na svetovnem spletu preko repozitorija DiRROS.

Slovenj Gradec, _____ Podpis: _____

ACKNOWLEDGEMENTS

I am extremely grateful to everyone who has contributed to completing my Master's thesis.

I would like to thank my supervisors, Prof. Dr. Walter Friesenbichler and Prof. Dr. Majda Žigon, for their constant support, expert mentorship, and invaluable advice during my master's thesis research. Their professional guidance has helped me to make my Master's thesis more thorough and comprehensive than I initially imagined.

I am truly grateful to Iskra ISD for allowing me to undertake this research. Also, I would like to thank all my colleagues from the company for their support, especially my work mentor Martin Krašček for his valuable insight, guidance in the field of injection moulding simulation, and encouraging words. Without their collective effort and contribution, the successful completion of this master's thesis would not have been possible.

Lastly, I would like to thank my family, girlfriend Janja, and friends, who have encouraged me during my studies and the completion of my thesis.

SUMMARY

PA66 Material Card Creation in Moldex3D Software

In the master's thesis, the properties of different batches of PA66 GF30 polymer from BADA (Germany) are compared. The material card for this material was created in Moldex3D numerical simulation software. Moreover, the theoretical background of polymers, their characterisation methods, and numerical simulation of injection moulding are presented. The injection moulding machine parameters were used to create an injection moulding simulation, the runner system and the cooling channels from the tool 3D model. The created material card was validated through an injection moulding pressure curve, the product filling pattern, and a comparison of the deformation of the Moldex3D simulation and scanned injection moulded part. The DOE multilevel factorial method was used to analyse how variations in the material parameters affect injection moulding pressure and part deformation.

Keywords:

PA66 GF30, Moldex3D, numerical analysis, material card, polymer characterisation, DOE.

POVZETEK

Izdelava materialne kartice PA66 za programsko okolje Moldex3D

V magistrskem delu smo primerjali termične in mehanske lastnosti različnih šarž materiala PA66 GF30, proizvajalca BADA (Nemčija) ter izdelali materialno kartico za omenjeni material v programskem okolju Moldex3D. Sprva smo predstavili teoretične osnove področja polimerov, metode karakterizacije polimerov ter numerične simulacije injekcijskega brizganja. Pred pričetkom eksperimentalnega dela smo izvedli temeljit pregled literature na izbranih področjih, s katerim smo pridobili bolj celosten vpogled v že obstoječe raziskave ter nadgradili svoje znanje iz teoretičnih osnov našega področja. Po temeljitem pregledu literature smo postavili hipotezo, da bodo razlike mehanskih in termičnih lastnosti med šaržami minimalne. Nadalje smo v prvem delu eksperimentalnega dela primerjali ključne mehanske in termične lastnosti različnih šarž materiala PA66 GF30. Izmerili smo masni in volumski indeks tečenja taline (MFR in MVR), analizirali kemijsko sestavo materiala z uporabo termogravimetrične analize (TGA), določili dinamični E modul in fazni kot s pomočjo dinamične mehanske analize (DMA), izmerili temperaturo toplotnih prehodov, z uporabo diferenčne dinamične kalorimetrije (DSC) izračunali stopnjo kristaliničnosti in izmerili mehanske lastnosti materiala s trgalnim strojem. Uporabili smo tudi princip superpozicije (TTS) na DSC napravi, s katerim smo preučili kako frekvenca in temperatura vplivata na modul elastičnosti in fazni kot. V drugem delu eksperimentalnega dela smo opravili karakterizacijo materialnih lastnosti, ki so ključne za izdelavo materialne kartice v Moldex3D. Za določitev viskoznosti materiala smo uporabili rotacijski in kapilarni reometer. Analizirali smo fazni diagram, ki opisuje zvezo med tlakom, specifičnim volumnom in temperaturo (PVT) ter izvedli meritev kristaliničnosti polimera z uporabo diferenčne dinamične kalorimetrije s temperaturnim moduliranjem (DSC TOPEM). Poleg tega smo opravili meritve toplotne prevodnosti in specifične toplotne kapacitete materiala. Izvedli smo tudi preizkus brizganja vzorčnih kosov z uporabo izbranega PA66 GF30 materiala, v okviru katerega smo izdelali delne brizge izdelkov med postopkom brizganja pridobili tlačne krivulje ter izdelali vzorčne kose. Izdelane vzorčne kose smo nato pregledali z napravo za računalniško tomografijo (CT), ki omogoča natančno skeniranje površine kosov. Del rezultatov meritev (viskoznosti, PVT diagrama ter kristaliničnosti) drugega eksperimentalnega dela smo preoblikovali in prilagodili kot parametre za ustrezen matematični model v Moldex3D. V sodelovanju z ekipo za tehnično podporo iz Moldex3D, smo izdelali materialno kartico za PA66 GF30 material, s trgovskim imenom Badamid A70 GF30 HH E. Za validacijo nove materialne kartice smo izvedli simulacijo brizganja za izbrano štiri gnezdno orodje, pri čemer smo primerjali tlačne krivulje, vzorec polnjenja izdelka in predvidene deformacije iz Moldex3D simulacije s skeniranima kosoma. Izbrano štiri gnezdno orodje je sestavljeno iz dveh gnezd spodnjega in dveh gnezd zgornjega ohišja. Za izboljšanje numerične stabilnosti simulacije brizganja in zmanjšanja potencialnih zapletov z mrežo izdelka, smo 3D modela ohišij poenostavili. V Moldex3D smo uvozili geometrijo hladilnih kanalov, dolivni sistem v obliki krivulj in ustrezna skalirana izdelka iz orodja.

Geometrijo dolivnega sistema smo izdelali neposredno v Moldex3D, s čimer smo lahko določili robni pogoj simetrije. Uporaba robnega pogoja simetrije nam je znatno skrajšala čas izračuna ter omogočila uporabo gostejše mreže. Dimenzije dolivnega sistema smo določili v skladu s 3D modelom orodja. Pri simulaciji brizganja smo uporabili procesne parametre iz izvedenega preizkusa. Z namenom določitve optimalne gostote mreže za analizo deformacij izdelkov, smo preučili konvergence rezultatov deformacij pri uporabi različnih gostot mreže. Pri primerjavi rezultatov skupne deformacije smo uporabili nadomestni material PA66 GF30 Ultramid A218V W30 iz materialne baze Moldex3D. Po analizi skupnih deformacij različnih gostot mrež smo se pri nadaljnjih izračunih odločili za uporabo 0.6 mm goste mreže. Navedene korake smo izvedli z namenom, da zagotovimo zanesljive in natančne rezultate deformacij ter omogočimo kvalitetno nadaljnjo analizo dimenzij izdelkov. Za preverjanje veljavnosti robnega pogoja simetrije smo primerjali rezultate tlačne krivulje brizganja simulacije z uporabljenim robnim pogojem s celotnim štiri gnezdnim dolivnim sistemom izdelka. Analiza je pokazala izjemno usklajenost med tlačnimi krivuljami celotnega dolivnega sistema in polovičnim dolivnim sistemom, kjer smo uporabili robni pogoj simetrije. Nato smo izvedli simulacijo polnjenja izdelka in deformacij po brizganju, pri uporabljeni 0.6 mm gosti mreži z upoštevanim robnim pogojem simetrije ter procesnimi parametri iz izvedenega preizkusa, ki predstavlja pomemben del našega magistrskega dela. Uporabili smo material PA66 GF30 različnih proizvajalcev ter različne primere naše izdelane materialne kartice. Na podlagi rezultatov simulacij smo ustvarili primerjavo tlačnih krivulj, vzorca polnjenja izdelkov ter dimenzije deformiranih izdelkov iz simulacije s skeniranima izdelkoma. Dimenzije izdelkov smo primerjali s pomočjo programskega okolja PolyWorks. Za temeljito analizo vpliva variacij materialnih lastnosti na brizgalni tlak ter deformacijo izdelka smo izvedli več nivojski načrt eksperimenta (DOE). V okviru tega načrta smo temeljito preučili vpliv viskoznosti, toplotne prevodnosti, hitrosti kristalizacije in PVT faznega diagrama. Merilne vrednosti štirih izbranih materialnih lastnosti smo povečali in zmanjšali za izbrane vrednosti koeficientov variacije (CV). Skupno smo izvedli 16 simulacij brizganja in tako uporabili vse možne kombinacije variiranih parametrov. Rezultate Moldex3D simulacije DOE smo interpretirali v programskem okolju za statistično analizo JMP. Primerjava mehanskih in termičnih lastnosti različnih šarž izbranega materiala je potrdila hipotezo, da so razlike med lastnostmi posameznih šarž zanemarljive. Uspešno smo izdelali materialno kartico za PA66 GF30 material. Rezultati Moldex3D simulacije so pokazali ujemajoč vzorec polnjenja izdelka, vendar pa je primerjava tlačnih krivulj razkrila manjšo vrednost tlaka v simulaciji v primerjavi z izmerjenim tlakom pri brizganju. Vzroke za omenjeno odstopanje smo izpostavili v magistrskem delu. Rezultati simulacije deformacij so pokazali podoben trend, kot je bil opažen pri dejanskem izdelku, vendar pa natančne vrednosti in ekstremi niso popolnoma ujemajoči. Rezultati DOE so pokazali, da je viskoznost materiala ključna lastnost pri izračunu brizgalnega tlaka. Kristaliničnost in PVT sta se izkazali kot najbolj vplivni materialni lastnosti pri izračunu deformacije izdelka. Z našo raziskavo smo analizirali natančnost simulacije brizganja, vpliv različnih šarž na termične in mehanske lastnosti polimerov ter vpliv podatkov materialnih lastnosti na rezultate simulacije. Raziskana

področja nam pomagajo pri reševanju in razumevanju problemov, s katerimi se srečujemo pri simulaciji brizganja polimerov. Nobena materialna kartica ne zagotavlja popolne aproksimacije obnašanja materiala v procesu brizganja, kljub temu pa nam simulacije omogočajo dober vpogled v trende deformacij in zanesljiv vpogled v potencialno problematična področja. Te informacije so ključne, saj inženirjem omogočajo preprečitev težav in optimizacijo izdelkov že v fazi razvoja izdelka.

Ključne besede:

PA66 GF30, Moldex3D, numerična analiza, materialna kartica, karakterizacija polimerov, DOE.

TABLE OF CONTENTS

1 INTRODUCTION

Polymer materials, or "plastic materials", as consumers call them, represent a large part of our daily life. They are present almost everywhere, from the automotive, pharmaceutical, food, sports, education, and space industries. Polymers are widely used because they are relatively easy to process, have low density, and have diverse chemical and mechanical properties, which is why they are more frequently used in the automotive industry. They are excellent insulators for electricity and heat, and the production of polymers requires less energy as compared to the production of metals. As a result of these properties, the production of polymer materials continues to grow year by year.

Over the past few decades, we have noticed some of the major issues that are becoming apparent with the use of polymer materials. Degradation, weak resistance to heat, and deformation under load are some of the negative properties of polymers. Due to these weaknesses, the products that are usually on the market are polymer composites.

Polymer composites consist of a polymer matrix, which is reinforced with reinforcement materials and differs in chemical consistency and form to improve the desired material properties according to their area of use. The advantage of adding reinforcements to polymer materials is to improve stiffness, strength, and ductility [1]. Polymer composites are used to improve material properties, but they may cause problems with the recycling of the material. Not all composites are difficult to recycle; some manufacturers even define what proportion of recycled material can be used in production to reduce waste, but some composites prove challenging to recycle.

Due to increased environmental awareness and the significant accumulation of plastic waste, more research is focused on the impact of polymer materials on the environment, from the start of production to plastic waste disposal. The polymer industry is shifting towards environmentally friendly materials, reducing the environmental impact of existing materials on the market and reducing waste. New studies are aimed toward environmentally friendly biopolymers that could replace conventional synthetic materials. However, the process of replacing these with biopolymers is challenging because of the difficulty in achieving similar properties and stability.

Despite the difficulty of replacing commercially used synthetic polymers, we can significantly contribute to preserving our environment by optimising existing processes and reducing waste material. In the production phase, numerical simulations can decrease part failures and predict part response to mechanical loads and environmental impact in the life cycle. No simulation is 100 per cent accurate because of various simplifications in numerical behaviour, material behaviour, and the chosen

boundary conditions. However, with research and development, we are getting closer and closer to the actual material behaviour.

A huge problem we face when setting up a numerical simulation for feasibility analysis is the quality of the material properties in our software database. The numerical simulation of injection moulding (IM) depends on the quality of the material card. The use of low-quality material cards or material replacements can lead to false simulation results or trend direction. Simulation results are highly dependent on boundary conditions.

Another problem is the variation in the composition of each material batch. No batch is the same as the other. For example, the mechanical properties and material flow behaviour could be significantly affected by a slight difference in glass fibre content. Therefore, the company's quality team checks the properties of the supplied material to ensure the material batch does not have a massive effect on the process stability.

In the master's thesis, we aim to investigate and present the comprehensive procedures necessary to develop a good quality IM material card within the numerical simulation software, Moldex3D. In addition, we validate the newly created material card and examine the comparability of different batches of the selected material with each other.

2 THEORETICAL BACKGROUND

2.1 Polymeric Materials

Polymers are macromolecules consisting of long chains of repeating monomer units. One polymer chain can consist of over a hundred monomers joined by a covalent bond. This chemical reaction that binds monomers and later oligomers and polymer chains is called polymerisation [2,3]. Several joined polymer chains with similar chemical structures but not necessarily identical lengths form a polymer material [1]. According to the arrangement of monomers in the polymer chains, polymers are divided into homopolymers and copolymers. Homopolymers are polymers composed of repeating units from a single type of monomer. Hypothetically, homopolymers A-A-A-A-A-A-A can be represented by $–[A]_n-$ where n indicates the number of repeating units which together form a macromolecule. Copolymers are polymers composed of two or more different types of monomers (A, B, C) [3].

Copolymers are divided into the following groups [3]:

- block copolymers (-A-A-A-A-B-B-B-B-),
- alternating copolymers (-A-B-A-B-A-B-A-B-),
- random copolymers (-A-B-A-A-B-B-B).

Polymers existed since the start of life on Earth because polymers are not only synthetical materials but also natural. Natural polymers such as proteins, cellulose, starch, natural rubber, deoxyribonucleic acid (DNA), and ribonucleic acid (RNA) play a critical role in plants' and animals' function, growth, and survival. Synthetic polymers, specifically polyamide 66, will be the focus of our master's thesis. The industry of synthetic polymers began in the nineteenth century with the modification of natural polymers [3].

Polymer materials are functional materials that can be widely used, from housing materials, automotive and aerospace industry to medical applications. Polymers are cheaper than metals because they require lower temperatures for processing, have good chemical and atmospheric corrosion resistance and are very lightweight, which is why they are used in the sports industry and transportation [2]. Also, large varieties of polymers are currently on the market, from standard polymers to more demanding engineering plastics and advanced engineering plastics such as high-temperature thermoplastics.

Polymers can be classified into three groups [1]:

- synthetic polymers (polyethylene, polypropylene, polyamide, etc.),
- natural polymers (cellulose, polysaccharides, enzymes, etc.),
- elastomers (nitrile rubber, butyl rubber, ethylene propylene rubber, etc.).

Synthetic polymers can be classified into two categories [1]:

- thermosets,
- thermoplastics.

Thermosets

Thermosets are rigid polymer materials that, when heated form a high degree of cross-linking. Such parts cannot be remoulded after production[3]. The cross-linked structure in Figure 1 demonstrates that thermosets cannot be recycled even with extremely high temperatures because they do not melt. They are commonly used due to good temperature and chemical resistance, good mechanical properties, and dimensional stability [1]. Some of the most widely used thermosets are epoxy, silicone, polyurethane, and bakelite – phenol-formaldehyde resin.

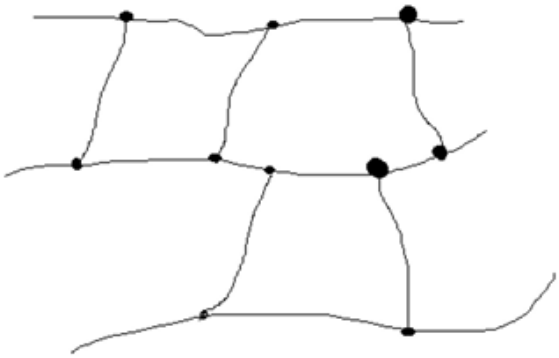

Figure 1: Thermoset Polymer Configuration [1]

Thermoplastics

Thermoplastics are polymer materials that can be reshaped after moulding. Upon reheating, the polymer chains are rearranged. In thermoplastics, the molecules are not connected chemically, but by weak hydrogen bonds and van der Waals forces (Figure 2). With the increase in temperature, the weak bonds are temporarily broken; thus, a new material configuration can be achieved. When the material is cooled and solidified, the secondary forces are restored, and the configuration is set once again. Thus, the remoulding of thermoplastic materials is not problematic [1].

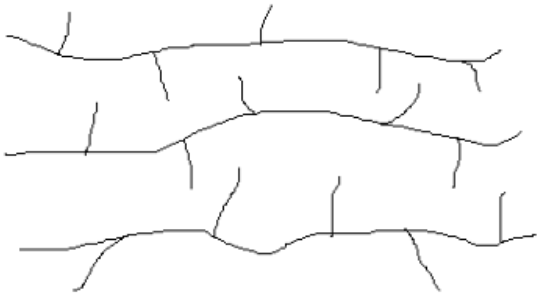

Figure 2: Thermoplastic Polymer Configuration [1]

Polymers are unique materials that are well known for two of their characteristics when compared to metal. The mechanical properties of polymers are highly dependent on temperature and loading rate. The tensile modulus of most polymers will decrease with the increase in temperature.

Polymer materials are also well known for their temperature transition behaviour. The glass transition temperature (T_g) is the transition at which the polymer changes from hard glassy material to a softer material. This transition is typical for amorphous polymers and the amorphous part of semi-crystalline polymers [4]. The polymer becomes more viscoelastic, showing an instantaneous elastic behaviour with viscous deformation. With the additional increase in temperature, the polymer is acting more like a rubber capable of withstanding large elastic deformation. Both amorphous and semi-crystalline polymers achieve a highly viscous state after further temperature increase [1].

At temperatures above T_g, polymers have high ductility and low modulus. If the polymer allows a large segment motion at temperatures below T_g, it behaves as a ductile material like polycarbonate (PC) or polyamide (PA). T_g is only present in the amorphous phase of the polymer, which makes up to between 20% and 80% of the semi-crystalline polymer [4]. On the other hand, amorphous polymer materials like poly (methyl methacrylate) (PMMA) and polystyrene (PS) observe a brittle failure as the segment motion is restricted [1].

The different behaviour of thermoplastic polymers is shown in Figure 3. When semi-crystalline polymers are heated, the crystals in the material structure begin to melt at a high temperature. At this point, the heat does not increase until the last crystal melts. Amorphous polymers do not exhibit this phenomenon, and absorbed heat only increases the temperature [4].

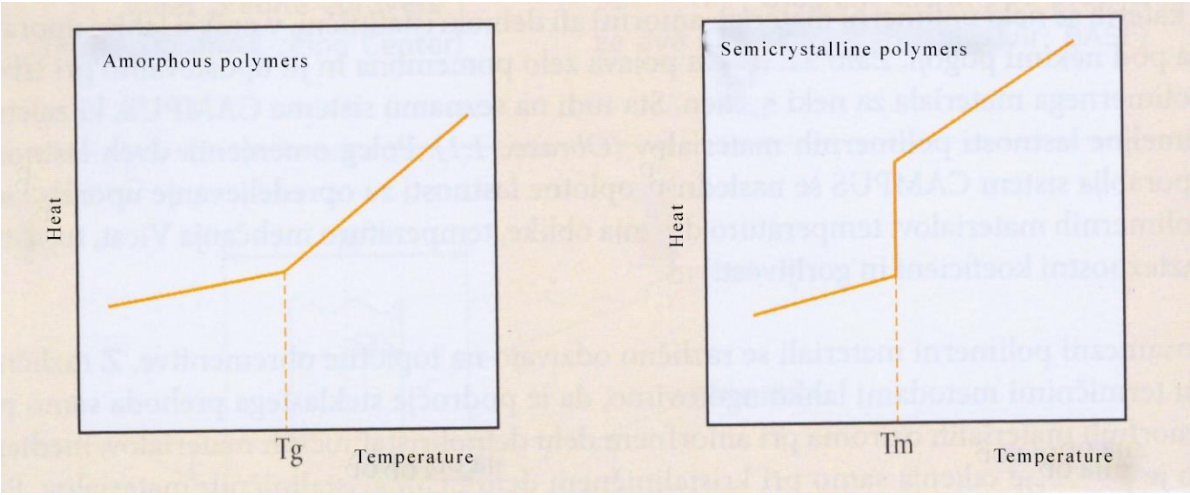

Figure 3: DSC Curves During the Glass Transition of an Amorphous Polymer and Melting of a Semi-crystalline Polymer [4]

Figure 4 shows the stress and strain behaviour of polymer solids under the effect of loading rate and temperature. We can conclude that polymers behave like a brittle material at low temperatures, there is no yielding, and the strain is low. If the temperature increases, yielding may occur, but the yield strength decreases. The polymer then acts as a more ductile material with high strain [1].

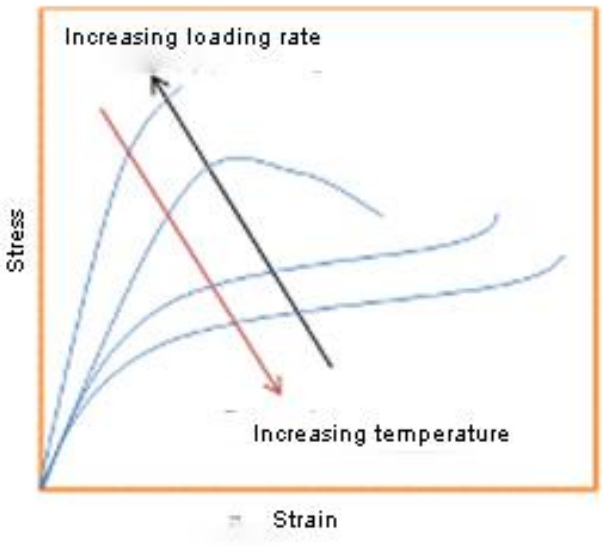

Figure 4: Stress-Strain Behaviour of Polymer Solids Under Different Temperature and Loading Rate [1]

Creep and stress relaxation are also crucial when working with polymers. During the creep tests, deformation is measured as a function of time at constant stress, while during the stress-relaxation test, strain is a constant while the stress is measured as a function of time [1].

2.1.1 Polyamide 66

Polyamides or nylons are engineering semi-crystalline polymers widely used in the automotive industry and other highly demanding engineering applications. Nylon is a generic term mainly applied to the family of polyamides [2]. There are several types of polyamides in the polymer industry, such as PA 6, PA 66, PA 12, PA 610, etc. The carbon atoms in the monomer can distinguish different types of polyamides. For example, PA 12 polymer is synthesised from monomers with 12 carbon atoms. PA 610 is synthesised from hexamethylene diamine and sebacic acid. The naming of PA polymers indicates the number of carbon atoms in the monomers used to create the polymer, as shown in Figure 5 [3,5]. PA 66 is synthesised from adipic acid and hexamethylene diamine; the chemical structure is shown in Figure 6 [6].

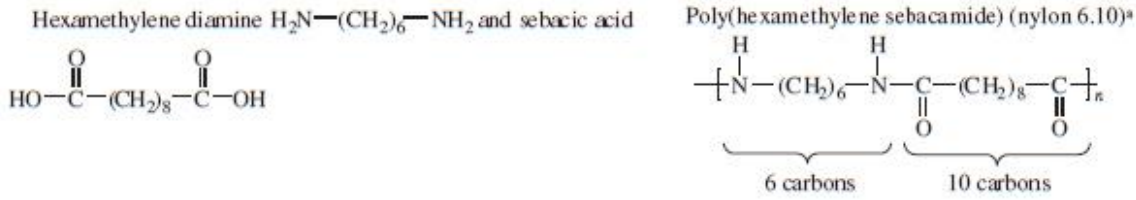

Figure 5: Chemical Structure of PA610 [3]

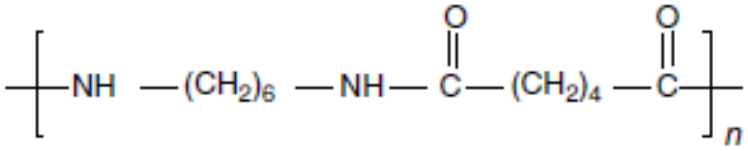

Figure 6: Chemical Structure of PA 66 [6]

PA is mostly known for high mechanical strength and temperature resistance; also, they exhibit high unnotched impact toughness and high resistance to crack initiation. Typical properties of PA can be observed in Table 1; note that these properties are just for reference [2]. With each type of polyamide and different producers, these values can differ.

Table 1: Typical Properties of PA 66 [2]

Properties	Unit	Value
Density	kg cm^{-3}	1140
Glass Transition Temperature (T_g)	°C	50
Melting Temperature (T_m)	°C	265
Heat of Combustion	kJ g^{-1}	31.9
Thermal Linear Expansivity	10^{-5} K^{-1}	9
Specific Heat Capacity	kJ kg^{-1} K^{-1}	1.70
Thermal Conductivity	W $m^{-1}K^{-1}$	0.25
Heat Deflection Temperature at 445 kPa	°C	245

When working with PA, water content and degree of crystallinity significantly affect the material's properties. With increased carbon atoms, the water absorption capability falls, improving the dimensional stability. Table 2 shows water absorption percentages of different PA types. Thus, proper material preparation and processing are required to achieve desired dimensions and properties. Processing data for PA is shown in Table 3 [5].

Table 2: Comparison of PA Types [5]

Type	Density [g/cm³]	Water Absorption [%]
PA6	1.12–1.15	2.8–3.2
PA66	1.12–1.15	2.5–2.7
PA610	1.06–1.08	1.2–1.4
PA11	1.04	0.8–0.9
PA12	1.01–1.02	0.7–0.8
PA Amorphous Types	1.06–1.08	0.3–1.1

Table 3: Typical Processing Conditions of PA [5]

Predrying	Necessary due to the impact of moisture on mechanical properties and surface waviness.
Compound Temperatures	Recommended 10°C–50°C above melt temperature. PA6: 215°C PA66: 250°C PA610: 200°C PA11: 187°C PA12: 177°C
Mould Temperature	Between 50°C and 90°C. For higher crystallinity, 100°C–120°C is required.
Flow Behaviour	Quite good.
Shrinkage	0.2%–2.5% depending on the PA type and additives.

2.1.2 Glass Fibres

Composite materials consist of polymer matrix and reinforcement, which are used to achieve the desired product requirement. Nowadays, glass fibres are widely used in polymer composites by the aircraft and automotive industry for marine applications, sports, and construction. Glass fibres are commonly used due to their strength, thermal stability, low and cost-effectiveness compared to other types of fibres [7]. The matrix protects the fibres from the environment and keeps them in place [1]. The mechanical behaviour of, for example, IM polymer composite with glass fibres depends highly on the modulus, matrix strength, fibre strength, chemical and thermal stability, fibre orientation and the interface bonding between fibres and polymer matrix to enable the transfer of stress [7]. The fibre orientation plays a crucial role in determining the correct shrinkage value and warpage determination of an IM part. Fibres orient in the direction of the flow, which results in a much lower shrinkage than perpendicular to the fibres.

In general, fibres can be classified based on origin or length. By length, they are divided into two groups continuous and short or discontinuous fibres. Continuous fibres are commonly used with thermoset polymers due to their low viscosity. Short fibres are mostly up to a few centimetres long and are widely used with thermoplastic polymers [1]. Today different types of glass fibres are available on the market, from A glass fibres to S glass fibres; the classification and physical properties can be seen in Figure 7. Different types of glass fibres have been developed to meet the specific requirements

of various applications. The chemical composition of each glass fibre type in wt % is shown in

Table 4. The mechanical and physical properties of each type can be observed in Table 5 [7].

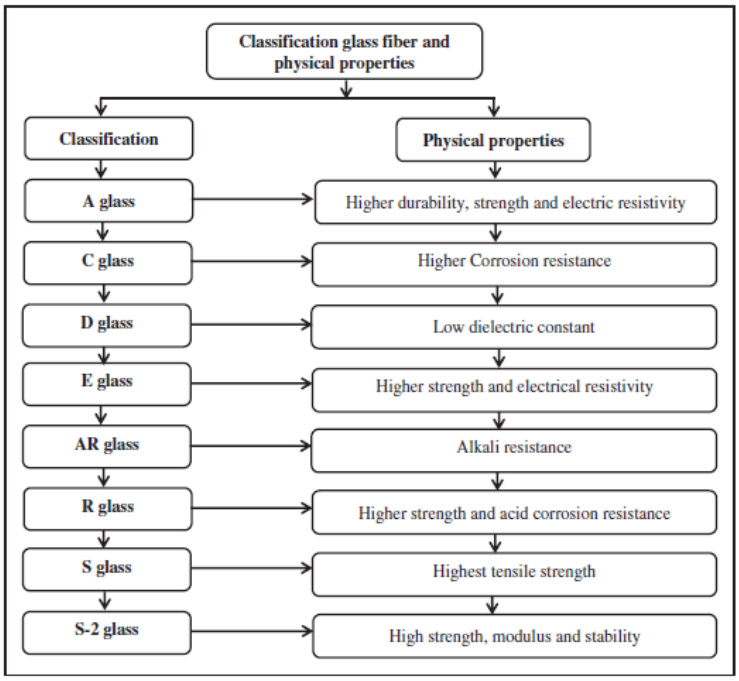

Figure 7: Classification of Glass Fibres and Their Physical Properties [7]

Table 4: Chemical Composition of Different Glass Fibre Types in wt % [7]

Type	SiO_2	Al_2O_3	TiO_2	B_2O_3	CaO	MgO	Na_2O	K_2O	Fe_2O_3
A Glass	67.5	3.5	-	1.5	6.5	4.5	13.5	3.0	-
C Glass	64.6	4.1	-	5.0	13.4	3.3	9.6	0.5	-
D Glass	74.0	-	-	22.5	-	-	1.5	2.0	-
E Glass	55.0	14.0	0.2	7.0	22.0	1.0	0.5	0.3	-
R Glass	60.0	24.0	-	-	9.0	6.0	0.5	0.1	-
S Glass	65.0	25.0	-	-	-	10.0	-	-	-

Table 5: Physical and Mechanical Properties of Different Glass Fibres [7]

Type	Density [g/cm^3]	Tensile Strength [GPa]	Young's Modulus [GPa]	Elongation [%]	Coefficient of Thermal Expansion [10^{-7}/°C]
A Glass	2.44	3.310	68.9	4.8	730
C Glass	2.52	3.310	68.9	4.8	63
D Glass	2.11–2.14	2.415	51.7	4.6	25
E Glass	2.58	3.445	72.3	4.8	54
AR Glass	2.70	3.241	73.1	4.4	65
R Glass	2.54	4.135	85.5	4.8	33
S-2 Glass	2.46	4.890	86.9	5.7	16

2.2 Injection Moulding

Injection moulding (IM) is one of the oldest and most widely used processes for polymer processing [8,9]. The automotive industry and consumer electronics are two of the primary industries that heavily rely on IM and are pushing the research and optimisation of the process further due to regular product development and high demand for new improvements and optimisations. Because of the high demand from the industry, more companies are using IM simulation software to avoid problems in the design phase and reduce the cost of production [10].

The IM process can be divided into 6 phases [10]:

- 1. Phase: mould closing,
- 2. Phase: injection,
- 3. Phase: packing,
- 4. Phase: cooling,
- 5. Phase: plastification and screw back,
- 6. Phase: ejection.

An example of an IM machine and its components are shown in Figure 8 and Figure 9. The operator interface of the control unit allows the operator to monitor and control the process. The IM process begins with closing the mould and inserting the material in the form of granules into the hopper [5,8]. The material is melted with the help of the heaters in the injection unit, together with the shear rate that occurs when granules move towards the front end of the screw. When the material is prepared, the screw moves forward, pushing the molten material out of the injection unit and inside the mould with high pressure. The material starts to solidify when in contact with mould, which is colder than the molten material. This process is accelerated by cooling water flowing in the cooling channels of the mould. During filling, packing, and cooling, the clamping unit keeps the two mould sides together, thus preventing the tool from opening and causing a flash effect on the part. When the material is in a solid state with sufficient rigidity, the mould is opened, and the part is ejected from the mould with ejectors pins [8,11].

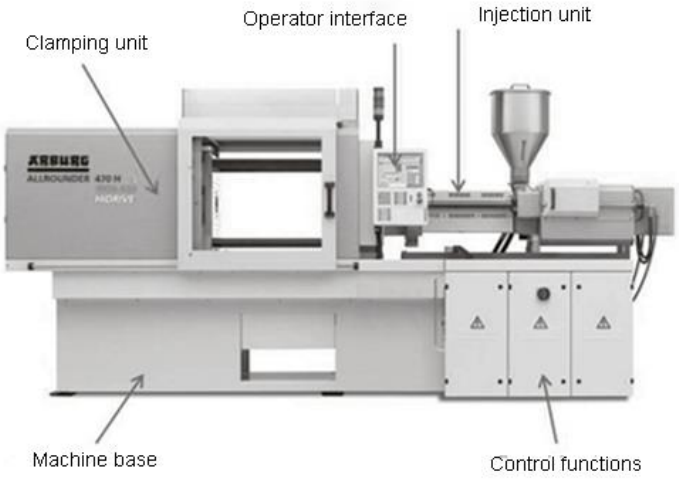

Figure 8: IM Machine and Its Essential Components [5]

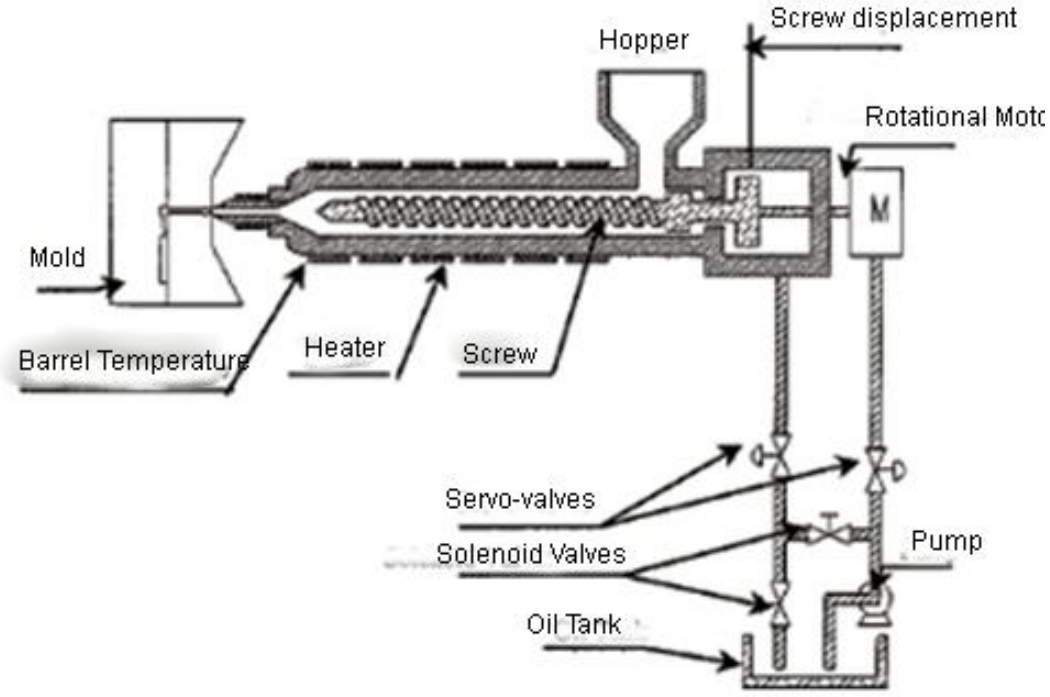

Figure 9: Schematic Diagram of an IM Machine [2]

A typical IM process pressure-time graph is shown in Figure 10, where [8]:

- (1) represents dead time,
- (2) mould filling,
- (3) packing,
- (4) sealing,
- (5) sealed cooling,
- (6) discharge.

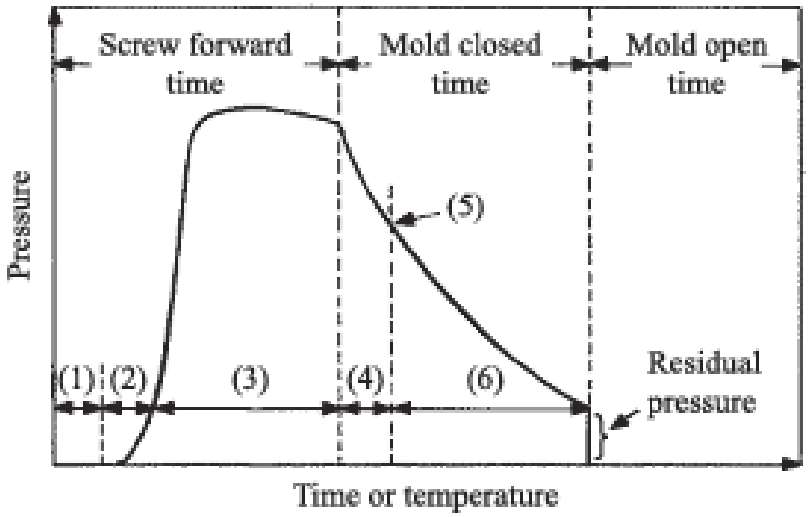

Figure 10: IM Pressure-Time Profile Curve [8]

IM process might be simple to learn but to master the IM process, a good understanding of the process parameters, material behaviour, and much practice is required. The most critical parameters are filling and packing pressure, mould and melt temperature, and cooling time [8]. The IM parameters are detected by different types of sensors which vary in sensing methods and purpose. In general, temperature and pressure sensors are most commonly used; Figure 11 shows the general classification of the sensors used in IM machines. Measuring the melt pressure during the IM process is hard since melt pressure can exceed values over 150 MPa, and the temperatures are often high and fast-changing. Also, the position of the sensor strongly influences the accuracy of the melt pressure and temperature measurement. If the pressure is measured directly in the mould or on the melt, some output variation will be present. Three examples of measuring principles are shown in Figure 12; direct measurement (a), indirect measurement (b), and contact-free measurement (c). In direct measurement (a), the melt pressure is applied directly on the sensor head, allowing exact measurements. In indirect measurement (b), the pressure is determined by measuring the force applied by, for example, the ejector pin on the pressure sensor. The contact-free (c) measurement is a common alternative used in IM machines and it involves capturing the mould compression induced by the melt pressure during the IM process [9]. Warpage analysis, material density, pressure, and temperature inside the mould are essential to determine the deformation of a part [8]. Even with IM simulation software, accurate warpage prediction is not easy because of the complex geometry shapes and viscoelastic nature, which depends on pressure, injection rate, and temperature. Also, the mathematical notation of the material behaviour is usually simplified in mathematical models.

Most numerical simulation software focuses mainly on phases from the injection of the material (phase 2) to the cooling of the part (phase 4) [10]. From the economic point

of view, it is essential to minimise the cooling time, which is the longest phase of the IM cycle; the time distribution of the IM process is shown in Figure 13 [11]. In the IM simulation, the melt is often assumed to enter the cavity with uniform temperature and prescribed flow rate or pressure [10]. To ensure the simulation is as accurate as possible to the actual material behaviour in the cavity, a good understanding of polymers, their properties, and the boundary conditions in the actual IM process is required. Also, the sensor type and the measurement locations are essential to analyse the pressure and temperature of the polymer during the IM process [9].

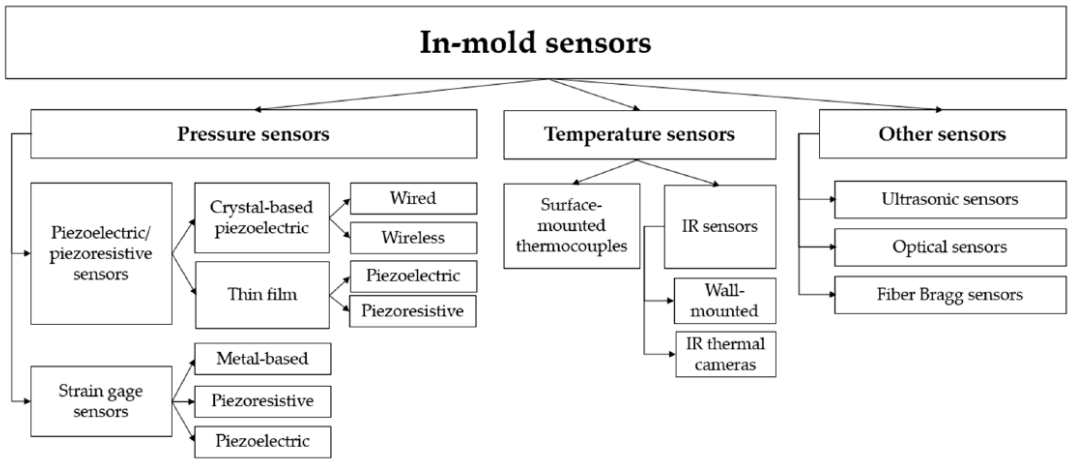

Figure 11: Classification of in-Mould Sensors [9]

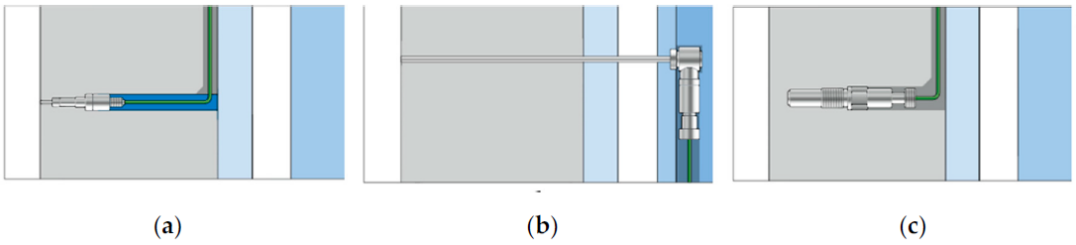

Figure 12: Examples of Measuring Principles: Direct Measurement (a), Indirect Measurement (b) and Contact-Free Measurement (c) [9]

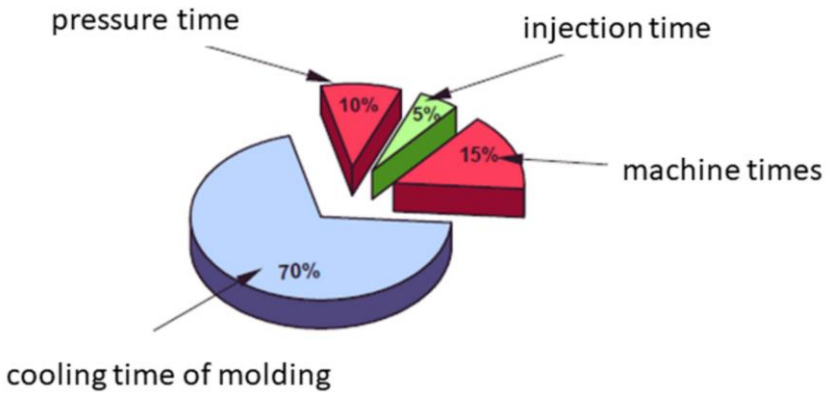

Figure 13: Time Distribution in IM Cycle [11]

2.2.1 Basic IM Terminologies

The Mould is a complex assembly of electrical and mechanical elements that plays a vital role in the final shape and dimensioning of the product [10]. In general, the mould is comprised of two halves of steel plates, one called the cavity side, which is fixed, and the other called the moving side or injection side. The injection side moves to the fixed side before the injection of the polymer melt material (phase 1) to form a cavity or in the opposite direction to allow the ejection of the part. These two sides are clamped with the machine's hydraulics to prevent opening when the material is pushed into the cavity with pressure.

The term cavity refers to the surface of the mould core and its counterpart that collectively shape the final product. The mould core is the two plates that form a closed mould cavity when the mould is closed (Figure 14). Sprue is the channel by which melt flows from the IM machine to the mould. The melt transfer from the sprue to the cavity is done with channels called runners. The entry area at which the melt reaches the mould cavity is called the gate (Figure 15) [10].

The gate diameter is much smaller than the runner diameter, which allows polymer material in the runner system (tunnel system for melt transfer) to be easily removed from the part [10]. After the ejection of the part, the runner system can be ground and reused to reduce plastic waste. Recycling of the runner system depends on the material type and customer requirement. For IM, cold and hot runner systems are commonly used.

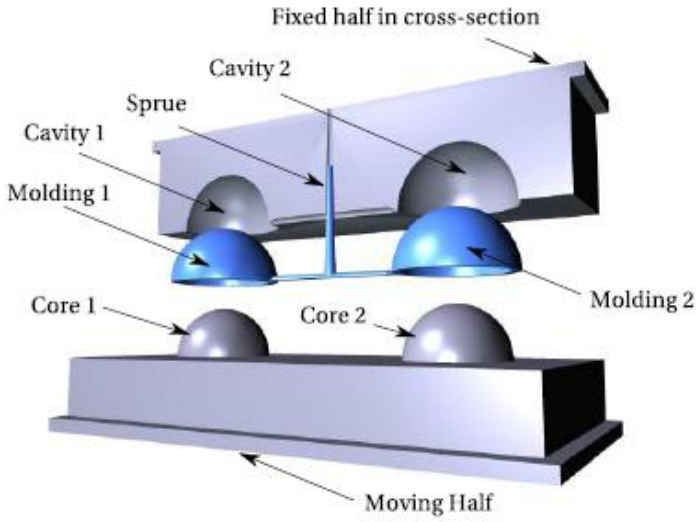

Figure 14: Two Cavity Moulds [10]

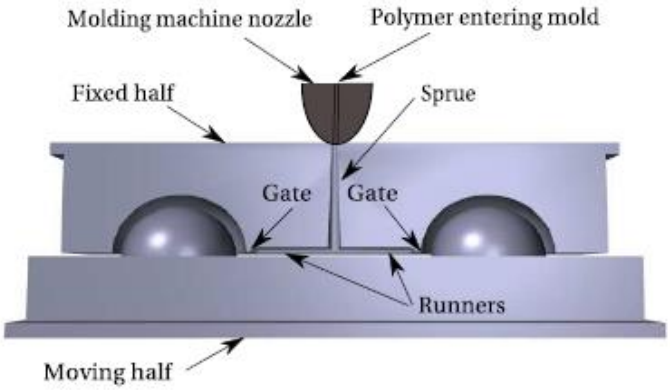

Figure 15: Two-Cavity Mould Showing Runner Concept [10]

2.3 Numerical Simulation of Injection Moulding in Moldex3D Software

The use of simulation software for polymer processing is increasingly more common. With simulation, mould and product design and the process itself can be optimised before production to avoid manufacturing problems. Using simulation saves time, material required to optimise the product in production, and other expenses. With simulation, we can see the flow of the material in every step of filling, which helps us to understand and study the product [2]. We can also obtain information regarding the pressure and temperature field in the cavity, the cooling time, and the predicted shrinkage and warpage.

Moldex3D is a numerical simulation software for polymer processing produced by DMPMOLD (china) [12]. These days numerical simulation software is commonly used in all technologically advanced industries. More customers demand simulation of IM for their product because unexpected failures can be prevented, filling anomalies and trouble points can be observed before prototype testing, pressure requirement and gate design can be optimised beforehand, and warpage trends with predicted deformation values can be beneficial when developing or optimising new products for IM.

2.3.1 Physics of Injection Moulding Process

The filling phase of IM is characterised by high material flow and, thus, high shear rate and shear stress. During this phase, the material melt is transferred from the injection unit to the mould using the injection ram. When melt reaches the mould cavity surfaces, it begins to transfer heat to the mould, the mould causes solidification of the melt, and the shape of the part is made. The solidified material plays a vital role in the part warpage and the effect of the packing phase on the part shrinkage [10]. If the material solidifies too quickly, the packing phase has little to no effect, and part warpage and shrinkage might cause problems for the part to be inside desired tolerance.

Switching from the filling to the packing phase is usually when 95% to 98% of the part is filled. Since the cavity is almost full, the melt flow is much smaller than during the injection phase. The pressure limit is usually around 80% of the injection pressure. The melt flow is still possible due to minimal material shrinkage, convection, and viscous dissipation effects. During this phase, most heat is transferred with conduction, and the solidified or frozen layers thicken and increase. When the material in the mould is sufficiently solidified, it can be ejected from the mould [10].

2.3.2 Why Is Simulation of Injection Moulds Required, and How Accurate Is It?

IM simulation was developed to predict and improve part quality in the product's development phase. At first, the part quality was mostly improved with process parameters. However, such optimisations require a lot of experience and knowledge of material processing and the effects of process conditions [10]. With IM simulation, problems that would occur in the production phase could be avoided with geometry optimisation, change in gate location, runner design optimisation, and improving the air venting of the mould. While some problems might be fixed with process parameters, some variations of parameters might cause other problems.

Improving the part in the design phase with IM simulations is more economically favourable than improving the quality in the production phase with process parameters or mould optimisation. Also, using IM simulation, different part designs, materials, and mould designs can be evaluated [10].

Before investing in simulation software, companies need to understand that the simulation results are highly dependent on provided data to the software, the assumptions made by the software, and, consequently, the knowledge of the researcher operating with the software [10].

2.4 Rheology of Polymers

The rheology of polymers is one crucial topic when dealing with IM simulation. Rheology is the science that studies the flow of matter and the deformation of polymer materials. Due to the large variety of polymers, researchers classify rheology into the following categories: thermosets, polymeric foams, homogenous polymers, fibre-reinforced polymers, liquid-crystalline polymers, and block copolymers. [13].

2.4.1 Viscoelasticity

During flow, most polymers have a viscoelastic behaviour, meaning they exhibit elastic and viscous behaviour in the liquid state. This viscoelastic behaviour is an intermediate behaviour between that of an ideal liquid and an ideal solid. In general, polymers will behave more like solids at lower temperatures and like liquids at higher temperatures.

The rheological properties of polymers are highly dependent on their chemical structure and molecular mass distribution [13,14].

The following three test methods are conducted to characterise a polymer's viscoelastic behaviour in a solid state: stress relaxation, dynamic mechanic analysis and creep [14].

During creep testing, the sample is placed under constant stress, and the strain of the sample is measured as a function of time. Ideal solids show immediate elastic strain. The strain will remain constant under stress but will return to zero if the stress is reduced to zero (elastic behaviour). Unlike solids, liquids lack the initial elastic response to the applied strain and instead display a continuous growth in strain. The slope of the strain increase is inversely proportional to the liquid viscosity while the strain rate remains constant. After the stress release, the liquid ceases to flow abruptly; thus, the strain rate drops to zero. The typical viscoelastic response during the creep test can be seen in Figure 16; the response can be divided into several districts. First, the initial elastic response region, the strain follows Hook´s law using zero-time modulus. The transition region is characterised by a nonlinear increase in strain. The third region, or equilibrium region, shows a linear strain increase over time. In the recovery region, the initial elastic retraction is followed by a gradual decay in strain, but the strain never returns to zero [14,15].

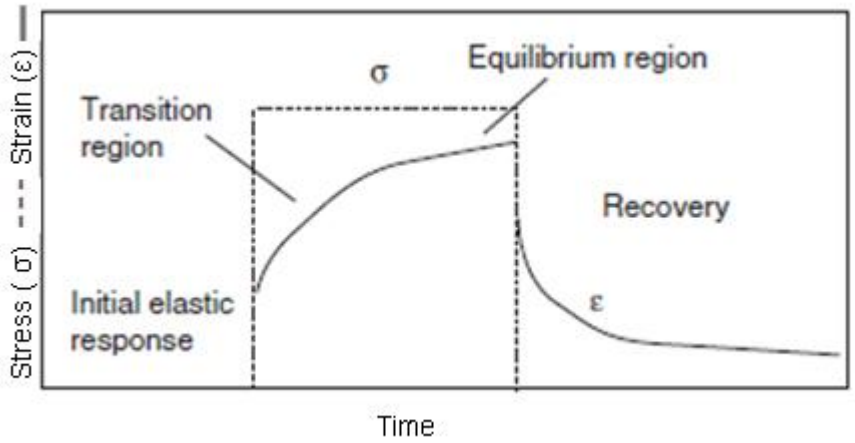

Figure 16: Viscoelastic Material Stress and Strain Curves as a Function of Time During Creep Testing [14]

In the stress relaxation test, the sample is placed under constant strain, and the resulting stress versus time is recorded. As mentioned before, polymers do not behave as ideal liquids or solids. If an ideal solid was tested on a stress relaxation test, we could see that the stress remains constant with time, whereas an ideal liquid measurement shows immediate return to zero stress at the start of imposed strain. Viscoelastic materials exhibit decay of stress with time when under constant strain [14].

2.4.2 Viscosity

Viscosity is one of the fundamental properties for determining the flow of polymers in a liquid state, and viscosity is a measure of the fluid´s resistance to flow [13]. Viscosity describes the flow of the material; for example, simple shear flow is shown in Figure 17. Assuming the top and bottom plates are equal and separated by a small distance in the Y direction. The top plate can move in the x direction by a constant velocity, whereas the bottom plate remains stationary. With experiments, equation 1 was made, which describes that F/A is proportional to V/Y in a steady state, with the constant η denoting the fluid viscosity. The left side of the equation (F/A) is called the shear stress, and the right side of the equation is called the shear rate (V/Y) [10,12].

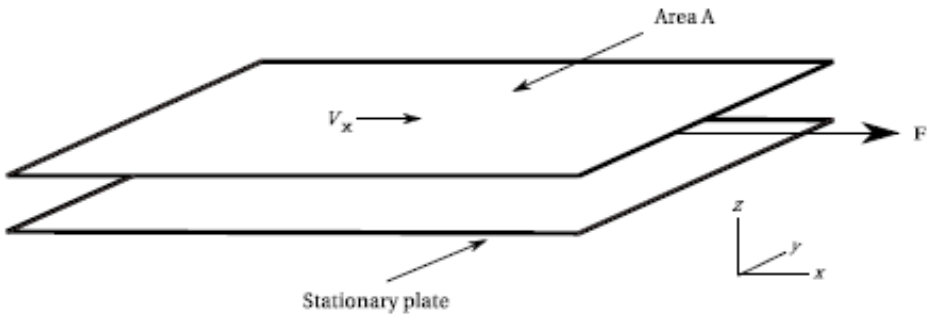

Figure 17: Material Flow Between Two Parallel Plates [10]

$$\frac{F}{A} = \eta \frac{V}{Y} \qquad (1),$$

$$\tau_{xy} = \eta\dot{\gamma}$$

Where:

- F - external force (N),
- A - area of the plate (m^2),
- η - viscosity (Pa*s),
- V - velocity (m/s),
- Y - the distance between plates (m),
- τ_{xy} - shear stress (N/m^2),
- $\dot{\gamma}$ - shear rate (1/s) [12].

The polymer's resistance to flow is mainly influenced by the conformation and orientation of molecular chains. With different flow fields, the conformation and orientation of molecular chains change; thus, the viscosity changes with the shear rate. The relationship between the viscosity of polymers versus the shear rate is shown in Figure 18.

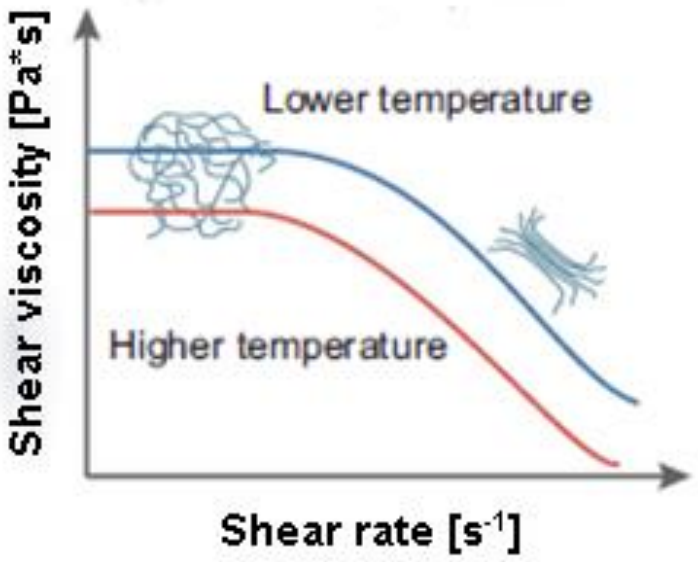

Figure 18: Viscosity Versus the Shear Rate of Polymers [12]

Polymers in a liquid state exhibit a unique rheological characteristic that is not seen in Newtonian fluids. During the flow of polymer liquids through a cylindrical tube, the polymer viscosity decreases with the increase in shear rate. This phenomenon is called shear thinning behaviour and can be seen in Figure 19 [13].

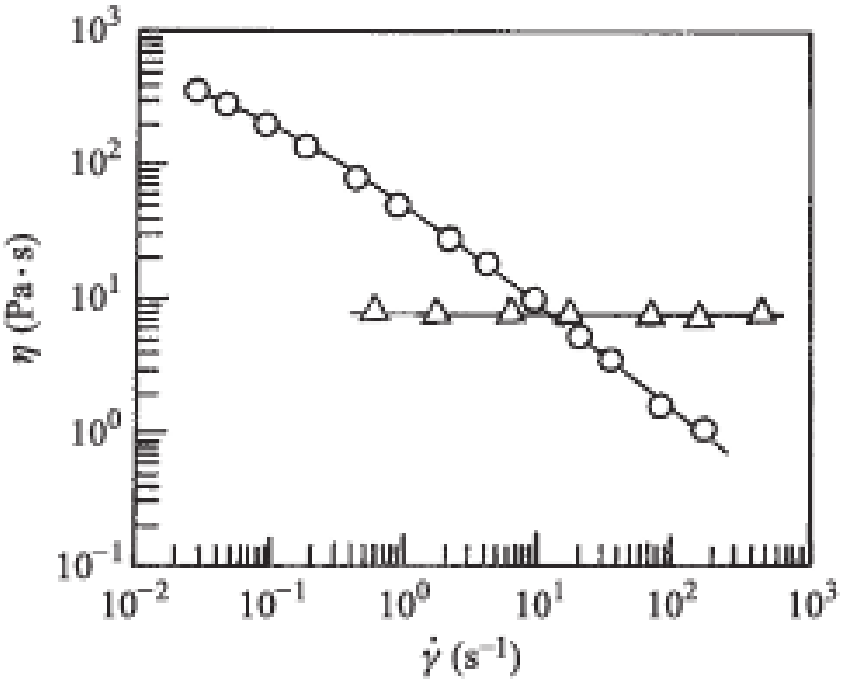

Figure 19: Measurement of Shear Viscosity (η) as a Function of Shear Rate (γ) for 4 wt % Liquid Solution of Glycerin (∆) and Polyacrylamide (○) at 25°C in Steady-State Shear Flow [13]

IM simulation software such as Moldex3D uses several theoretical models to describe polymers' viscosity versus shear rate behaviour. Some of the commonly used theoretical models are [10,12]:

- Power-Law Model,
- Carreau Model,
- Cross Model,
- Modified Cross Model,
- Herschel-Bulkley Model.

The Modified Cross Model is one of the most widely used theoretical models for viscosity approximation within the Moldex3D software. The Modified Cross Model is represented in equation 2. The second theoretical model that is described in the master's thesis is the Herschel-Bulkley Model which is widely used for materials with high filler content; the theoretical model is represented in equation 3 [10,12].

$$\eta = \frac{\eta_0}{1+(\frac{\eta_0}{\tau^*}\dot{\gamma})^{1-n}} \qquad (2),$$

Where:

- η - viscosity of polymer melt (Pa*s),
- η_0 - zero-shear rate viscosity (Pa*s),
- $\dot{\gamma}$ - shear rate (1/s),
- τ^* - critical shear stress (Pa),
- n - power law index (/) [10,12].

$$\eta = \frac{\tau_y}{\dot{\gamma}} + \frac{\eta_0}{1+(\frac{\eta_0}{\tau^*}\dot{\gamma})^{1-n}} \qquad (3),$$

Where:

- η - viscosity of polymer melt (Pa*s),
- η_0 - zero-shear rate viscosity (Pa*s),
- $\dot{\gamma}$ - shear rate (1/s),
- τ^* - critical shear stress (Pa),
- τ_y - yield stress (Pa),
- n - power law index (/) [12].

2.5 Polymer Analysis Methods

2.5.1 Melt Flow Rate (MFR)

Melt flow index (MFI) or melt flow rate (MFR) is a method often used in quality control departments to measure the deviation of the MFI value of different material batches to ensure process stability. The test is described in ISO standard 1133 [2]. In some cases, MVR or melt volume rate is used instead of MFR. With MVR, we measure the volume of the material extruded from a standardised die under standardised pressure and temperature at a defined time; MVR is expressed in cm^3/10 min. With MFR, we measure the mass of the material extruded from a standardised die under constant shear stress and temperature at a defined time; MFR is expressed in g/10 min [4]. In general, MFR is commonly used in the polymer industry because it is simple and inexpensive to use. The structure of an MFR measuring device can be seen in Figure 20.

The stability of the material for processing can be determined by using MFI (Table 6). It is essential to mention that the measured MFR values vary based on polymer type, filler content, and measuring parameters. In general, it might not be the most exact method, but it is simple and low-cost for companies to afford [2]. If used correctly, it can provide some valuable information regarding the material's behaviour but must not be considered equal to the actual viscosity of the material. In our case, it is recommended that we follow the ISO 1133-2 version of the test which is suitable for moisture-sensitive materials such as PA, PC, ABS and PET.

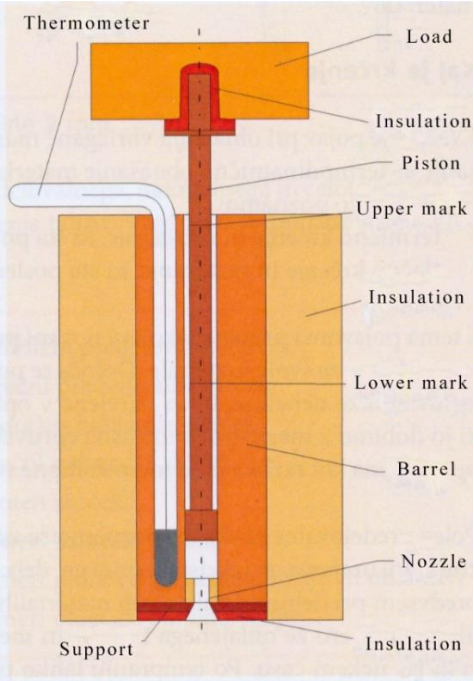

Figure 20: MFR Measuring Device [4]

Table 6: MFI Requirement for Different Processing Techniques [2]

Processing Technology	MFI [g/10 min]
Extrusion	0.01–10
Injection Moulding	1–100
Blow Moulding	0.01–1
Rotational Moulding	1.5–20

2.5.2 Thermogravimetric Analysis (TGA)

Thermogravimetric analysis (TGA) is a common thermal method in the polymer industry used to analyse changes in structural, physical, or chemical properties of a material caused by variations in temperature [16–18]. In general, temperature affects most chemical and physical properties of polymer composites and their structural transformation. The main thermal analysis techniques used by researchers these days are differential scanning calorimetry (DSC), differential thermal analysis (DTA), TGA, and derivative thermogravimetry (DTG). TGA analyses a material's mass changes as a function of temperature [17,18]. DTG plot is derived from the TGA plot and represents the derivative of the weight change curve versus temperature. A comparison of the TGA and DTG principle is shown in Figure 21. These techniques are commonly used in combination with each other. TGA/DTG is one of the most widely used techniques for characterising natural fibres [17,18]. DTA measures the temperature difference between the sample and the reference when heated or cooled. DTA results describe the material's phase transitions, decomposition, and other thermal events.

In the TGA method, a small sample of material is weighed constantly during heating to temperatures up to 1000°C in N_2 or O_2 atmosphere, allowing measurement of mass loss as a function of temperature and time [18,19]. Figure 22 shows the basic structure of the TGA measuring device. The basic TGA instruments involve a programmed furnace that enables linear temperature rise and a precision balance that constantly measures the mass of the material during the procedure. The computer or the control panel allows us to determine the heating rate and the operation mode required for our research. In general, TGA devices can heat the sample to 1200°C with a 0.5°C to 30°C linear heating rate [16].

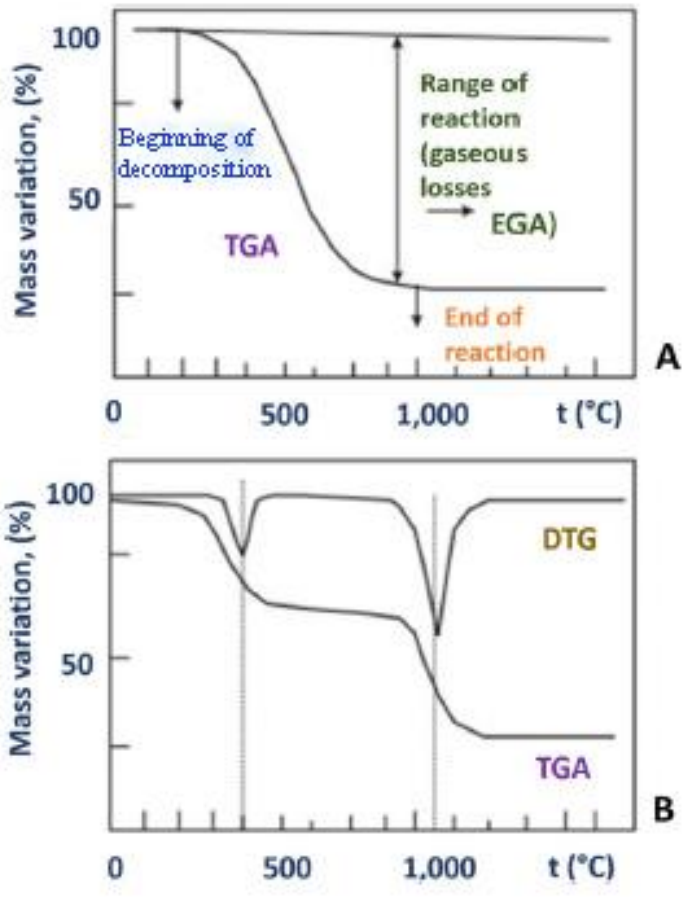

Figure 21: Comparison of TGA (A), m = f(t) and DTG (B), dm/dt = f(t) [18]

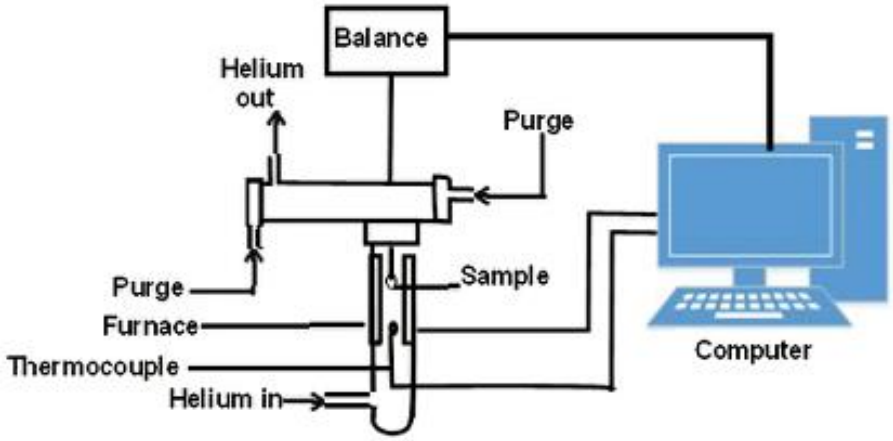

Figure 22: Thermogravimetric Analyser [16]

The kinetics of the material decomposition can be acquired using this technique, and thus we can evaluate the material's thermal stability. The TGA method is widely used for various polymer characteristics such as polymer lifetime determination, chemical composition, polymer degradation kinetics, and activation energy determination [19].

Three standard stages for TGA analysis are described and shown in Figure 23 [16]:

- The first stage (drying stage, marked a): this stage takes place between 25°C and 150°C depending on the polymer type. The loss of mass is a consequence of the vaporisation of moisture, which also indicates material hydrophobic or hydrophilic behaviour. Also, loss of other volatile ingredients like unreacted monomers can be detected.
- The second stage (main pyrolysis stage, marked b): this stage takes place between 150°C and 300°C, depending on the polymer type. During this stage, the degradation of the polymer starts and ends with complete degradation of that polymer. Overall, most polymers are pyrolysed up to about 600°C.
- The third stage (carbonisation, marked c): this is the final stage, which takes place between 500°C and over 1000°C. During this stage, the majority of the material is decomposed. Some inorganic additives like glass fibres remain after this stage (marked d).

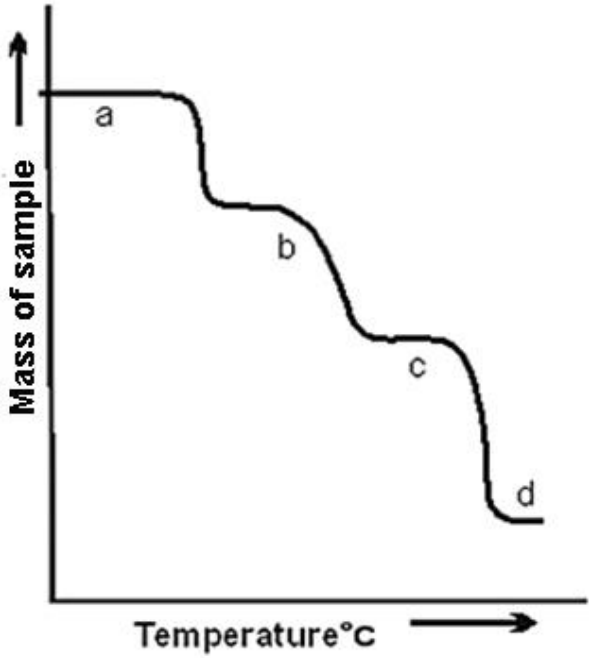

Figure 23: Thermogravimetric Curve and Standard Stages [16]

2.5.3 Dynamic Mechanical Analysis (DMA)

Dynamic mechanical analysis (DMA) is a standard analytical technique to analyse the mechanical properties of polymer composites as a function of temperature or frequency. DMA analysis is commonly used to determine composite materials' mechanical properties and viscoelastic behaviour under dynamic load [20]. DMA measures the sinusoidal strain as the sample response to oscillating sinusoidal stress at a given frequency or temperature, as shown in Figure 24. For viscoelastic materials such as polymers, the phase angle δ, the lag between the stress and strain sine waves, is typical [14,21].

Storage modulus or dynamic modulus (*E´*, elastic response) and loss modulus or dynamic loss (*E´´*, viscous response) are two mechanical properties that describe the relationship between the applied stress and produced strain during the DMA analysis, which can be seen in Figure 25. The storage modulus represents the material's ability to return or store energy and is commonly associated with the "stiffness" of a material. On the other hand, the loss modulus shows the material's ability to dissipate or lose energy. The relationship between the two moduli is represented as tan δ = *E˝*/*E´* and is called damping. A low tan δ value indicates high material elasticity, while a high tan δ indicates non-elastic material behaviour [20,22,23]. An important parameter commonly used in DMA is the complex or the shear modulus (*E**). The complex modulus describes the material behaviour under deformation. It combines the viscous and elastic behaviour of the material; the complex modulus is described in equation 4. The relationship between each parameter is shown in Figure 26 [20,23].

$$|E^*| = \sqrt{E'^2 + E''^2} \quad (4),$$

Where:

- *E´* - storage modulus (Pa),
- *E˝* - loss modulus (Pa),
- *E** - complex modulus (Pa) [10,24].

During the measurement, the DMA analyser measures *E˝*, *E´*, phase angle, the amplitude of the tan δ, and its spring constant, denoted as k. When the material exhibits more elastic behaviour, *E** approaches *E´*, decreasing the phase angle [23]. A composite material's glass transition (T_g) is determined from the peak of tan δ or drop of the loss modulus [21].

Time-temperature superposition (TTS) allows the measurement of the material's viscoelastic behaviour over a wide frequency range or a long time. With TTS-measured data, we can predict *E´* at frequencies or temperatures beyond the measuring limit. TTS technique uses time-temperature "equivalency". The material's viscoelastic behaviour varies similarly at high temperatures; it displays properties comparable to those at low frequencies. Whereas at lower temperatures, the viscoelastic behaviour of the material is similar to the response at higher frequencies [22].

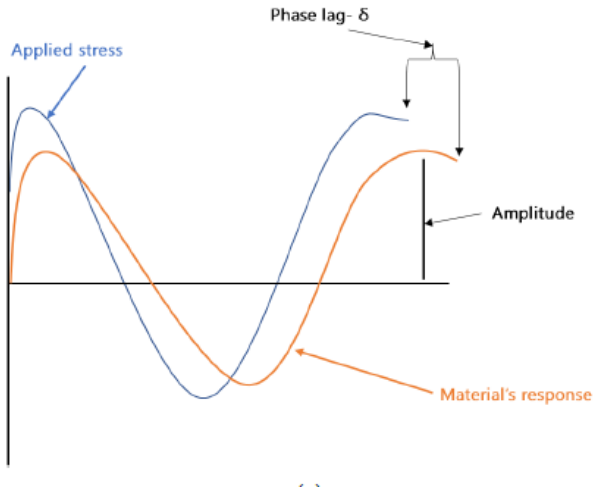

Figure 24: Applied Stress on the Sample and Its Response During DMA Measurement [21]

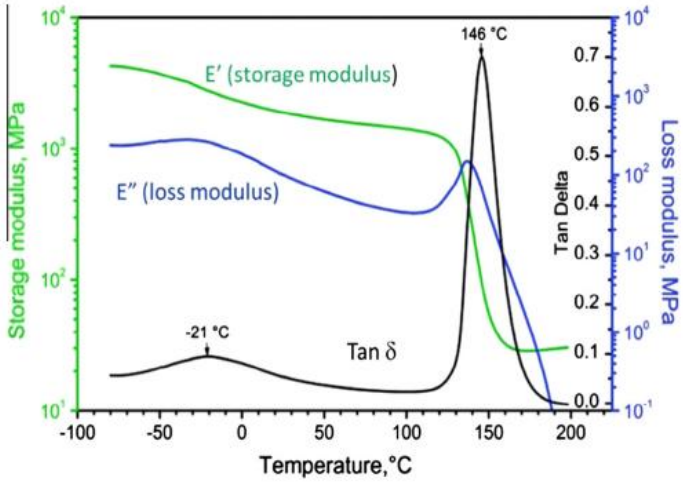

Figure 25: DMA Curves of Loss Modulus, Storage Modulus and Tan δ as a Function of Temperature [20]

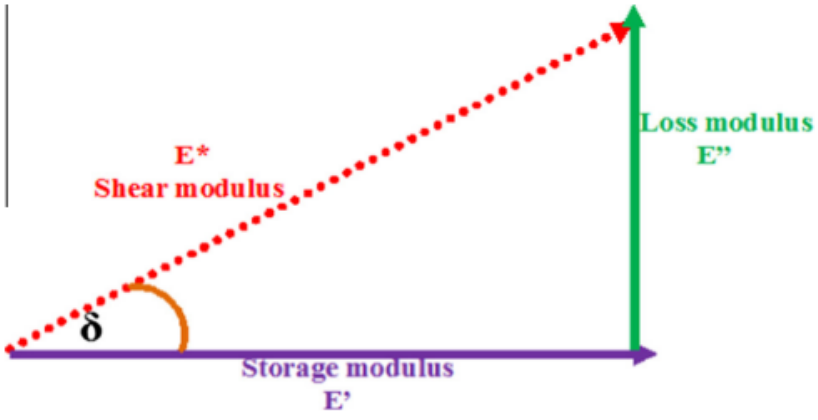

Figure 26: Relationship Between DMA Parameters [20]

2.5.4 Differential Scanning Calorimetry (DSC)

Differential scanning calorimetry, or DSC, is a thermal analysis technique that measures the amount of enthalpy released or absorbed by the sample when cooled, heated, or held at a constant temperature. DSC measurement provides information regarding the physical or chemical changes that include changes in heat capacity or involve endothermic or exothermic processes [19,25]. In the DSC measurement, the temperature of the material is maintained, decreased, and increased at a constant or predetermined rate, depending on the analysis program [16].

DSC method can be used for obtaining information regarding the following material properties [19,25]:

- thermal history,
- cold crystallization,
- crystallization,
- degree of crystallinity,
- transition temperatures and enthalpies,
- oxidation induction time,
- curing and polymerisation kinetics.

The DSC measuring procedure is described in the following paragraph:

The sample and the reference in pans are put on a heated thermoelectric disk inside the furnace, shown in Figure 27 [26]. The two thermocouples maintain the differential heat flow of the sample and reference. The energy that the sample emits or absorbs during an exothermic or endothermic event is compensated by adding an equivalent amount of energy to the sample by the DSC apparatus. With this step, the isothermal conditions of the reference holder and sample remain the same. The heat flow rate between an inert material and the sample is measured as a function of temperature and time [16].

In Figure 27, different DSC measuring systems are represented with a focus on the precision of sample heat absorption or release measurement. Figure 27a represents a two-dimensional measuring system commonly used in ultra-fast DSC or heat flow DSCs. The sample and reference are put in the same furnace at different positions [4,26].

This measuring system, shown in Figure 27a, is commonly used because of its short measuring time compared to three-dimensional systems, but the two-dimensional system has a drawback. The sample does not only exchange heat with the sensor but also with the surrounding oven. However, this cannot be measured using the heat flow sensor; thus, the results are not as accurate as with the three-dimensional system. Three-dimensional systems fix this drawback by allowing heat exchange only with the thermocouple and not with the surroundings [26].

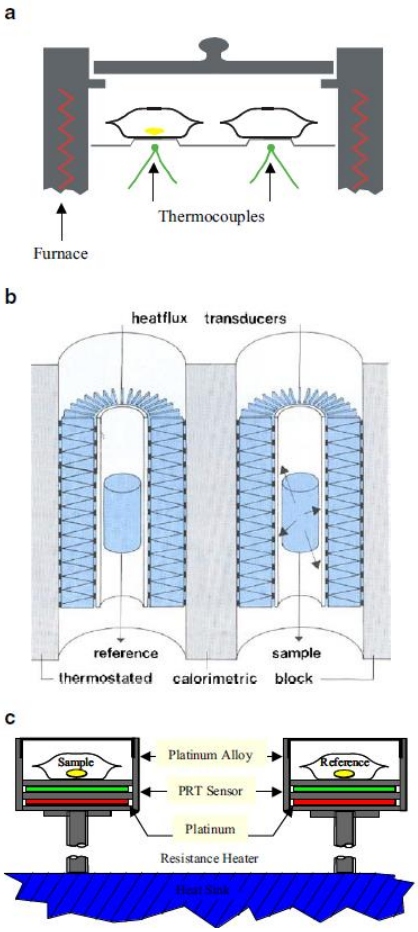

Figure 27: Three Different Types of DSC Measuring Systems. (a) – Two-Dimensional Plate, (b) Three-Dimensional Cylindrical and (c) Three-Dimensional System With Power Compensation [26]

Figure 27b shows a three-dimensional measuring system, also known as Tian-Calvet type heat flux DSC, which can measure up to 94% of heat exchange [26]. As mentioned before, this system has improved accuracy compared to the two-dimensional system but requires a long measuring time.

Figure 27c shows another three-dimensional system, also known as power compensation DSC. Here the sample and reference are placed in separately temperature-controlled ovens made of high-conductive metal [4]. The system uses active temperature control or power compensation to measure heat loss accurately [26].

Thermal events of DSC are shown in Figure 28. A positive peak usually (chosen by agreement) represents an exothermic transition, whereas an endothermic transition is represented by a negative peak [16]. Typical thermal events observed with DSC are the glass transition, crystallization, and melting. These thermal events define at which temperatures amorphous or semi-crystalline polymers can be used [4].

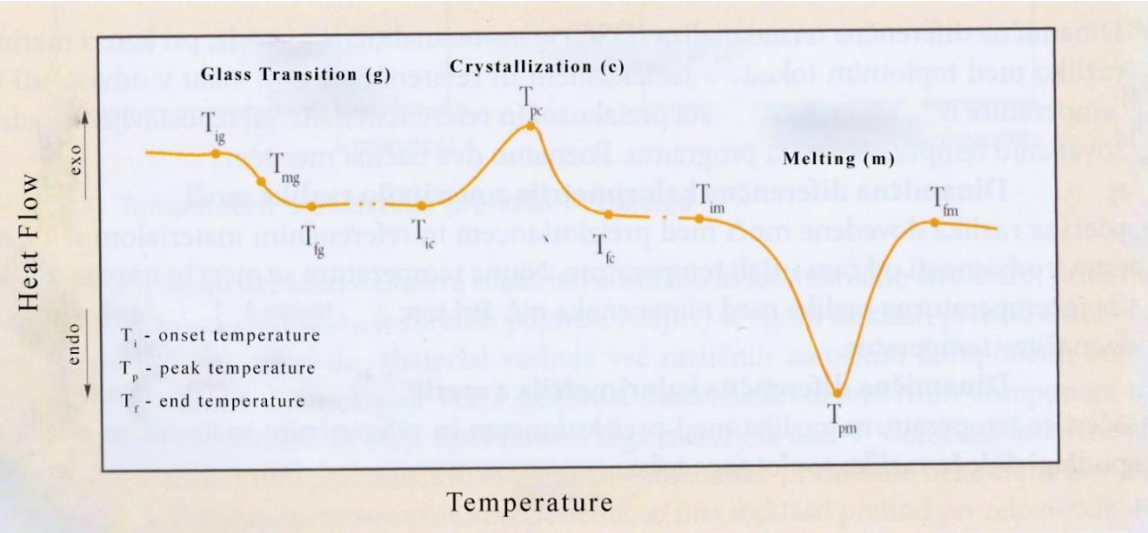

Figure 28: DSC Thermal Events [4]

Moreover, DSC allows us to measure the crystallisation of polymers, which is essential to evaluate the exact material behaviour during the IM process. When polymers are cooled, the crystallization is not instant but requires some time for the molecules to rearrange and form crystals. A schematic diagram in Figure 29 shows that the crystallization rate is relatively low at the beginning, and then the growth rate of crystals rapidly increases through time [12].

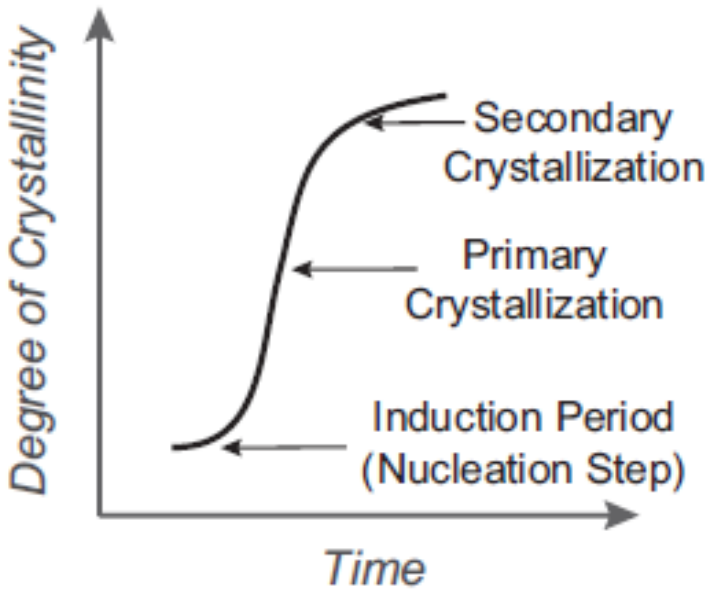

Figure 29: Theoretical Diagram of the Degree of Crystallinity Versus Time [12]

The Avrami equation is generally used to describe the crystallization kinetics of polymers. Moldex3D IM simulation software uses the Nakamura equation, developed

from the Avrami equation, to describe the crystallization kinetics of polymers. The Nakamura equation is described in equation 5:

$$\frac{dx_c}{dt} = \mathrm{nK(t)} \times (1 - \mathrm{x}_c) \times (-\ln(1 - \mathrm{x}_c))^{\frac{n-1}{n}} \qquad (5),$$

$$K(T) = ln(2)^{\frac{1}{n}} \times (\frac{1}{t_{1/2}})_0 \times \exp\,(-\frac{\frac{U^*}{R}}{T - T_\infty}) \times \exp\,(-\frac{K_g}{T \times \Delta T f})$$

Where:

- *K(t)* - non-isothermal crystallization rate constant (1/K),
- $t_{1/2}$ - crystallization half-time (s),
- T - crystallization temperature (K),
- *R* - universal gas constant (J/mol*K),
- ΔT - supercooling (K),
- *U** - activation energy of the crystallising units to transport across phase boundary (J/mol),
- T_∞ - the temperature at which the crystallization stops (K),
- *f* - correction factor accounting for the latent heat of fusion with temperature increase (/),
- x_c - degree of crystallization (/),
- *n* - Avrami index (/) [12].

TOPEM is a temperature-modulation technique introduced by Mettler Toledo. This technique uses stochastic modulation of the cooling or heating rate and random temperature pulses. By utilising this modulation, a large frequency spectrum is obtained, which allows us to determine complex specific heat capacity over a range of frequencies in a single scan. Separation of non-reversal and reversal effects is possible with this technique so that frequency-dependant thermal events (glass transition) can be separated from non-frequency-dependant ones (melting and crystallization) [25,27].

Figure 30 shows an example of measurement data using DSC TOPEM. A polyethylene terephthalate (PET) sample was preheated to 80°C and fast-cooled on an aluminium plate. The sample was then placed in a 40 µL aluminium crucible and heated at a 0.2 K/min heating rate. The upper black curve in Figure 30 represents the raw measurement data. The software then converts these data to calculate the total heat flow (black curve), non-reversing heat flow (blue curve), and reversing heat flow (red curve). This measurement can also determine specific heat capacity and phase curve-defined frequencies [25].

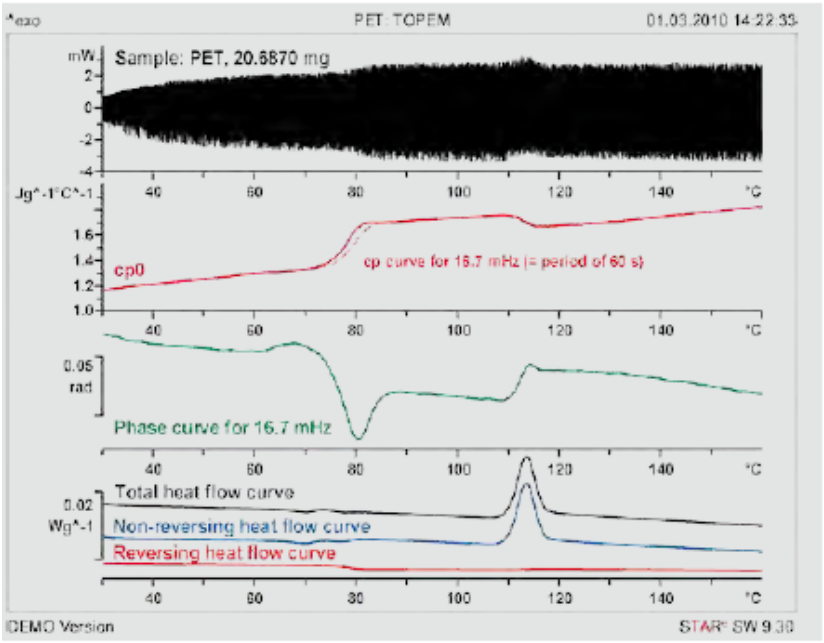

Figure 30: DSC Curves of a PET Sample Using TOPEM [25]

2.5.5 Thermal Conductivity

Thermal conductivity is an essential property that companies' research & development departments consider when choosing the appropriate material for a given application. Thermal conductivity refers to the ability of the material to conduct heat, which provides us with valuable information on the material's efficiency in transferring or absorbing heat [6,10]. The Fourier's law describes the factors that affect the conduction of materials, which is shown in Equation 6 and Figure 31. The units of thermal conductivity are Watts per meter Kelvin (W/m*K) or Joules per meter second Kelvin (J/m*s*K) [12,24,28]. Wood and most polymeric materials generally have low thermal conductivity; thus, they are good insulators. Good conductors of heat are metals like gold, copper, silver, and aluminium [6,28]. Thermal conductivity values of some thermoplastic polymers are shown in
Table 7 [10,29].

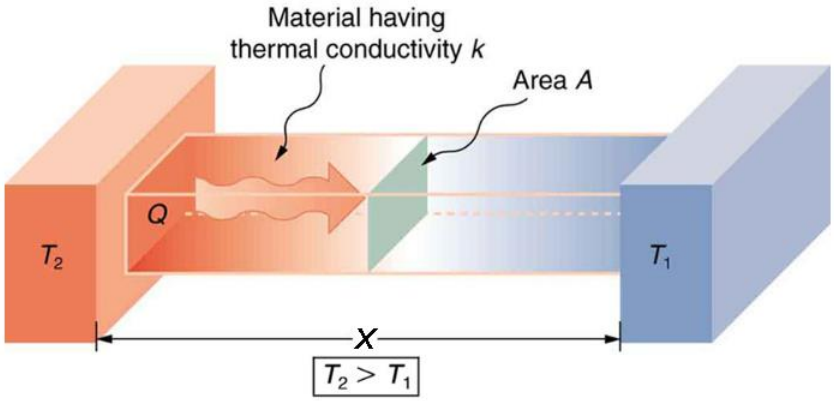

Figure 31: Heat Conduction Through a Material [28]

Table 7: Thermal Conductivity of Thermoplastic Polymers [10,29]

Material	Thermal Conductivity [W/m*K]
PC	0.19–0.21
PA 6	0.22–0.33
PA 66	0.24–0.33
PMMA	0.16–0.25
PS	0.10–0.15
ABS	0.15–0.20
PET	0.15
PP	0.11–0.17
Aluminium	250
Copper	401
Steel (AISI 1020)	51.9
Steel (AISI P20)	51.9

Fourier's law of heat conduction:

$$\frac{dQ}{dt} = -\mathrm{kA}\frac{dT}{dx} \qquad (6),$$

Where:

- Q - heat transfer (J),
- t - time (s),
- k - thermal conductivity (W/m*K),
- A - cross-sectional area (m^2),
- T - temperature (°C),
- x - thickness (m) [10,24].

Due to the low thermal conductivity of polymers, it is difficult to achieve accurate measurements. The thermal conductivity of polymers is highly dependent on molecular orientation, temperature, and degree of crystallinity [10]. The thermal conductivity of polymers can be improved by adding heat-conductive fillers, such as silicon nitride,

aluminium nitride, graphite, carbon nanotubes, and graphene. The filler type, size, and shape strongly influence the polymer composite's thermal conductivity [29].

IM simulation software uses theoretical models to approximate the material's behaviour during the IM process. The three theoretical models commonly used in IM simulations are [12]:

- Constant thermal conductivity: this is the simplest model, which assumes the thermal conductivity remains constant with temperature;
- Linear model: this model can be used for a simple approximation of the dependence of thermal conductivity on temperature;
- Tabulated data: this is quite commonly used in material cards for the IM simulation since this allows us to input the measured thermal conductivity values at different temperatures directly. The thermal conductivity between data points is approximated using standard linear interpolation; generally, 4–8 measured data points are used.

2.5.6 Specific Heat Capacity

The energy required to raise or lower the temperature of the material and the energy the material contains at a given temperature is defined by the specific heat capacity, *C* [10,12]. The unit of specific heat is Joule per kilogram degree Kelvin (J/kg*K); the specific heat capacity is described in equation 7 [10]. The specific heat can be provided in two forms based on the measuring technique: constant pressure (C_p) or constant volume (C_v). In general, the specific heat of polymers is much higher than metals, as shown in Table 8 [12].

The specific heat capacity is vital when calculating the heat loss from the melt to the cooling system during the filling, packing, and cooling phases. Also, it is used to calculate the heat generated by the viscous dissipation of the melt. Furthermore, it calculates the latent heat, which is the heat by the solidification of polymers, especially semi-crystalline polymers [10].

$$C_p = \frac{Q}{m \times \Delta T} \qquad (7),$$

Where:

- C_p - specific heat (J/kg*K),
- Q - required heat quantity (J),
- m - mass of the sample (kg),
- ΔT - temperature change (K) [6,10].

Table 8: Specific Heat Capacity Values of Materials [10,12]

Material	Specific Heat Capacity [J/kg*K]
ABS	1250–1700

POM-Acetal	1500
PA66	1700
PC	1300
PE	2300
PP	1900
PS	1300
PVC	800–1200
Steel (AISI 1020)	460

Moldex3D uses the following theoretical models to describe the specific heat of materials [12]:

- constant specific heat;
- linear model: specific heat at two different temperatures is given;
- three-stage linear interpolation model: specific heat is given at four different temperatures, two in solid state and two in liquid;
- tabulated data: variable number of specific heat values at temperatures can be used. Between two measured values, a standard linear interpolation is used.

2.5.7 Tensile Test

The tensile test is a commonly known method used to obtain information regarding the material´s elastic and plastic behaviour. The tensile test is described in ISO 527 or ASTM D638 [4]. Some properties acquired from a tensile test are the material's elastic or Young's modulus (*E*), ultimate strength, strength coefficient, stiffness, and initial yield strength. A standard tensile test diagram shows stress (σ) or applied force on the y-axis and strain (ε) on the x-axis [15,30]. The corresponding sample deformation during measurement is illustrated in Figure 32.

Block 1 represents the elastic response of the material to stress up to the yield point. In block 2, the material deformation remains uniform, and the material experiences plastic deformation. Uniform deformation takes place up to the curve maximum or the ultimate stress. After this point, non-uniform deformation starts and lasts until the fracture point [30]. Hook's law describes the relationship between stress, strain, and elastic modulus in the elastic region [15]. Hooke's law can be expressed as:

$$\sigma = E \cdot \varepsilon \qquad (8),$$

Where:

- σ - stress (N/m^2),
- E - Young's modulus (Pa),
- ε - strain (/) [15].

Tensile test procedure:

First, the tensile specimens are embedded in the testing machine. The exact dimension of each specimen can be measured and added to the testing software to

improve the accuracy of results. The specimens are stretched with constant speed and increasing force until they break. The measuring machine constantly measures the strain of the sample during the procedure [4].

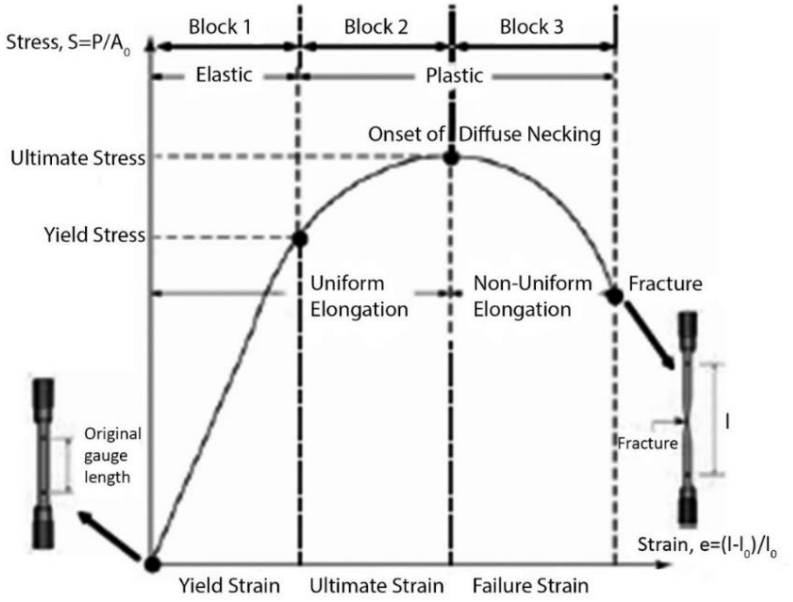

Figure 32: Typical Stress-Strain Curve for a Metal Material [30]

Four types of curves are most common for tensile testing of polymer materials. They are shown in Figure 33. Curve "A" represents the properties of brittle and rigid amorphous polymers like PMMA and PS. These materials stretch only slightly during stress; when the material reaches the critical strain, it breaks. Curve "B" represents the properties of rigid materials which, after reaching ultimate stress, still stretch and can absorb additional stress. This effect is due to the macromolecule's orientation due to the heavy stretching of the material. This behaviour is typical for PA, PE, and PP. Curve "C" represents a similar material with the difference that such materials do not increase in strength after yield stress. This behaviour is typical for PC, acrylonitrile butadiene styrene (ABS), and acrylonitrile styrene acrylate (ASA). Curve "D" represents soft and rigid elastic polymers which exhibit high elongation even at low stress (rubbers) [4,15].

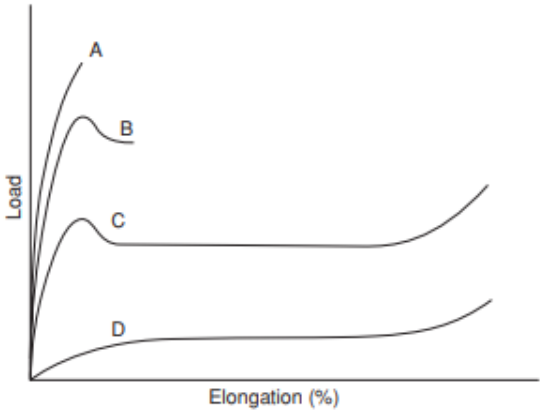

Figure 33: Typical Stress-Strain Curves for Polymers [15]

2.5.8 PVT Properties

For engineers and IM machine operators, the PVT diagram or pressure-volume-temperature behaviour of a polymer is essential. The polymers PVT diagram is used to investigate the nature of phase transitions and the polymer melts surface tension calculation, warpage calculation, and the prediction of service life and service performance of polymer materials based on the free volume concept [4,31]. PVT data is one of the most critical information IM simulation software uses to approximate the material behaviour during the IM process. For the IM industry, optimising the product design and minimising warpage is vital to deliver good products to the customer. Some of the fundamental process parameters influencing warpage are the mould and melt temperature, packing pressure, packing time, and cooling rate. By analysing PVT diagrams, optimal IM processing conditions and minimal warpage can be achieved [32].

PVT properties of a material are required to create a good quality material card. Two PVT diagram samples, one of amorphous PS and the other of semi-crystalline high-density polyethylene (HDPE), are shown in Figure 34. The diagrams show the typical characteristics of these two thermoplastic groups. Elongation and shrinkage of both groups highly differ. When processing or simulating the behaviour of polymer materials, these characteristics of different polymer types must be considered [4].

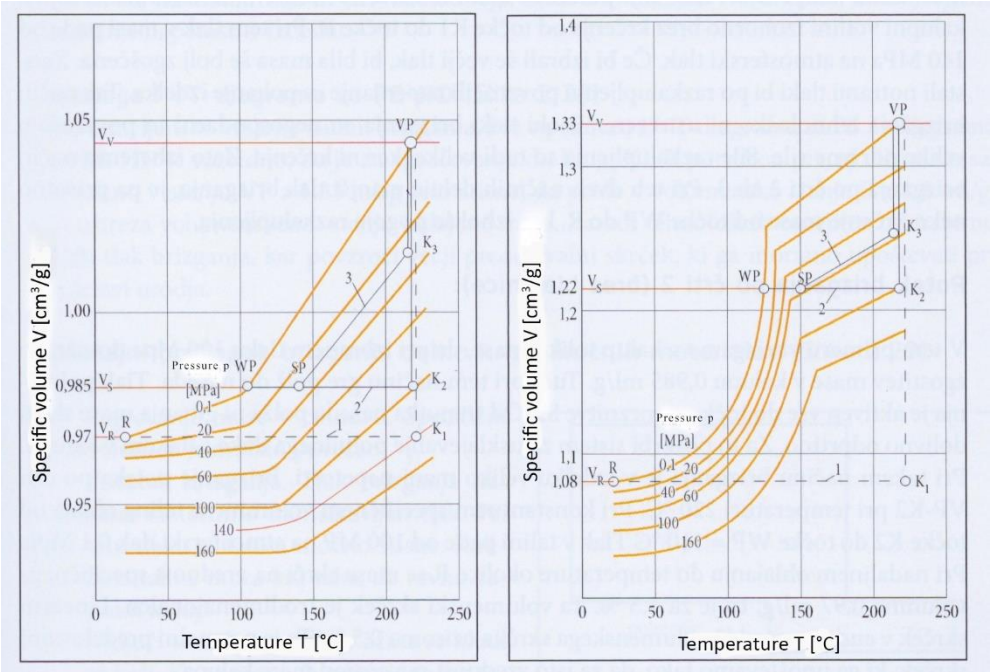

Figure 34: PVT Diagram of PS (left) and PE-HD (right) [4]

A dilatometer is commonly used to measure the bulk-specific volume as a function of the pressure and temperature of polymers. The two main techniques used to analyse the PVT behaviour are the piston-die technique and the confining-fluid technique; Figure 35 shows the sketch diagrams of the two techniques. With the piston-die technique, the polymer is pressurised and enclosed in a die using a piston [31]. The PVT device measures the piston's displacement to calculate the material's volume during the change in pressure and temperature. This technique is commonly used due to its simplicity [31,33]. The main disadvantage of this technique is that the pressure applied during the measurement is not hydrostatic due to the wall sticking of the material. Two possible errors during the PVT measurement using the piston-die technique are the formation of voids in the sample when the material is solidifying and possible leakage between the piston and the die [31].

The confining-fluid technique is more complex than the piston-die technique. The method involves immersing a sealed sample in liquid mercury or silicon oil. During the measurement, the fluid is pressurised and heated. The bellows of the enclosed chamber are then used to measure the volume during the measurement. The specific volume of the polymer is then calculated by the correction of the relative difference in the volume of the confining fluid [31,33]. Using this technique, leakage and friction of the sample during measurement are not problematic compared to the piston-die technique; the applied pressure is hydrostatic. The disadvantages of the technique are that possible reactions between the fluid and the polymer can occur, and the measured volumetric change is only that of the polymeric sample. According to testing done by Sato et al. in 1997, the difference between the two techniques in measurement principles of method does not lead to differences higher than 4% [31].

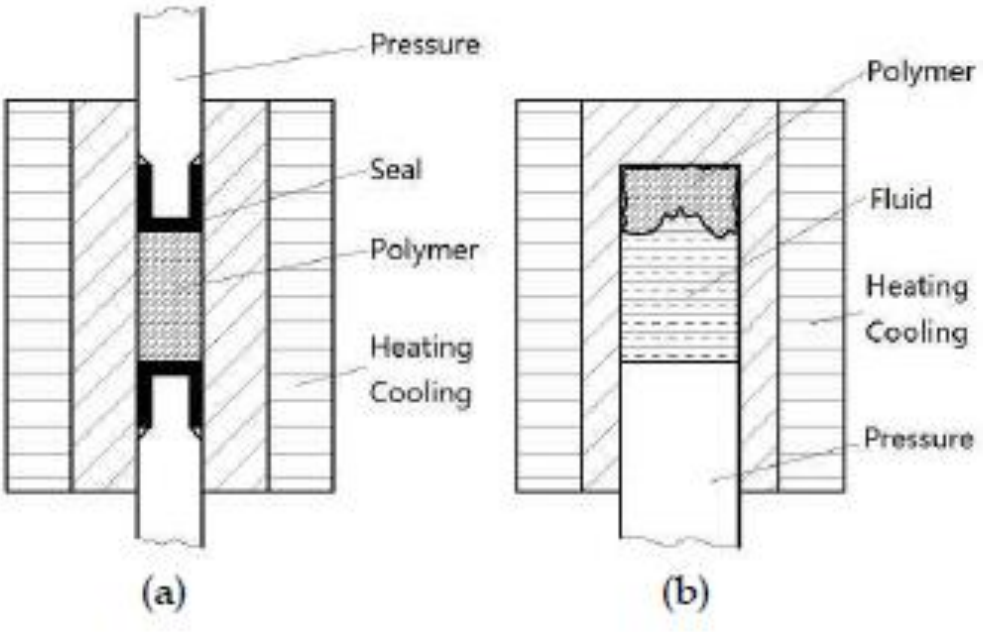

Figure 35: Diagrams of Piston-Die Technique (a) and Confining-Fluid Technique (b) [31]

Moldex3D IM simulation software uses several theoretical models to describe the PVT behaviour of polymer material. Some of the commonly used theoretical models are [12]:

- Constant specific volume,
- Spencer-Gilmore model,
- Tait model,
- modified Tait model (1),
- modified Tait model (2).

The Modified Tait model is most commonly used for IM simulation. The modified Tait (1) model introduced additional parameters to the original Tait model to improve the accuracy of the equation of state. The modified Tait (2) model was later introduced to deal with the abrupt volumetric change of semi-crystalline polymers. The theoretical model representing modified Tait (2) is shown in equation 9 [12,34].

$$\breve{V} = \breve{V}_0 \left[1 - \mathrm{C} \times \ln\left(1 + \frac{P}{B}\right)\right] + \breve{V}_t \qquad (9),$$

$$\breve{V}_0 = \begin{cases} b_{1s} + \quad b_{2s}\bar{T}, & if\ T \le T_t \\ b_{1l} + \quad b_{2l}\bar{T}, & if\ T > T_t \end{cases}$$

$$B = \begin{cases} b_{3s}\exp(-b_{4s}\bar{T}), & if\ T \le T_t \\ b_{3l}\exp(-b_{4l}\bar{T}), & if\ T > T_t \end{cases}$$

$$\breve{V}_t = \begin{cases} b_7\exp(-b_8\bar{T} - b_9 P), & if\ T \le T_t \\ 0, & if\ T > T_t \end{cases}$$

$$\bar{T} = T - b_5$$

$$T_t = b_5 + b_6 P$$

$$C = 0{,}0894$$

Where:

- *C* - universal constant (/),
- $\breve{V}_0$ - specific volume at zero pressure (m^3/kg),
- b_1 (b_{1m}, b_{1s}) and b_2 (b_{2m}, b_{2s}) - parameters describing the dependence of $\breve{V}_0$ on pressure and temperature,
- B - sensitivity to pressure as a function of temperature (m^3/kg),
- b_3 and b_4 - parameters describing the pressure as a function of temperature,
- $\breve{V}_t$ - specific volume increases due to crystallization (m^3/kg),
- T_t - transition temperature (K),
- b_5 and b_6 - parameters describing the change of T_t with temperature,
- b_7, b_8 and b_9 - parameters forming the state transition of semi-crystalline polymers [12,34].

Many theoretical models describing the PVT behaviour of polymer materials are available in IM simulation software. The accuracy of the theoretical model approximation is dependent on the measurement procedure and parameters and the fitting of the measured data to the theoretical model. In most cases, the modified Tait model will give a good approximation of amorphous and semi-crystalline polymers. When working with fibre-filled polymers, the approximation is not as accurate as for non-fibre filled materials since these theoretical models are not continuous at phase transitions. Thus, the continuous Renner model was developed by the company Simcom, which provides a more detailed description of the PVT behaviour of polymer composites. Renner model is shown in equation 10 [35,36].

The equation for the solid state:

$$V = \propto_s + \xi\left(\frac{T_b}{CS_5} + 1\right) \times (\beta_M - \propto_s) \qquad (10),$$

The equation for the molten state:

$$V = \propto_M$$

The constants are described as follows:

$$\beta_s = \frac{CS_1}{1 + CS_3 \times P}$$

$$\beta_M = \frac{CM_1}{1 + CM_3 \times P}$$

$$\propto_s = \beta_s + \frac{CS_2 - CS_1}{1 + CS_4 \times P} \times \frac{T_b - CS_5 + 10K}{10K}$$

$$\propto_M = \beta_M + \frac{CM_2 - CM_1}{1 + CM_4 \times P} \times \frac{T_b}{10K};\ \xi = 0\ dla\ x \leq 0;$$

$$\xi = CS_7 \times x + (1 - CS_7) \times x^{CS_6} dla\ x > 0$$

$$T_t = CT_1 + CT_2 \times P$$

$$T_b = T - T_t$$

Where:

- β_s - specific volume coefficient in a solid state (1/Pa),
- β_M - specific volume coefficient in a molten state (1/Pa),
- $\propto_s$ - coefficient related to thermal expansion in the solid state (1/K),
- $\propto_M$ - coefficient related to thermal expansion in the molten state (1/K),
- T_t - transition temperature (K),
- T_b - fiducial temperature (K) [35,36].

3 EXPERIMENTS

3.1 MFR

The MFR measurements were conducted in two sets of measurements. In the first set of measurements, we compared the MFR and MVR values of four batches. We made this measurement to show the different flow behaviour of batches on the MFR results. We conducted the second set of measurements to demonstrate how moisture content affects the melt flow behaviour of PA66.

All measurements were done according to ISO 1133 standard (part 2: a method for material sensitive to time-temperature history and/or moisture) at 20°C using Mflow extrusion plastomer (Zwick/Roell).

For the first set of measurements, the material was dried at 100°C for 1 hour with a moisture analyser type MB120 (OHAUS). Table 9 shows the process parameters we used for the first set of measurements.

In the second set of measurements, we measured three samples from the same material batch. We dried the samples at 160°C for 5 min, 15 min, and 30 min. We used the same process parameters for the second set of measurements as for the first set.

Table 9: MFR Measurement Parameters

Standard	Filling Quantity [g]	Climate [°C]	Set Temperature [°C]	Test Load [kg]	Tolerance Present [%]	Position up to Start of Measurement [mm]	Number of Extrudates	Measurement Travel Δs [mm]
ISO 1133-2	8	20	275	5	10	50	10	1.5

3.2 Viscosity

The material was dried at 80°C for 4 hours at 2 mbar pressure for the viscosity measurement with a vacuum dryer type VD23 (Binder GmbH). The residual moisture content was evaluated with FMX HydroTracer (aboni GmbH für Mess und Automatisierungstechnik). The residual moisture amount was approximately 0.0118%.

For the measurements, two different rheometers were used (rotational and high-pressure capillary rheometer). The measurements were done at three different temperatures, 285°C, 295°C, and 305°C, in a shear rate range between 0.001 s^{-1} and approximately 27000 s^{-1}.

3.2.1 Rotational Rheometer

The measurements were done using the rotational rheometer, type MCR501 TD (Anton Paar GmbH). The measurements were performed according to ISO 6721-10

standard in steady state mode in a shear rate range from 0.001 s^{-1} to 1.0 s^{-1} using a plate/plate measuring device PP25 (Ø25) under nitrogen atmosphere to prevent oxidation of samples.

The sample in the shape of plates with a diameter of 25 mm and thickness of 2 mm was made by compression moulding using a vacuum press type P200PV (Dr. Coolin GmbH). The compression moulding conditions can be seen in Table 10.

Table 10: Compression Moulding Parameters

Step	1	2	3	4	5
Temperature [°C]	305	305	305	305	30
Time [s]	3	1	1	1	10
Pressure [bar]	0	25	50	75	100

3.2.2 High-Pressure Capillary Rheometer

A high-pressure capillary rheometer (HPCR), type Rheograph RG50 (Göttfert Werkstoff-Prüfmaschinen GmbH), was used for the viscosity measurements according to ISO 11443 standard. The measurements were carried out in the shear rate range of approximately 100 s^{-1} to 27000 s^{-1} using a 15 mm cylinder and a round die system with a diameter of 1 mm. We used four dies of varying L/D ratios (0.1, 10, 20, and 30) with the entry angle of the die set to 180°. We performed the rheological analysis of measured data to evaluate the shear flow behaviour (wall adhesion) using correction methods developed by Bagley and Rabinowitsch.

3.3 PVT Properties

We measured the specific volume as a function of pressure and temperature using a PVT100 (SWO Polymertechnik GmbH) measuring device.

Before the measurement, the material was dried at 80°C for 4 hours at 2 mbar pressure with a vacuum dryer type VD23 (Binder GmbH). We evaluated the residual moisture of the material with an FMX HydroTracer moisture meter (aboni GmbH für Mess und Automatisierungstechnik). The residual moisture amount was approximately 0.0118%.

We measured the PVT behaviour of the material using a piston apparatus method according to ISO 17744 standard in a temperature range from 40°C to 290°C and in a pressure range from 200 bar to 1600 bar in isobaric cooling mode with a linear cooling rate of 6 K/min.

3.4 Thermal Conductivity

To measure the thermal conductivity of our material, a production of test samples, according to the standard ASTM D7984 (chapter 2.2), was required. The material was dried at 80°C for 4 hours in a dry air dryer (Dryer DP615, Piovan S.p.A).

3.4.1 Production of the Test Specimen

For the thermal conductivity measurement, we produced the shouldered test specimens of type 1A according to ISO 527 standard using an Arburg Allrounder 320C 500–100 injection moulding machine with a screw diameter of 20 mm. Table 11 shows the injection moulding parameters used to produce test specimens. The test specimens were cut with the dimensions 30 x 20 x 4 mm^3 (L x W x H), as shown in Figure 36.

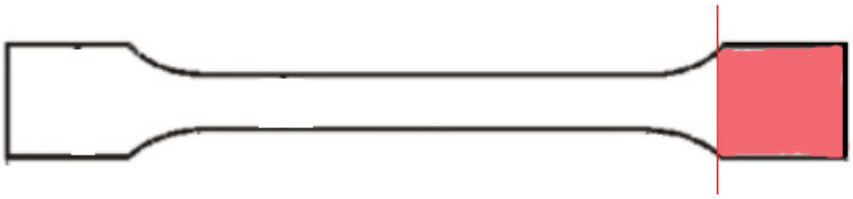

Figure 36: Sampling Position for Thermal Conductivity Measurement

Table 11: Process Parameters for Production of Type 1A Shouldered Test Specimens

Parameter		Value
Barrel Temperature [°C]	Hopper	55
	Z1	270
	Z2	275
	Z3	280
	Z4	285
	Nozzle	295
Mould Temperature [°C]	Ejector Side	85
	Cavity Side	
Injection Speed [cm^3/s]		75
Injection Pressure [bar]		1120
Back Pressure [bar]		50
Packing Pressure [bar]		910
Packing Pressure Time [s]		11
Packing Pressure Switchover Point [cm^3]		10.5
Residual Melt Cushion [cm^3]		8.96
Cooling Time [s]		45
Cycle Time [min]		1.01

We measured the thermal conductivity as a function of temperature at four different temperatures (22°C, 70°C, 285°C, and 305°C). The line source method was used for the measurements in the melt-state according to ASTM D5930-09 standard using the K-System II (Advance CAE Technology Inc.) thermal conductivity measuring device. For the measurement in the solid state, we used a Modified Transient Plane Source method (MTPS) with the thermal conductivity measuring system TCi (C-Therm Technologies Ltd.) according to ASTM D7984 standard.

We measured each method on three independent samples from which we calculated an arithmetic mean value.

3.5 Thermogravimetric Analysis (TGA)

To measure TGA, DMA, DSC, and tensile test, we produced the shouldered test specimens of type 1BA according to ISO 527 standard using a Krauss Maffei KM50-90C1 injection moulding machine. We dried the material at 80°C for 4 hours using a vacuum dryer; the residual moisture amount was approximately 0.01%. We produced three different batches of the PA66 GF30 material with eighty specimens each. The samples were stored after the technologist had determined that the process was stable to ensure the sample material's stability. Samples were cooled and packed in double moisture-resistant plastic bags to reduce moisture intake. Table 12 shows the injection moulding parameters used to produce type 1BA test specimens.

Table 12: Process Parameters for Production of Type 1BA Shouldered Test Specimens

Parameter		**Value**
Barrel Temperature [°C]	Hopper	80
	Z1	270
	Z2	270
	Z3	280
	Z4	285
	Nozzle	295
Mould Temperature [°C]	Ejector Side	85
	Cavity Side	
Injection Flow Rate [cm^3/s]		60
Injection Pressure [bar]		1300
Back Pressure [bar]		15
Packing Pressure [bar]		500
Packing Pressure Time [s]		2
Packing Pressure Switchover Point [mm]		13
Residual Melt Cushion [mm]		8.6
Cooling Time [s]		10
Cycle Time [s]		19

The thermogravimetric analyser with DSC signal TGA/DSC 3+ (Mettler Toledo) was used to inspect the material composition of two batch samples. We cut a small sample from the tensile specimen with a weight of 5mg–12 mg. The sample was heated from 40°C to 500°C with a heating rate of 10 K/min in the N_2 atmosphere (20 mL/min) and then kept at the temperature of 550°C for 30 minutes in the O_2 atmosphere (20 mL/min).

3.6 Dynamic Mechanical Analysis (DMA)

We tested two samples of each batch on the DMA 8000 analyser (Perkin Elmer). We cut the samples using a precision diamond blade saw, as shown in Figure 37. Each sample's thickness and width were measured using a calliper.

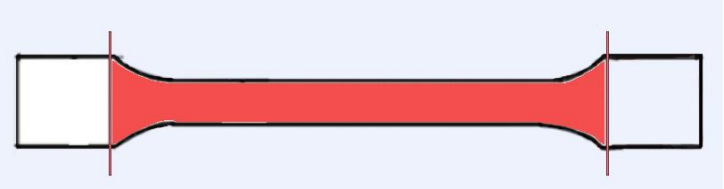

Figure 37: Sampling Position for DMA Measurement

We used a dual cantilever-rectangle measuring system with a frequency of 1 Hz and 0.02 mm amplitude. We analysed all the samples at a temperature range of 25°C to 250°C. The samples were first held at 25°C for one minute and then heated to 250°C at a heating rate of 2°C/min. The batch comparison was made based on the storage modulus *E´* and tan δ.

3.6.1 TTS – Frequency

We examined the time-temperature-superposition principle in the second part of the DMA measurements for one material batch. This measurement function measures the dependence of the storage modulus *E'* on the frequency. This measurement's frequency varies from 0.01 Hz to 100 Hz by 10 frequencies per decade. The temperature range is from 30°C to 250°C with a heating rate of 5°C/min between each segment. Before each temperature segment measurement starts, there is an isothermal heating of 2 min.

3.7 Differential Dynamic Calorimetry (DSC)

To measure the thermal properties of the samples, we used the differential scanning calorimeter DSC 2 (Mettler Toledo). We cut a small sample of the test specimen for the measurement. Each sample weight was inserted in the measurement program before the start of measurement. In general, the samples weighed from 8 to 11 mg. We put the samples into 40 µm aluminium crucibles punctured thrice with tweezers and pressed them together to close the cap. During the sample preparation, material handling was done only with tweezers to prevent the accumulation of grease on the sample, which could affect the measurement results. We measured at temperatures ranging from 0°C to 300°C in a controlled N_2 atmosphere with a continuous flow of gas (20.00 mL/min). The heating and cooling rates were set at 10 K/min.

3.7.1 Relative Crystallinity

We measured the relative crystallinity data for one material batch at five cooling rates (5 K/min, 10 K/min, 15 K/min, 20 K/min, and 25 K/min). These results were used to understand the material crystallization during the cooling phase. Also, the relative crystallinity for two samples of three different batches was measured at a cooling rate of 10 K/min to examine the impact of material composition on the relative crystallinity data.

3.7.2 DSC TOPEM

The specific heat capacity was also measured using a DSC 2 (Mettler Toledo) measuring device. We used the TOPEM program by Mettler Toledo to measure the specific heat, C_p, of one sample from each batch. At the start of the test, we kept the samples at 0°C for 1 minute, then heated them from 0°C to 300°C with a heating rate of 1 K/min. During the heating, the sample temperature was varied every 15 seconds by the tolerance of +/-0.5 K in the controlled N_2 atmosphere with a continuous gas flow (20.00 mL/min).

3.8 Tensile Test

For the mechanical properties of our material, we tested three batches of PA66 GF30 material from BADA on a universal testing machine AG-X plus 10 K (Shimadzu) according to ISO 527 standard. The samples used for measurement were tensile test bars 1BA according to ISO 527 standard. Nine samples of each batch were tested with the testing speed of 1 mm/min until 0.25% strain and 50 mm/s until break. The general sample dimensions were: gauge length 50 mm, sample thickness 2 mm and sample width 5 mm. Before the start of the measurement, we measured each sample's width and thickness using a calliper.

3.9 Material Card Creation in Moldex3D

The Moldex3D technical support team assisted us in creating the material card in Moldex3D software. For the material card data, we used the material properties from the technical data sheet (TDS) from BADA, along with the measured PVT data, thermal conductivity, specific heat capacity, viscosity, and relative crystallinity. We used the following mathematical models for the material properties:

- Modified Cross Model (3) (viscosity),
- Modified Tait model (2) (PVT),
- Nakamura model (relative crystallinity),
- Tabulated data (specific heat),
- Tabulated data (thermal conductivity).

We used generic data for PA66 GF30 from Moldex3D for the viscoelasticity, structure VE, and fibre information. Appendix 1 shows all the data used to create the material card.

3.10 Part Sample Production and Scanning

Figure 38 shows the two housing parts we used to validate the material card. We produced the two parts using a four-cavity mould (two cavities per housing) with a Sumitomo Demag IntElect 130–560 injection moulding machine. Table 13 shows the process parameters used for the IM of the two parts. We heated the material PA66 GF30 used for injection moulding at 80°C for 4 hours. The residual moisture amount was approximately 0.0118%. After injection moulding, the parts were 3D scanned using a Metrotom 1500 (Zeiss) CT (computerized tomography) scanner.

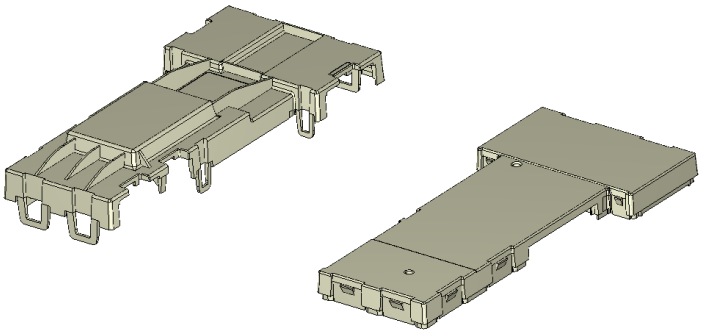

Figure 38: Two Housing Parts

Table 13: Process Parameters for Injection Moulding of the Two Housing Parts

Parameter		**Value**	
Barrel Temperature [°C]	Hopper	60	
	Z1	270	
	Z2	290	
	Z3	300	
	Z4	300	
	Nozzle	300	
Mould Temperature [°C]	Ejector Side	90	
	Cavity Side		
Flow Rate [cm^3/s]		30	90
Injection Pressure [bar]		1600	1600
Back Pressure [bar]		40	
Packing Pressure [bar]		600	
Packing Pressure Time [s]		3	
Packing Pressure Switchover Point [mm]		9	
Residual Melt Cushion [mm]		7	
Cooling Time [s]		12	
Cycle Time [s]		24	

3.11 Measuring Report Creation in Polyworks

3D dimensional analysis software PolyWorks Inspector (InnovMetric) was used to assess the part's deformation and compare it with the simulated deformed 3D model. The dimensional analysis software allowed us to compare the approximate dimensions of the part after deformation, obtained from the simulation software, with the original CAD model. By using dimensional analysis software, we could check that the approximate dimensions of our part were within tolerance so that we could accurately assess the deformation trends of each part, and define a measurement protocol for any additional deformation analysis. Figure 39 shows the datum features for both housing parts; we set the datum features according to the customer drawing. The measured features of both parts are shown in Appendix 5; figures show the measurement results of the scanned part.

Figure 39: Datum Features of the Lower Housing (left) and the Upper Housing (right)

3.12 Injection Moulding Simulation

We used Moldex3D software for the injection moulding simulation of the two parts. The runner system and the cooling channel geometry were created from the IM tool 3D model using Creo parametric software, as shown in Figure 40. To enhance the numerical stability of the IM simulation and mitigate complications related to the meshing and solving, the 3D model geometry underwent a process of cleaning and simplification. We imported the cooling channels, runner curves, and the corresponding housing parts into the Moldex3D software. The runner geometry was made in Moldex3D because this allows us to set symmetry boundary conditions, thus reducing calculation time and ensuring suitable mesh thickness. We set the runner

system dimensions according to the IM tool 3D model. Figure 41 shows the prepared model in the Moldex3D numerical simulation software. The two housing parts were meshed using a 5-layer BLM-type mesh. To define the mesh thickness setting for further analysis, we checked the part warpage result convergence using different mesh thicknesses to reduce unnecessary calculation time. We used an alternate material PA66 GF30 Ultramid A218V W30, for mesh definition. Based on the total warpage displacement, the results are shown in Table 14; we used 0.6 mm mesh thickness for further analysis.

Table 14: Mesh Selection

Mesh Thickness [mm]	Part Solid Mesh Element Count [x10^6]	Part Surface Mesh Element Count [x10^3]	Warpage Total Displacement [mm]
1.2	0.56	84	0.683
1.0	0.71	107	0.695
0.8	1.01	152	0.706
0.6	1.74	262	0.724
0.5	2.49	373	0.722

We made the IM simulation using a 0.6 mm thick 5-layer BLM-type mesh. Created PA66 GF30 material card was analysed, along with the created material card using PVT data made with decreasing pressure steps and some alternate PA66 GF30 material cards. For the IM simulation, we used the machine mode setting to achieve as matching parameters and behaviour of the IM process as possible. We set the process parameters for the IM simulation based on the process parameters of the two housing parts; Table 15 shows the IM process parameters used in Moldex3D. Table 16 shows machine parameters set according to our IM machine. We set the mould size according to the tool dimensions (396 x 496 x 319 mm^3). For the IM simulation, we used transient fill-pack-cool-warp analysis.

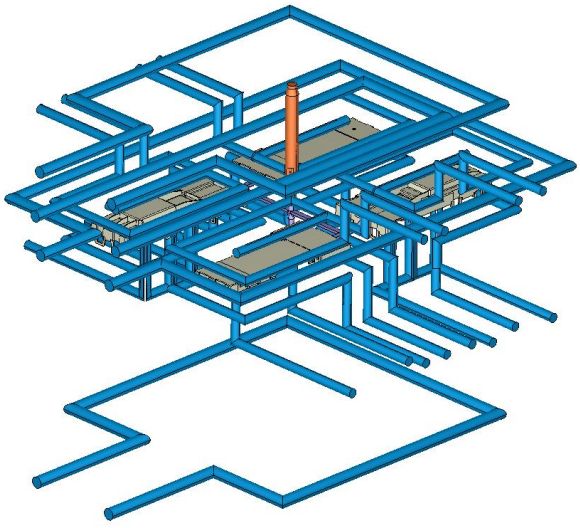

Figure 40: Prepared 3D Model From the IM Tool 3D Model

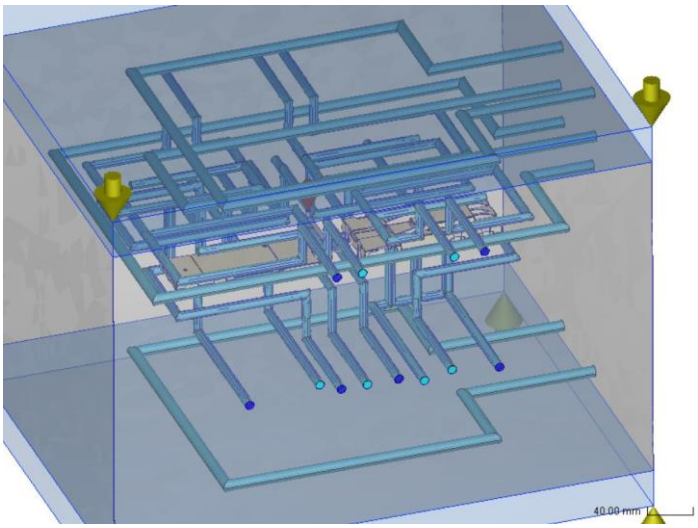

Figure 41: Prepared Model for the IM Simulation in Moldex3D Software

Table 15: IM Simulation Process Parameters

Parameter	**Value**				
Setting Method	Machine Mode 1 (by profile)				
Flow Rate Profile					
Profile Type	Polyline				
Suck Back [mm]	5				
Ram Position [mm]	0	9	15	25	85
Injection Velocity [mm/s]	25	25	30	90	100
Injection Pressure Profile					
Ram Position [mm]	0	9	85		
Injection Pressure [MPa]	60	60	160		
VP Switch-Over- by Ram Position [mm]	9				
Packing Pressure [MPa]	60				
Packing Time [s]	3				
Mould Temperature [°C]	90				
Melt Temperature [°C]	300				
Plasticizing					
Back Pressure [MPa]	4				
Screw Speed [rpm]	130				
Barrel Temperature					
Zone	Nozzle	1	2	3	
Temperature [°C]	300	300	290	270	
Cooling Settings					
Cooling Method	General				
Initial Mould Temp [°C]	90				
Air Temperature [°C]	25				
Eject Temperature [°C]	223				
Cooling Time [s]	12				
Mould-Open Time [s]	5				
Coolant Inlet Temperature [°C]	90				
Coolant Inlet Pressure [bar]	5				
Mould Metal Material	1.2343				

Table 16: IM Simulation Machine Settings

Parameter	Value
Maker	Sumitomo Demag
Grade	IntElect 2
Screw Diameter [m]	35
Screw Stroke [mm]	160
Shot Weight [g]	154
Max Injection Pressure [MPa]	280
Max Injection Rate [cm^3/s]	192
The Time Constant of Injection Speed	0.01
The Time Constant of Injection Pressure	0.1
Nozzle Volume [cm^3]	154
Max Pressure Slope [MPa/s]	2500
Machine Type	Electric
Clamping Force [t]	143

3.13 Material Card Properties Testing

The created material card properties and their effect on max filling pressure and warpage were tested by simulating and analysing the result of the created material card. Appendix 5 compares viscosity, PVT, specific heat, relative crystallinity, and thermal conductivity data with two alternate PA66 GF30 material cards. We compared the approximated sprue pressure and part dimensions.

We prepared a simple design of experiment (DOE) to test the effect of the material card properties on the simulation results. Our research aims to understand the impact of the material card data on the IM simulation filling pressure, estimated total warpage displacement, and dimension results.

We performed the experimental trials using Moldex3D simulation software. We interpreted the IM simulation results in the JMP statistical software. With our DOE, we want to show the impact of each material card data on the IM simulation results. Understanding the effect of each material card's properties and their correlation helps R&D engineers to work on IM simulation software. By understanding the correlation between the material card properties and their effect on the IM simulation results, we can optimise process parameters, predict and understand the issues of material card data, and enhance alternate material selection and optimisation of our created material card.

Of course, many factors affect the IM process and simulation. However, with a proper understanding of the effects of material card data on IM simulation results, we can reduce possible misinterpretation and prevent using bad material cards. There are many parameters and material properties used in the material cards. In our DOE, we focus on the PVT, viscosity, thermal conductivity, and crystallization rate because we expect these would significantly impact our analysed parameters. The factors and the

study domain are shown in Table 17. We increased or decreased our measurement values of the selected material card properties for the coefficient of variation (CV). Using the varied measured data, we recreated the mathematical model parameters. Having four factors, each taking two levels, we decided to use a 2^4 full factorial DOE. Hence, we ran 16 IM simulation runs, where for each run, we varied the selected four material properties according to the selected CV.

Table 17: Factors and Study Domain

Factor	Low Level (–1)	High Level (+1)
PVT	–3%	+3%
Viscosity	–10%	+10%
Thermal Conductivity	+5%	–5%
Crystallization Rate	–5%	+5%

4 RESULTS AND DISCUSSION

4.1 Results of the Material Characterisation

4.1.1 MFR

Measurement Set 1

Table 18 shows the results for the first set of MVR measurements. From the results, we can see that with different batches, the MFR and MVR value also changes. MVR value deviation between different batches is mainly due to the change in the composition of the material. When material suppliers prepare the polymer materials with additives and reinforcing fibres, achieving the same material composition is difficult due to several factors. These include the inherent variability of raw materials, variations in reaction kinetics and side reactions, and the influence of the process parameters. Thus, material suppliers provide information regarding the tolerance of each component in the composite. The automotive industry formed the international material data system (IMDS) to facilitate access of the companies to material composition data of suppliers. Table 19 shows the material composition of our PA66 GF30 material. The provided material composition data was vital in the measurement analysis of the master's thesis, as can be seen in Figure 42: Set 1; the green and purple-coloured batches are inside the tolerance, while the blue and gold coloured are outside the tolerance. In general, the supplied material is prechecked by the supplier using an MFR measuring device; thus, all material samples should be tolerable.

The resulting batch variation primarily results from moisture content and batch material composition. In our case, we dried all the samples with the same procedure. The time and temperature of the drying process have been changed and do not correspond to the specifications in the technical data sheet for production (80°C for 2–4 hours), as a longer drying time is required.

Regarding the moisture content of the material, the drying program was changed from 15 min to 60 min at 100°C due to the significant moisture content of some older samples. In the 60-minute program, all the samples were dried entirely and quickly transferred to the MFR instrument.

The sample handling and device preheating was done according to ISO 1133-2 standard. We, therefore, suspect that the main factor for the significant deviation is the material composition. The example of the batch material content variation can be observed in the DSC results. The standard deviation of all samples was within expectations. The trend of MFR values with each extruded sample remained the same during the measurement, which was another indicator that the test was stable.

In conclusion, moisture content and material composition deviations are the two leading causes of the MFR deviation. The material composition can vary within the

tolerance of the supplier. Differences in material composition are shown in the following measurements. The moisture content of the measured samples should be within the allowed values.

Table 18: MFR and MVR Results for Set 1

Batch Number	Average MFR [g/10 min]	Standard Deviation [g/10 min]	Average MVR [cm³/10 min]	Standard Deviation [cm³/10 min]	Allowed MVR Value [cm³/10 min]
23200073	76.30	0.95	62.84	0.69	55±10
23020076	72.18	1.31	59.87	0.68	
23100084	61.10	0.75	50.29	0.72	
23140041	71.67	0.85	57.58	0.69	

Table 19: Selected PA66 GF30 IMDS Material Composition

Component	Content [wt %]
PA66	66.6
GF	30±2
Further Additives (not to declare)	2±1.5
Pigment Portion (not to declare)	1.4±1.1

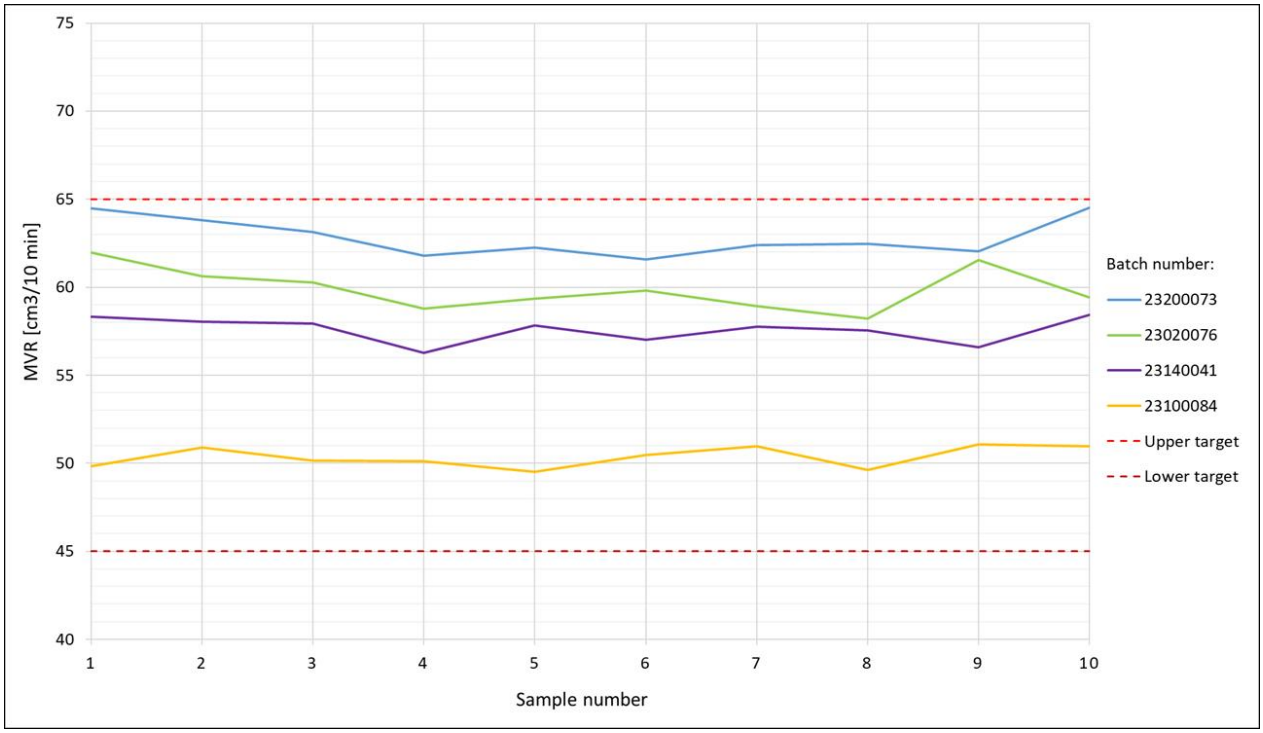

Figure 42: Set 1; MVR Values for 4 Different Batches, Each Measured With 10 Samples; Upper and Lower Tolerance Limit

Measurement Set 2

Measurement set 2 was performed to show the effects of the moisture content on the MFR of PA66. As shown in Figure 43, the MVR values dropped significantly with the increase in drying time. The MVR value drop indicates that the samples that were dried for 5 min and 15 min were not wholly dried as compared to the results of the 30 min drying samples and the supplier MVR value of this batch. Also, with high moisture content, the standard deviation of the extrudates reaches a value over 1.11, which might indicate that the samples still had some moisture, as seen in Table 20.

As we can see, with less moisture, the flow rate of the material decreases significantly. Thus, to correctly compare two different batches, both materials must have a similar moisture content to exclude the effect of moisture on the MFR results. The sample, which was dried for 30 min, is comparable in its MVR value to that provided by the supplier with 57.20 cm^3/10 min.

Table 20: MFR and MVR Results for Set 2

Drying Time [min]	Average MFR [g/10 min]	Standard Deviation [g/10 min]	Average MVR [cm^3/10 min]	Standard Deviation [cm^3/10 min]	Allowed MVR Value [cm^3/10 min]
5	95.83	2.25	79.60	1.11	55±10
15	80.09	0.85	64.45	0.57	
30	65.86	1.34	54.08	0.87	

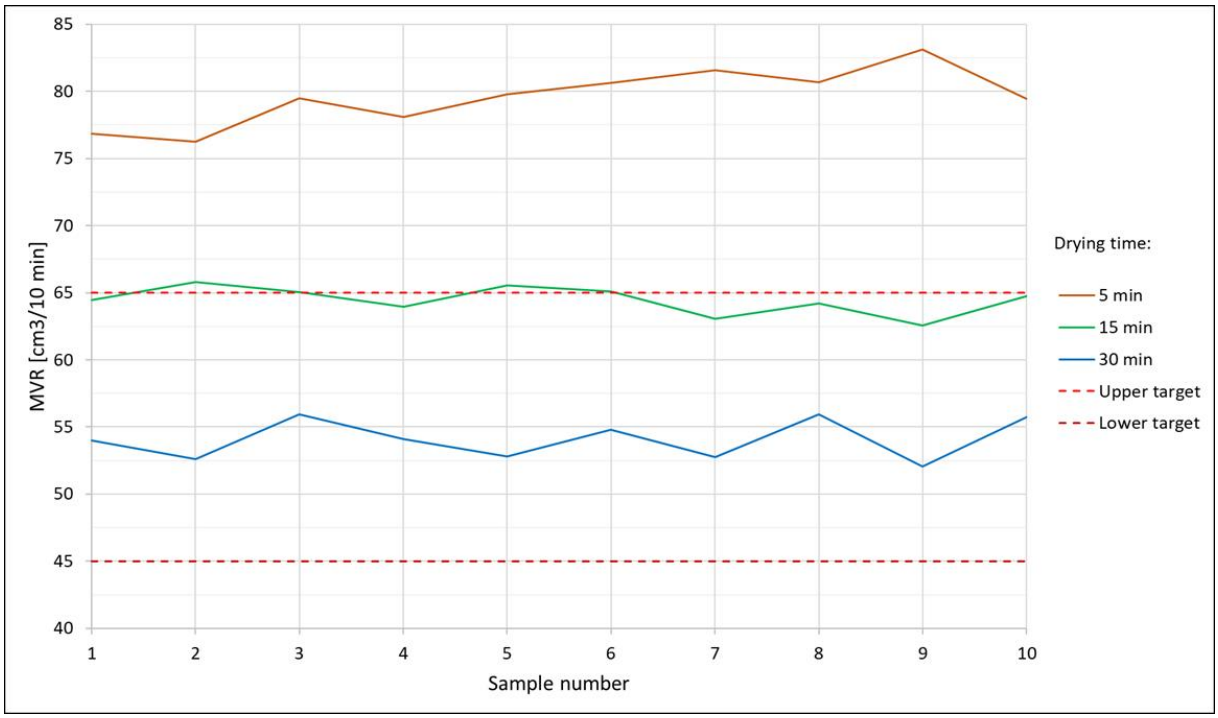

Figure 43: Set 2; MVR Values for 3 Different Drying Times, Each Measured With 10 Samples; Upper and Lower Tolerance Limit

4.1.2 Viscosity

The viscosity was measured using a rotational rheometer in the shear rate range from 0.001 s^{-1} to 1.00 s^{-1}. Due to the high GF content, the material started to leak out of the measuring gap at shear rates above 0.14 s^{-1}. Thus, the measured viscosity values above 0.14 s^{-1} were not used for the calculations. The material shift from the plate/plate can be seen in Figure 44.

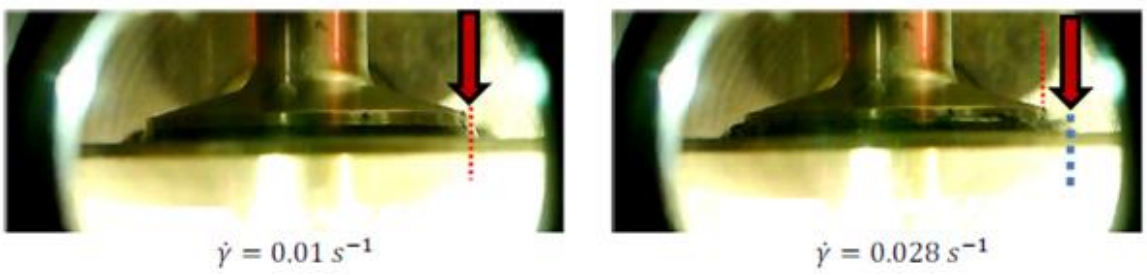

Figure 44: Sample Position During Viscosity Measurement With Plate/Plate Rheometer at Two Shear Rates

The measured viscosity with a rotational and high-pressure capillary rheometer (HPCR) at three different temperatures can be seen in Figure 45.

We made the first approximation of the measured viscosity using the Cross-WLF model. The approximation of the measured values from the rotational rheometer in a shear rate range from 0.001 s^{-1} to 0.14 s^{-1} and all the measured values from the HPCR were used. The measured and approximated viscosity using the Cross-WLF model can be seen in Figure 46. This approximation did not yield satisfactory results; thus, we made two additional approximations.

We performed the second approximation with a reduced shear rate range from the rotational rheometer data; all data from the HPCR was used. We made this approximation using the Cross-WLF model. As we can see from Figure 47, better results were obtained as compared to the first version.

For the third version of the mathematical description of the viscosity curve as a material law, we used the Cross-WLF material model in combination with the Herschel-Bulkley extension. This approach is often used when describing the flow of thermoplastic materials with high filler content in low shear rate ranges. In the case of our master's thesis, we were more interested in the viscosity behaviour in the higher shear rate range; thus, we used the second approximation to create the material card. The third approximation using Cross-WLF approximation with Herschel-Bulkley extension can be seen in Figure 48.

For research purposes, we created an additional viscosity approximation to verify if the rotational rheometer measurements are needed as material data for the IM simulation. Thus, only HPCR measured data was used with the Cross-WLF model, as shown in

Figure 49. As presented in the figure, the approximation with Cross-WLF using only HPCR data and extrapolation down to low shear rates could lead to inaccurate results.

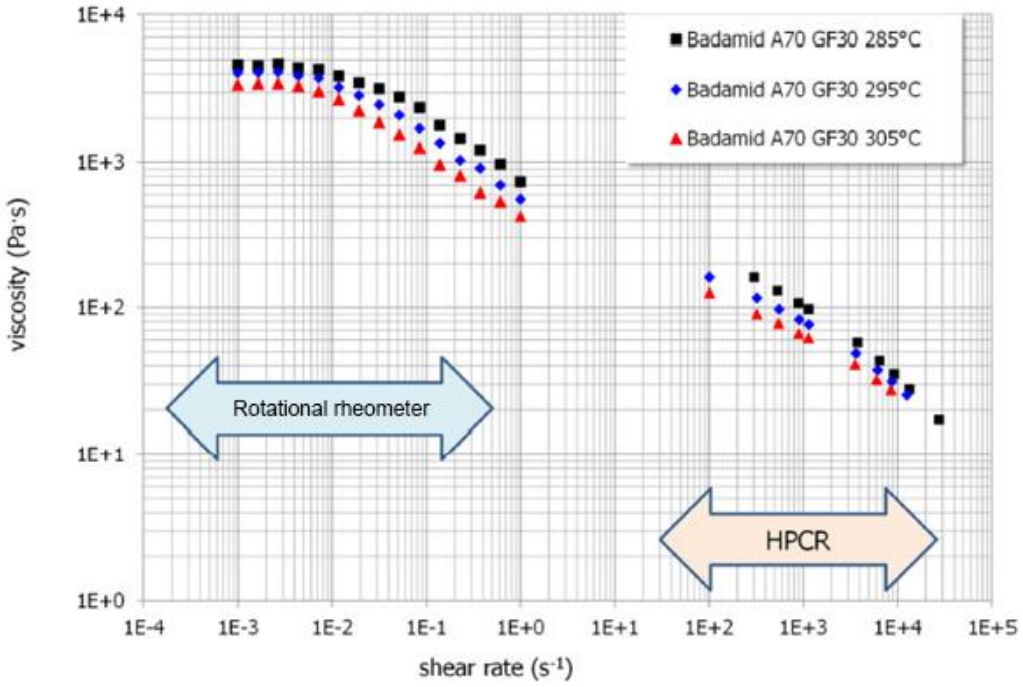

Figure 45: Viscosity Values With a Rotational Rheometer and HPCR

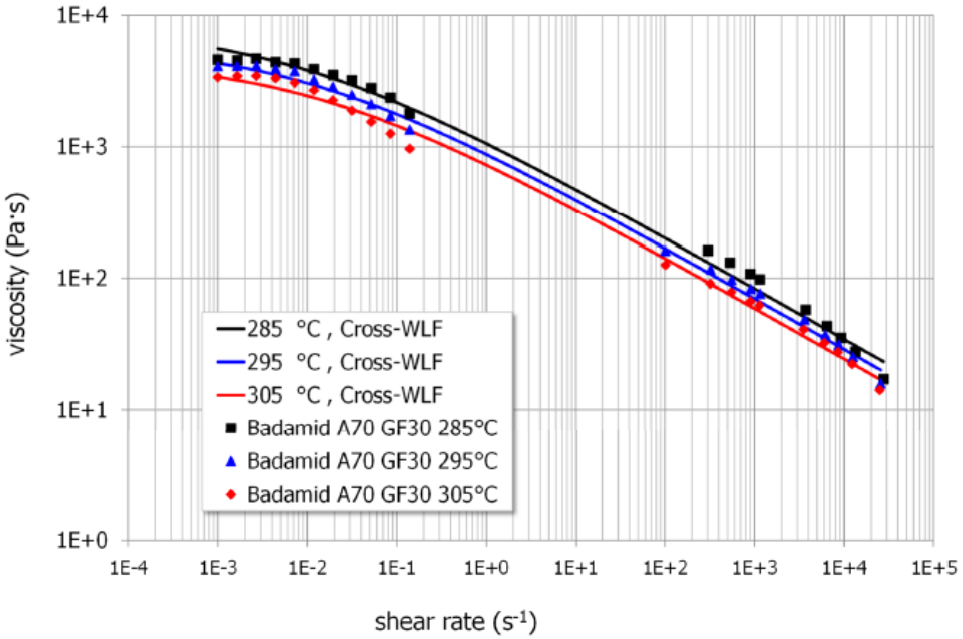

Figure 46: Viscosity Data Points (symbols) and Approximated Viscosity Data (lines) Using the Cross-WLF Model (first approximation)

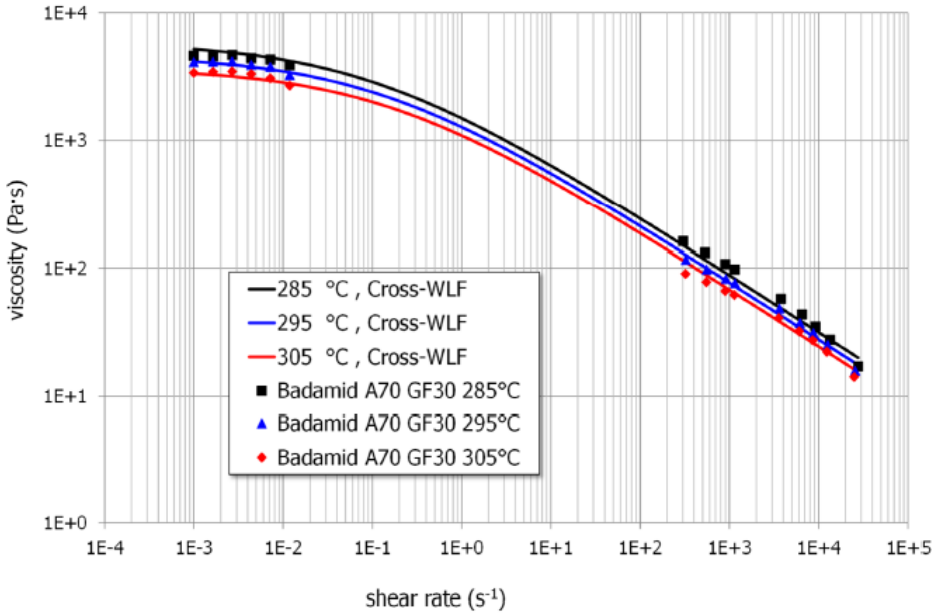

Figure 47: Viscosity Data Points (symbols) and Approximated Viscosity Data (lines) Using the Cross-WLF Model (second approximation)

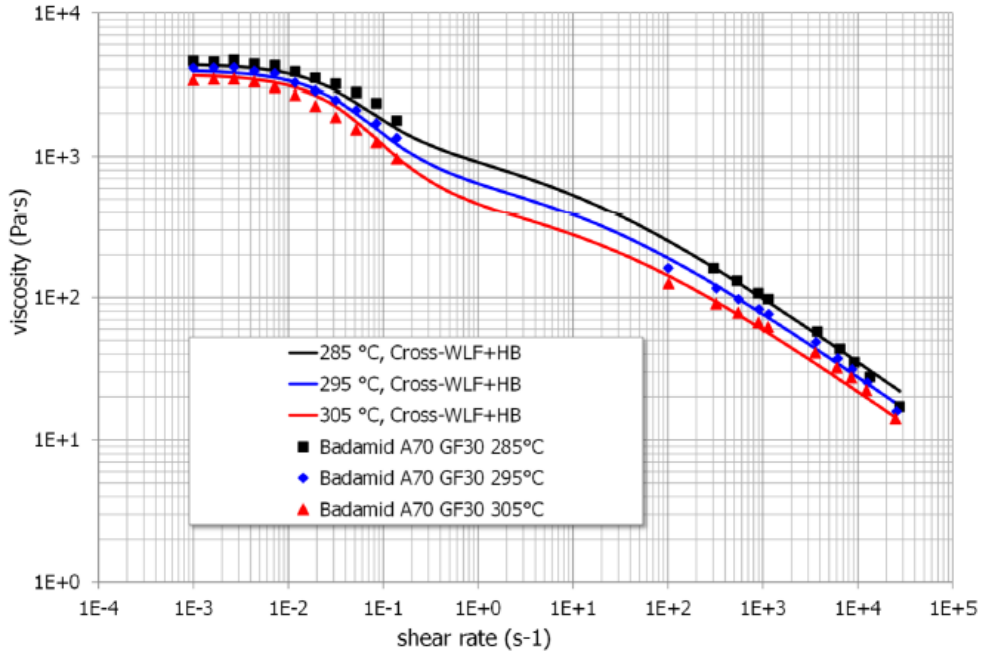

Figure 48: Viscosity Data Points (symbols) and Approximated Viscosity Data (lines) Using the Cross-WLF Model in Combination With the Herschel-Bulkley Model (third approximation)

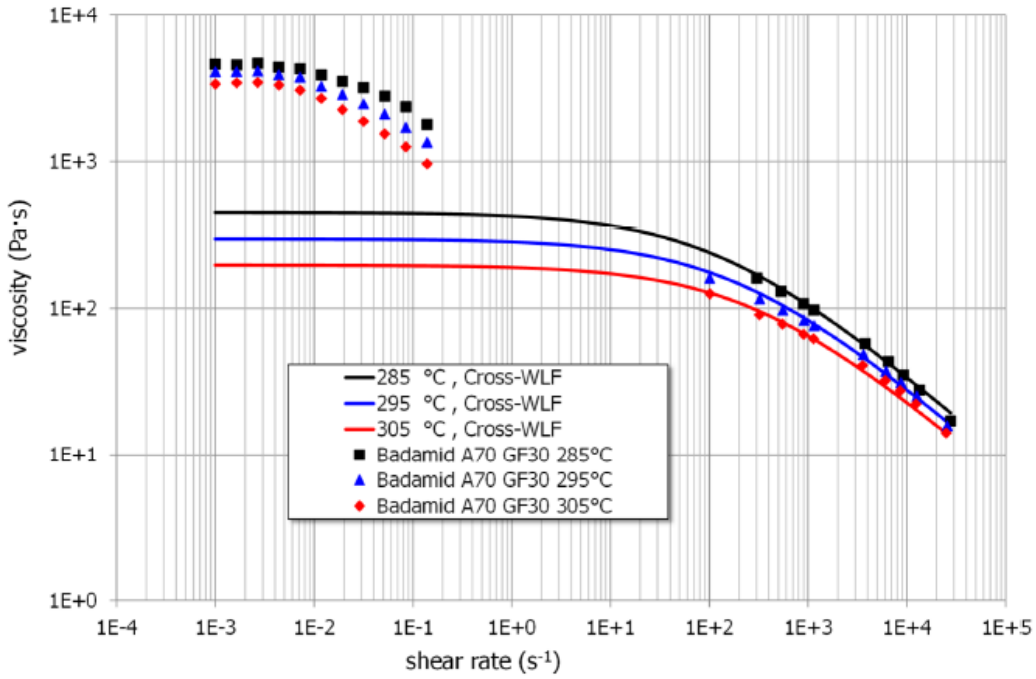

Figure 49: Viscosity Data Points (symbols) and Approximated Viscosity Data (lines) With the Cross-WLF Model Using Only HPCR Measured Data (fourth approximation)

4.1.3 TGA

In Figure 50, the comparison of the TGA curves of six samples is shown. In contrast, the exact composition of the batches and their DTG peaks are shown in Table 21. In general, the sample results are pretty similar and show little deviation. The measurement shows some interesting points. Firstly, samples 2 and 3 had 0.2% to 0.3% lower concentration of other substances, which is still inside the material producer's tolerance zone. Secondly, the GF and polymer matrix content slightly varied, but nothing unexpected showed. Thirdly, all sample degradation temperatures were around 425°C with a slight deviation. We can observe slight differences between the measured samples from the DTG curve (top right corner of Figure 50). We expect this is due to the different material composition of samples, but in general, these differences are negligible.

Table 21: TGA Samples Composition and DTG Peaks

Batch Number	Sample Number	Polymer Matrix [%]	GF [%]	Other [%]	DTG Peak [°C]
23020076	02	69.37	29.74	0.89	425.22
23020076	03	67.87	31.23	0.9	424.31
225110003	04	68.49	30.29	1.22	425.19
225110003	05	68.25	30.75	1.00	424.33
225110004	06	68.23	30.65	1.12	425.98
225110004	07	68.71	30.11	1.18	424.99
Standard Deviation	/	0.52	0.56	0.14	0.63

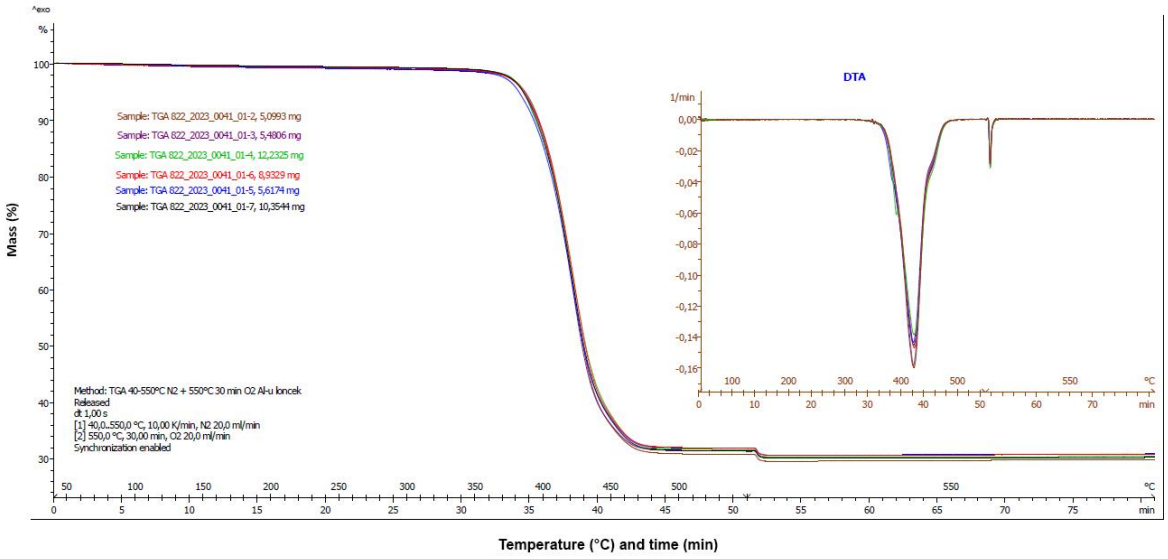

Figure 50: TGA and DTG Curves of Three Measured Batches, Two Samples Each

4.1.4 DMA

With the DMA analysis, we measured the storage and loss moduli (*E´* and E'') and the tan delta of three batches, two samples in each batch. The tan delta and storage modulus results can be seen in Figure 51 and Figure 52; the tabulated results are shown in Table 22. Based on our measurements, we can conclude that the tan delta, i.e., the ratio between loss and storage modulus, for different batches remains the same. Moreover, some deviation in measuring of the storage modulus could be observed. Sample one showed the highest deviation in comparison to the other samples.

This large deviation may be due to differences in sample thickness or the composition of the sample material. Based on the TGA results, it would be hard to conclude that this is due to a slight material composition change. Also, the sample thicknesses were roughly the same, and the measurement procedure remained the same during the measurement of each sample. The moisture content could be a factor that was not measured, but all samples were stored in double moisture-resistant plastic bags and generally had the same conditions; thus, this would not be the case. Also, with moisture content, storage modulus generally rises. As we can see, the second sample of this batch had a similar storage modulus as compared to the other four samples; thus, this could be due to uneven sample embedment on the DMA device. The measured glass transition showed a slight deviation between measurements. On average, the T_g of the material was around 69°C.

Table 22: DMA Data of Six Measured PA66 GF30 Samples

Batch Number	Sample Number	Tan Delta	Storage Modulus *E'* at 30°C [MPa]	T_g [°C]
23020076	01	0.081	6372	69.60
23020076	02	0.081	5606	69.92
225110003	03	0.082	5557	69.84
225110003	04	0.081	5330	68.75
225110004	05	0.079	5389	67.54
225110004	06	0.080	5403	68.04
Standard Deviation	/	0.001	388.22	1.00

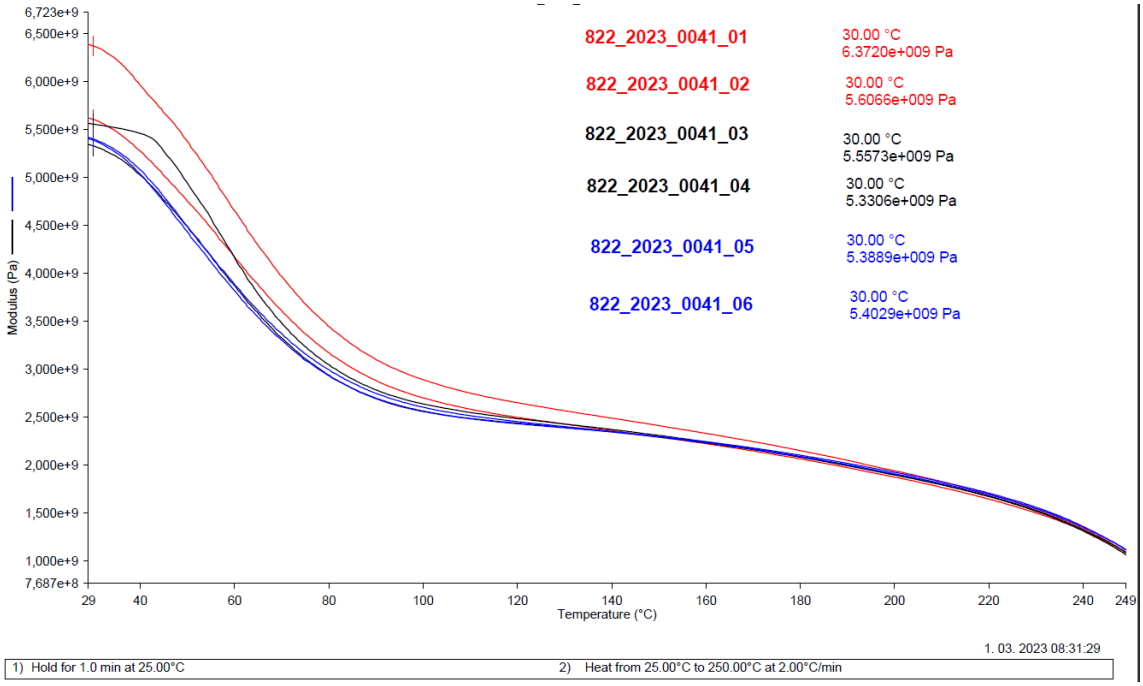

Figure 51: DMA Curves of the Storage Modulus E´ of Measured Samples

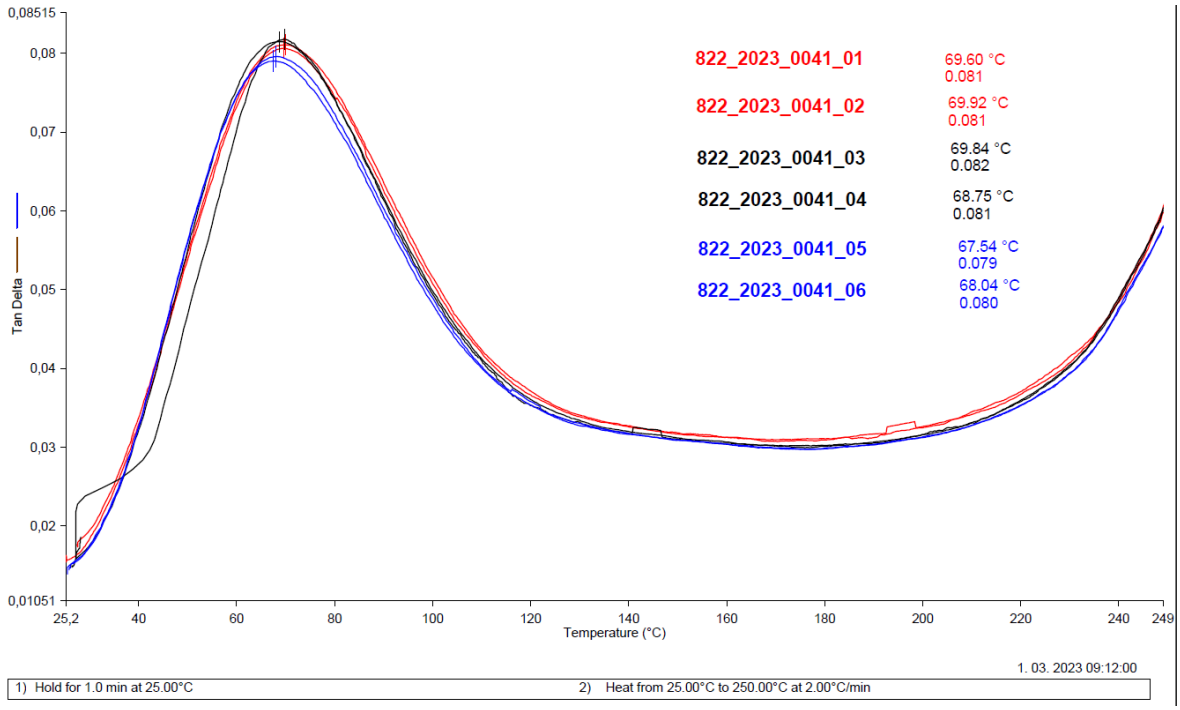

Figure 52: DMA Curves of the Tan Delta of Measured Samples

Using the TTS technique, we analysed the storage modulus and tan delta of one material batch at various temperatures and frequencies. Figure 53 shows the measured material's storage modulus vs. frequency behaviour. We can see that with the increase in frequency, the storage modulus increases, which indicates that the material becomes rigid. Thus, the oscillation amplitude due to natural frequency will be much lower. E' increased up to two times from 1 Hz to 10^9 Hz, which shows high-frequency dependence. The slope of the modulus curve is steepest between 1 Hz and 10^5 Hz, meaning the material exhibits a significant change in viscoelastic behaviour within this frequency range. At frequencies above 10^7, the material's viscoelastic behaviour becomes more stable, and the effect of frequency on the material's relaxation mechanism is much smaller than at lower frequencies.

Tan delta dependency on temperature is shown in Figure 54. The tan delta's peak represents the polymer's glass transition, which, as seen in the figure, is at 70°C. At 100 Hz, the glass transition shifts from 70°C to 80°C. This observed phenomenon can result from molecular restructuring or some restriction of the movement of polymer chains. The area under the tan delta curve indicates the total amount of energy the material can absorb. The tan delta peak value increased in the frequency range of 0.1 Hz to 10 Hz, meaning the material gained more energy dissipation potential. Tan delta values decreased in the frequency range above 10 Hz, indicating that the material exhibited a more elastic response.

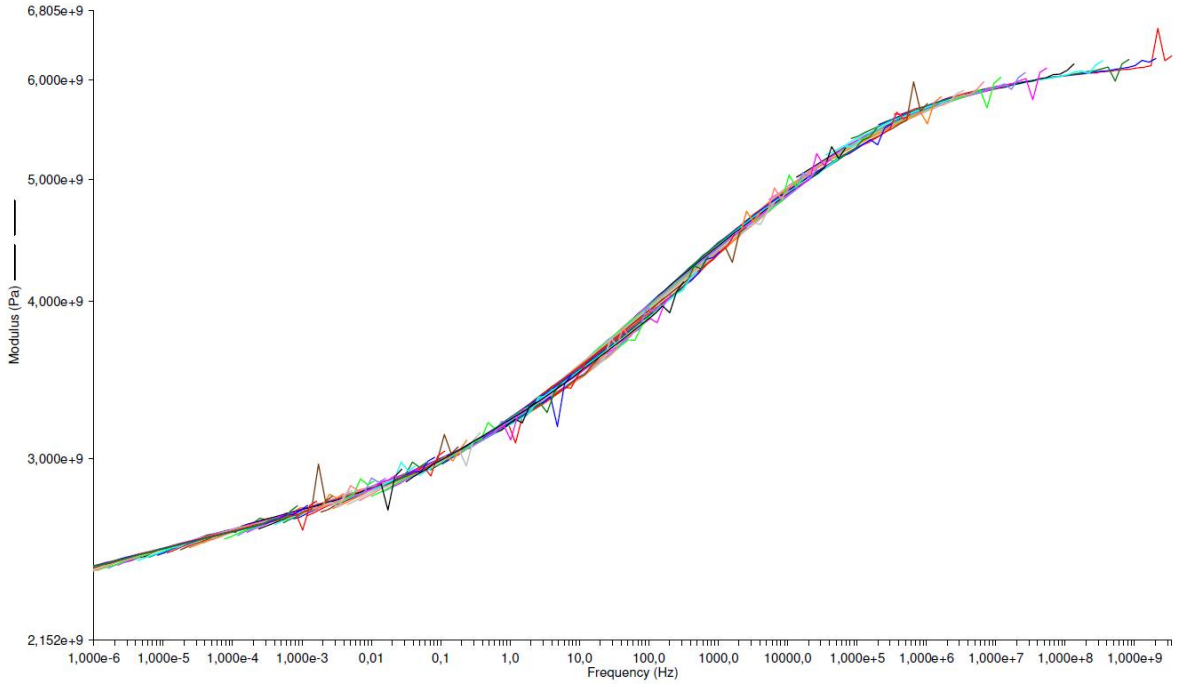

Figure 53: Storage Modulus E´ vs Frequency of Measured Sample

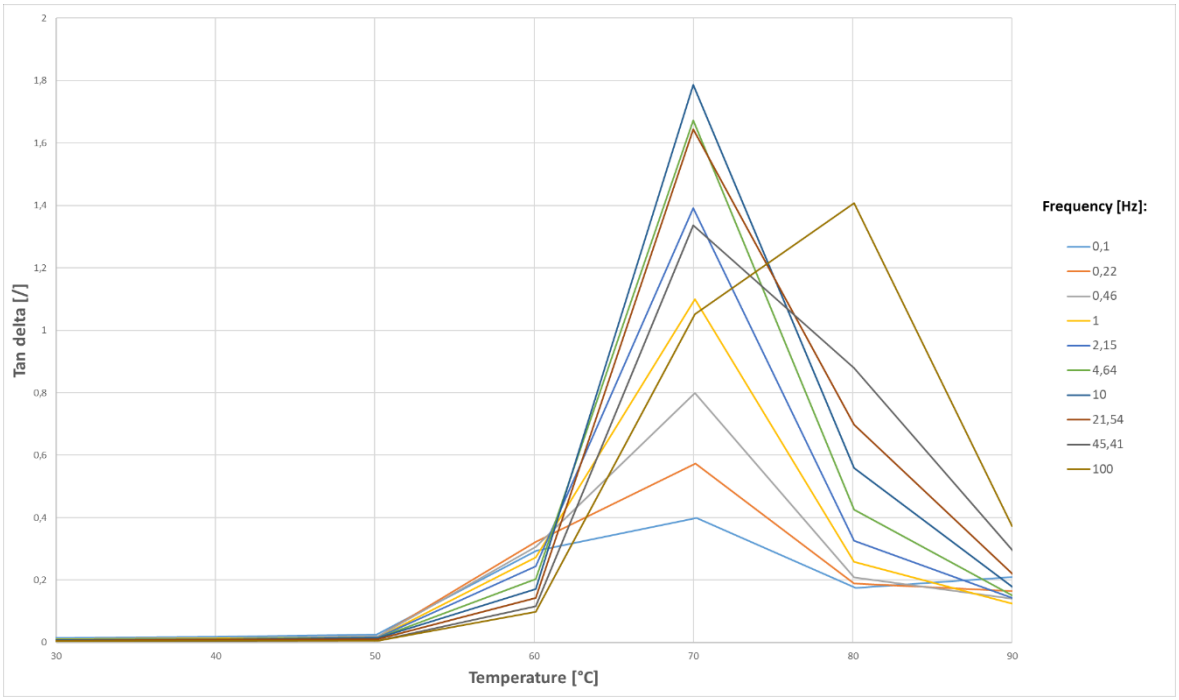

Figure 54: Tan Delta vs Temperature of the Measured Sample

4.1.5 DSC

Table 23 summarises the thermal events during heating and cooling along with the associated enthalpies, enthalpy of crystallization (ΔH_c) and the enthalpy of melting (ΔH_m). T_m and T_c thermal events did not change drastically between batches; these differences are negligible when comparing their enthalpy values. A more significant

difference can be seen by comparing the T_g of each sample; this could be due to the measured data processing. Calculating the exact T_g of PA66 GF30 is difficult due to the slight slope transition, which can be seen in Appendix 3; in this case, the data from DMA should be more accurate. The melt temperature T_m is consistent with the T_m value from the TDS. We calculated the degree of crystallinity of each sample, and the measured degrees were very comparable; sample number 04 stands out the most. Sample 05, which was also from the same batch, showed higher crystallinity values. Thus, we cannot connect the lower measurement of the degree of crystallinity to the batch. With more measurements, we expect the results to be more or less the same. Excluding sample 04, the standard deviation of the degree of crystallinity of the measured samples is 0.2, which is very good. In conclusion, we experienced minor differences between observed batches, but the results generally showed nothing unexpected.

Figure 55 shows the results for relative crystallinity results. From the results, we can observe the crystallization behaviour of the material at five different cooling rates. At higher cooling rates, the crystallization starts later than at lower cooling rates. Also, with the increase in cooling rate, the crystallization enthalpy increased. To conclude, the relative crystallization results look as expected.

We used the DSC TOPEM method to measure the material-specific heat capacity; the DSC TOPEM results are shown in Appendix 4. Some variations between measured batches have been shown, possibly due to poor sample geometry or material composition. Samples 10 and 11 required some data modifications after measurement. For sample 03, this was not necessary; therefore, we decided to use sample 03 for the material card. The peak on the figure represents the T_m thermal event, which is consistent with DSC measurement and material TDS. The sample number with the corresponding batch number is demonstrated in Table 24. We compared the specific heat at 25°C of three measured samples. The results show a deviation between the measured specific heat values, which was expected to some extent since the sample composition of each batch varies. All samples were cut at the same section on the part, but the actual glass fibre content variation between samples remained. Sample geometry and the surface area also affected the specific heat measurement, as they affected the heat transfer and the thermal behaviour of the measuring material. Sample 03 has the most comparable thermal conductivity to that of PA66 in literature, which is roughly 1.3 $J/g^{-1}°C$; thus, we used the specific heat measurement results of sample 03 for the material card data in Moldex3D.

Table 23: Results of the DSC Analysis of Samples PA66 GF30

Batch Number	Sample Number	T_m [°C]	ΔH_m [J/g]	T_c [°C]	ΔH_c [J/g]	T_g [°C]	X_c [%]
23020076	01	258.01	42.95	232.02	33.08	52.80	4.37
23020076	02	257.65	44.17	232.03	34.57	50.95	4.25
225110003	04	258.80	39.53	230.17	33.17	59,47	2.81
225110003	05	258.94	35.99	229.86	25.99	51.98	4.42
225110004	07	258.28	40.72	231.04	30.32	53.83	4.60
225110004	08	258.04	40.13	230.66	31.02	57.68	4.03
Standard Deviation	/	0.5	2.86	0.92	3.05	3.38	0.65

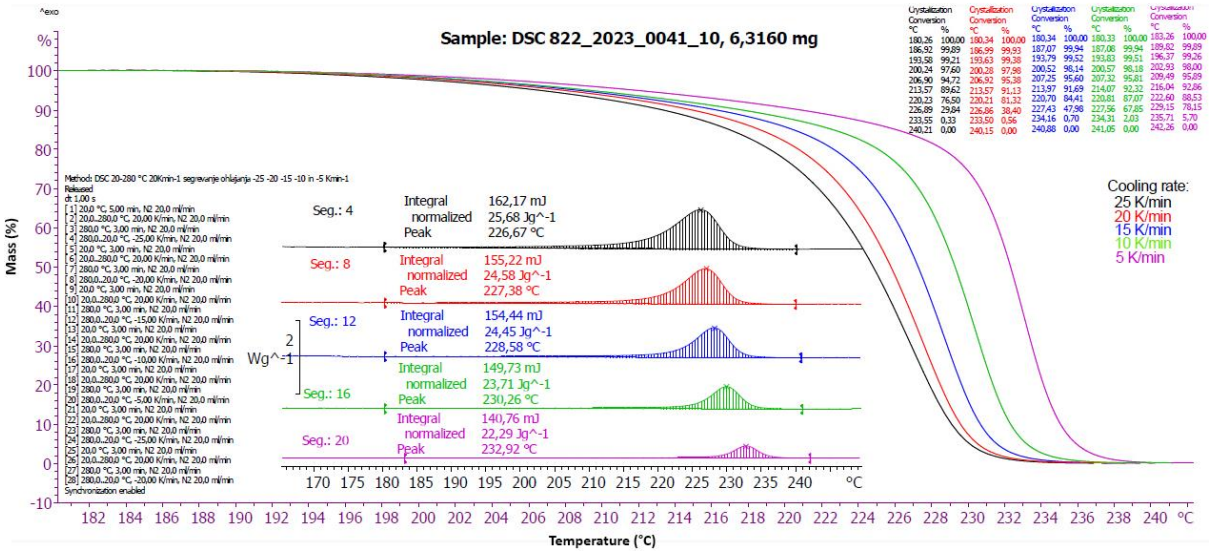

Figure 55: DSC Curves for the Relative Crystallinity of Samples PA66 GF30

Table 24: Results of the Specific Heat of Samples PA66 GF30 Using the DSC TOPEM Method

Batch Number	Sample Number	Specific Heat at 25°C [J/g·°C]
23020076	03	1.29
225110003	10	0,95
225110004	11	1.9

4.1.6 Tensile Test

We noticed some differences between all samples. Table 25 summarises data for the average values of all three batches for modulus of elasticity (E), tensile strength (σ_M), elongation at tensile strength (ε_M), and elongation at break (ε_B). The results show some variation, as expected, due to the differences in the material composition. Sample 01 showed a slightly lower elongation compared to the other two batches. Lower elongation value could be due to the different material composition. We can see a lower content of other substances from the TGA data compared to the other two batches; thus, slightly more polymer or GF could be present.

Nevertheless, more material samples should be measured on the TGA analyser for an accurate assessment. Compared to the TDS data, the modulus of elasticity is quite similar. The standard deviation for nine samples of each batch was below 0.8 GPa. The results of each batch can be seen in Appendix 2.

Table 25: Tensile Test Results With Average Values of 9 Samples PA66 GF30 for Each Batch

Batch Number	Sample Number	E (GPa)	σ_m (MPa)	ε_m (%)	ε_B (%)
23020076	01	6.93	171.6	7.03	7.25
225110003	02	6.64	170.0	9.05	9.31
225110004	03	6.69	169.8	8.64	8.92
Standard Deviation	/	0.16	1.04	1.07	1.09

4.1.7 PVT Data

The measured values for the material PVT data and the approximation with the two-domain Tait model can be seen in Figure 56. In general, the 2-domain-Tait-model and the 13-coefficient-model by Schmidt are mostly used to describe the PVT behaviour of thermoplastic materials. As a semi-crystalline polymer, the selected material (PA66 GF30) has both crystalline and amorphous phases in its solid state (two transition temperatures, T_m and T_g). In our case, a good approximation of the PVT behaviour is not given nor by the Schmidt or the two-domain Tait model. Because of the approximation of the material PVT properties, we expected poor results when analysing shrinkage and warpage in the simulation software. The main error in our measurement is the distance interval between 0 and 1600 bar, as shown in Figure 96; this distance interval is quite large; thus, we expect poor warpage approximation.

A better approximation of the PVT behaviour of the selected composite material could be achieved using the Renner model. The first measured PVT values and PVT approximation using the Renner model can be seen in Figure 57. As we can see from the diagram, the Renner model better approximates our material's PVT behaviour. Unfortunately, at the moment, Moldex3D software cannot use the Renner model to describe the PVT material data. Thus, the two-domain Tait model was used to create the material card.

We made additional measurements to improve the approximation of the PVT behaviour. Firstly, we examined the effect of the sealing material on the measurement results. For the first PVT measurement, we used polytetrafluoroethylene (PFTE) seals. Also, we made an additional measurement using Vespel or polyimide (PI) seals which are more stable at higher temperatures, up to 300°C. Thus, we would reduce the influence of possible false measurements of the specific volume due to seal material softening. Figure 58 shows the comparison of the measured PVT behaviour using PTFE versus Vespel seals. As shown in the figure, the angle of the PVT curves decreased using Vespel seals, while the distance between isobars remained the same.

The difference in the specific volume was less in the solid range (approximately 1%). In the melt range, the difference is more significant (around 5%).

We performed another measurement using PFTE seals with decreasing pressure steps. Using a different measurement approach could improve the measurement results since, from Figure 56, we can see that with the decrease of pressure, the distance between isobars increases, thus increasing the error. Figure 59 compares the PVT behaviour using PTFE seals with decreasing and increasing pressure steps. As we can see, the difference between isobars significantly decreased, especially at lower pressures, and the angle of the curves remained similar. In conclusion, we expected better warpage approximation than with previous measurement results. Since the distance between isobars is still high compared to other material cards, we still expected overly high warpage values from the IM simulation.

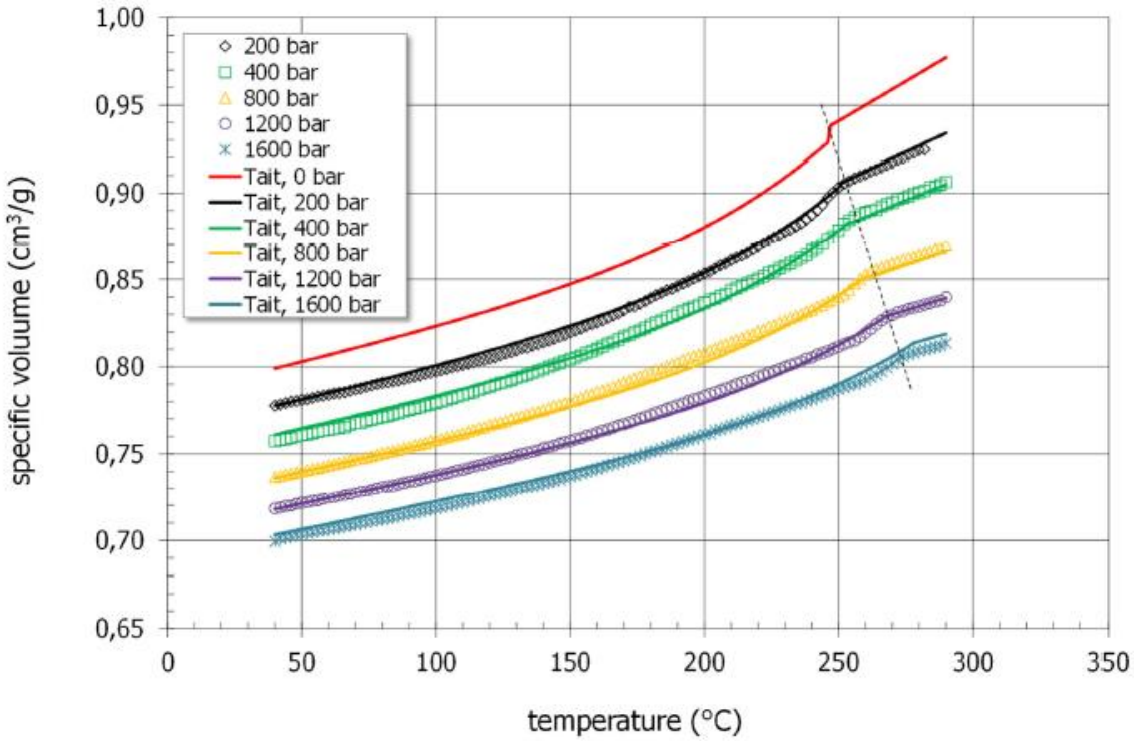

Figure 56: PVT Diagram Using the Two-Domain Tait Model for Data Approximation (lines represent approximated data, symbols represent measured values)

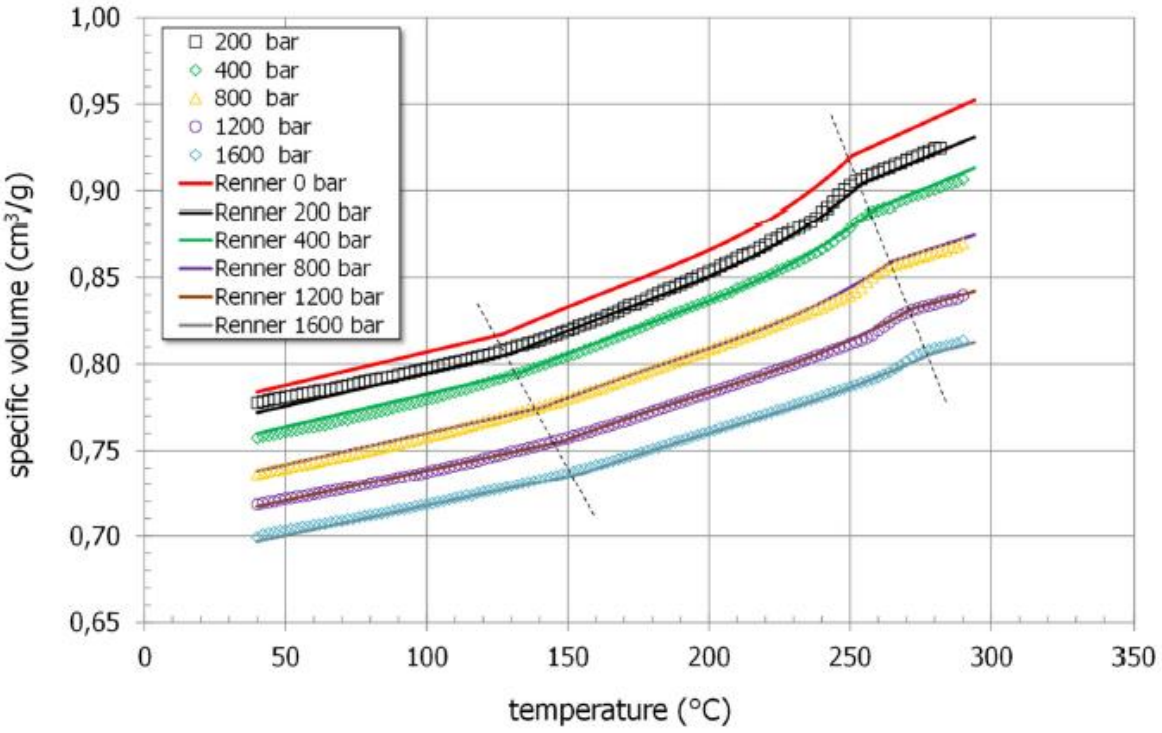

Figure 57: PVT Diagram Using the Renner Model for Data Approximation (lines represent approximated data, symbols represent measured values)

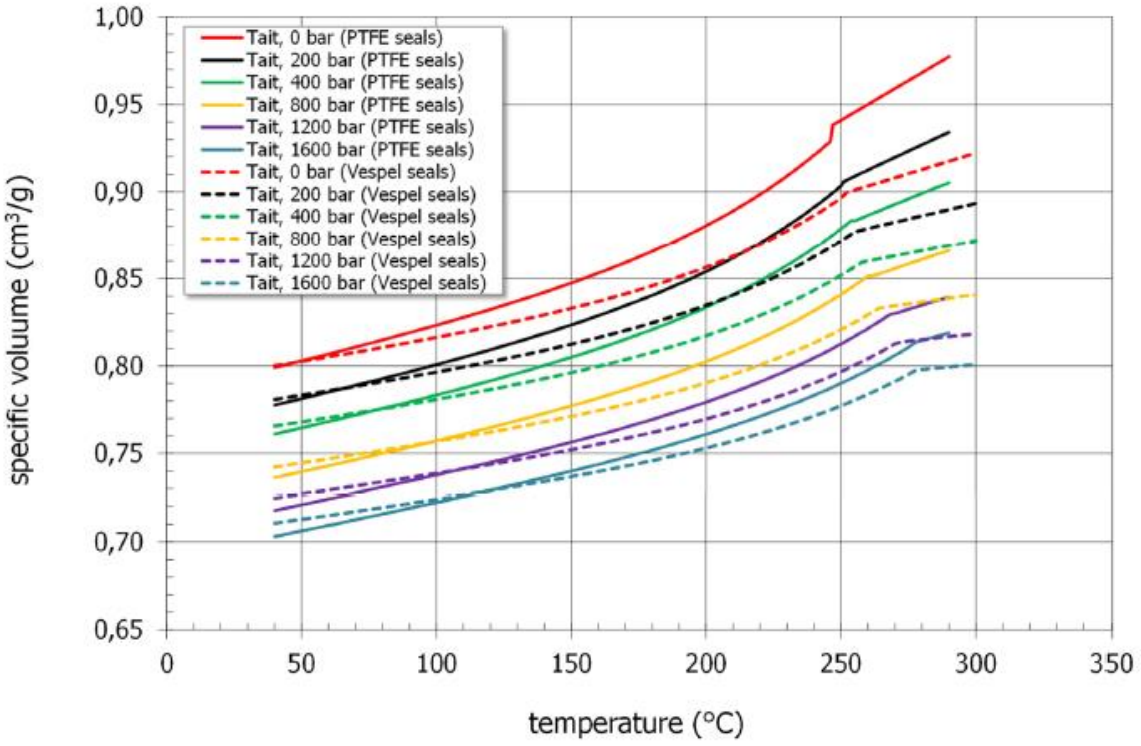

Figure 58: Comparison of the PVT Behaviour Measured with PFTE (solid line) and Vespel Seals (dotted line)

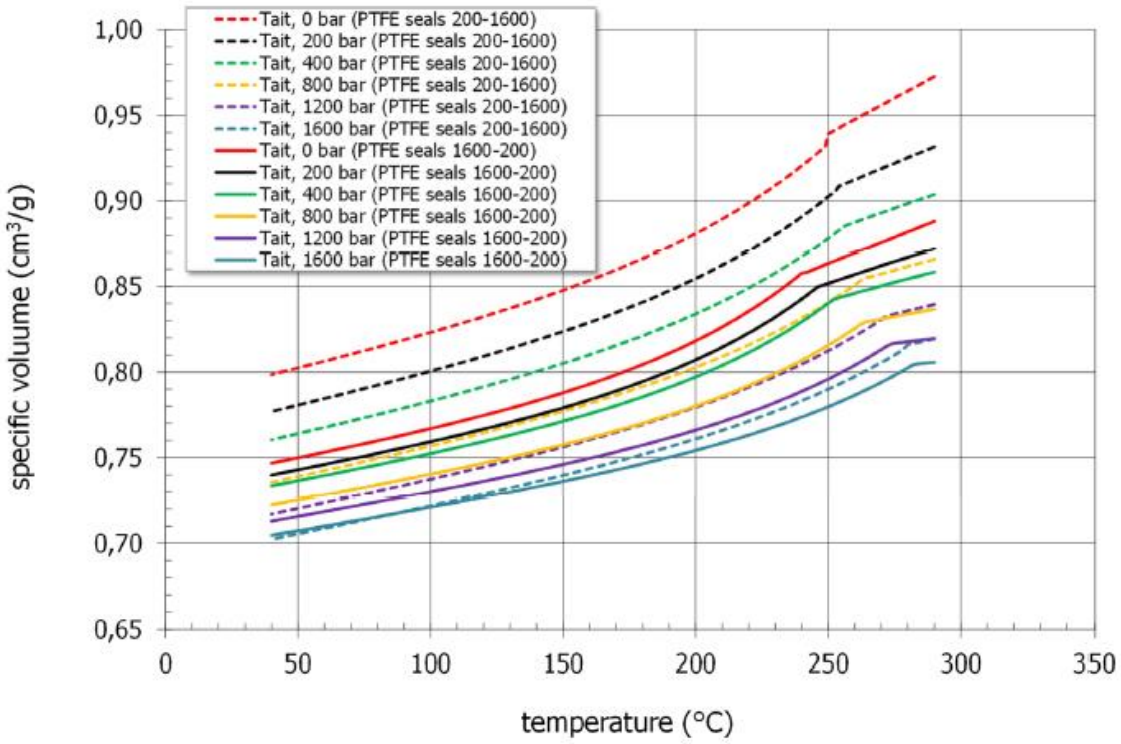

Figure 59: Comparison of the PVT Behaviour Measured Using the PTFE Seals with Decreasing (solid line) and Increasing Pressure Steps (dotted line)

4.1.8 Thermal Conductivity

The results of the thermal conductivity, measured according to the standards ASTM D5930-09 and ASTM D7984, can be seen in Figure 60. The exact numerical values of the mean arithmetic value calculated from the three independent samples are summarized in Table 26. The coefficient of variation amounts to ±1.84%.

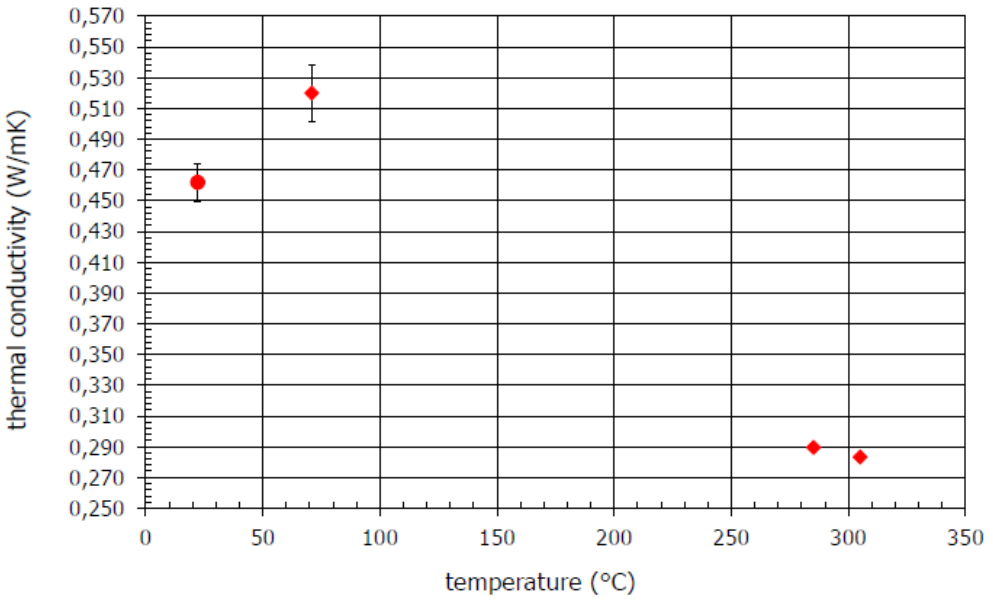

Figure 60: Thermal Conductivity as a Function of Temperature

Table 26: Thermal Conductivity Results

Standard	T [°C]	λ [W/m*K]	Standard Deviation [± W/m*K]	Coefficient of Variation [± %]
ASTM D7984	22.25	0.462	0.01251	2.71
	70.89	0.520	0.01846	3.55
ASTM D5930-09	285.12	0.290	0.00193	0.67
	304.97	0.283	0.00118	0.42

4.2 Comparison of Own-Measured Material Data With Moldex3D Material

The comparison of our measured material card data with alternative material cards can be seen in Appendix 5. Viscosity data comparison shows a slightly different material behaviour, especially at the lower shear rate values. The two alternate material cards could use only HPCR data for their calculation. In general, our measured data looks acceptable.

The PVT diagram indicates that our data show a higher specific volume difference between maximal and minimal pressure. A high difference in the specific volume between maximal and minimal pressure will lead to higher warpage values; thus, we expect a poor estimation of warpage. Using the Renner model would improve the warpage approximation, but generally, we expect a poor warpage prediction from the original material card.

The specific heat data is similar to the two alternative material cards. As we can see, the T_m of the alternative cards was approximately 230°C, whereas our material card showed T_m at 260°C. Different T_m could be due to a different material composition; we compared our measured T_m peak, which corresponds with the supplier's T_m in TDS.

The thermal conductivity showed quite different behaviour at lower temperatures than the other two alternative materials. When comparing another PA66 GF30 material type, each showed slightly different behaviour or had linear data; thus, this is not a concern.

When comparing the relative crystallinity data, we found that the two alternative materials, like many others, use reference data for relative crystallinity. Figure 85 shows that the differences are minimal; thus, this should not significantly affect the results.

4.3 Comparison of Simulation Results for Filling and Packing Pressure With Actual IM Process

We compared the IM pressure from the simulation with the actual IM process. Initially, we compared the approximated filling-sprue pressure curves of several variations of our created material card, shown in Figure 61. The highest filling pressure value (≈600 bar) was measured using PVT data from two alternate materials (Ultramid A3WG6 and

Ultramid A218W V30). The simulated maximum filling pressure is significantly smaller than the actual maximal filling pressure of the IM machine (≈1000 bar). Also, the simulation runs with alternate material PVT data showed a shorter filling time than the actual part, which is ≈1 s. This mismatch in filling times suggests that a comprehensive characterisation of the material behaviour is needed to produce a good quality material card. A comprehensive characterisation of the material is required because the IM simulation also considers the correlation of material properties. Additionally, our created material card did not include the pressure dependence in the viscosity model (D3 coefficient). Thus, in the IM simulation, we did not consider the dependence of the shear viscosity on the pressure.

Our created material card and its variants showed maximum filling pressure of around 500 to 600 bar, which is not a good approximation of the actual filling pressure. As shown in Figure 61, the variants using decreasing pressure steps (PVT1) showed higher values, especially the linear specific heat variant. However, this is not a good comparison with the actual filling pressure behaviour.

Several factors could cause non-matching injection pressure; first, we compared the filling pressure of two simulation runs, one with symmetry boundary conditions and the other using an existing runner system and four housing parts. Thus, we could see if the boundary condition is the cause of false filling pressure approximation or if other factors contribute. Figure 62 shows the comparison of symmetry boundary condition vs entire part geometry. The filling pressure result using the symmetry boundary condition shows a slightly higher angle at the start of the fill, but in general, the differences are minimal; thus, using the symmetry boundary condition should not significantly affect our results.

In the next step, we compared the filling and packing pressure of several PA66 GF30 material cards with the actual filling pressure from the IM machine. The filling pressure comparison is shown in Figure 63. The IM machine pressure shows the actual injection pressure based on the sensor on the mould. In contrast, the simulated runs show only sprue pressure and not the complete injection pressure of the cylinder during the IM process. The IM machine used to produce the parts (Sumitomo Demag IntElect 2) is an electrical IM machine that measures the injection pressure via the measuring cell between the screw and the electric motor. This measurement method is not as accurate as the measurement of the injection pressure directly on the melt surface using piezoelectric sensors; thus, we expected some difference in the pressure curves.

From the filling pressure curves of different PA66 GF30 material cards, shown in Figure 63, we can see that the filling pressure highly depends on the material card data. A more in-depth study of the impact of material properties on the IM simulation is presented in the DOE. The two variants of our created material card, Ultramid A3WG6 material cards from Moldex3D and Moldflow, showed smaller filling pressure than the actual IM machine. The simulated run using Grilon AGZ-30/2 showed much higher

filling pressure than the IM machine. The material card for Grilon AGZ-30/2 was the only one with a pressure dependence in the viscosity model.

Nevertheless, we do not know how the D3 parameter was determined and if the producer of the material card verified the material card in the SIM simulation software. We obtained the best results using the Ultramid A218W V30 material card. In general, the steepness of the filling pressure curve from the IM machine is much higher than the filling pressure curve in the IM simulation. The difference in steepness of the filling pressure curve could be the due to the actual runner and cavity geometry differing from the CAD model. The process parameters were kept the same for all simulated runs, so this should not cause a pressure difference. As we can see from the injection moulding pressure curves, the alternative material cards do not necessarily give a good approximation of the actual material behaviour during IM.

As we can see from Figure 63, the material card is the leading cause of the deviation in the injection pressure. A comparison between the properties of Grilon AGZ-30/2, Ultramid A218W V30, and our created material card is shown in Appendix 5. From the figures, we can observe some differences between each material card's properties. The main difference is shown in PVT data. We examined several methods and causes for the high difference between isobars in PVT measurement. Unfortunately, none produced satisfactory results. From the PVT data shown in Figure 58 and Figure 59, we can see that the results depend highly on the measuring procedure and sealing material.

A good example is shown in Figure 100 (Appendix 5), where we compared the PVT data of Ultramid A3WG6 from Moldex3D and Moldflow. In our research, we compared the simulated results using Ultramid A3WG6 PVT data from Moldex3D and Moldflow. The filling pressure comparison showed a minimal difference between each material card, shown in Figure 63; the two curves overlap.

The next step of our research would be to carry out the PVT measurements according to a company's protocol that provides material cards such as Moldex3D and Moldflow. These companies have much experience producing material cards, have well-defined procedures for measuring different polymer materials, and check that the created material card matches the actual behaviour during the injection moulding process. Also, they have a direct insight into the mathematical equations their software uses for calculation.

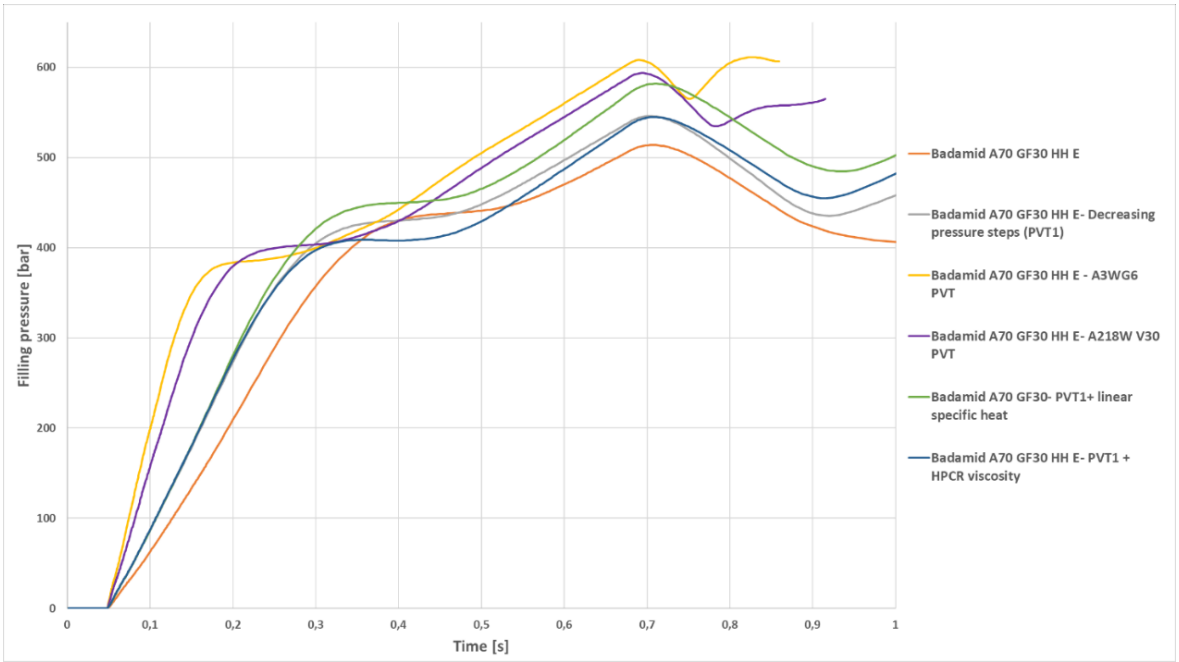

Figure 61: Sprue-Filling Pressure Comparison of Different Variations of Our Created Material Card

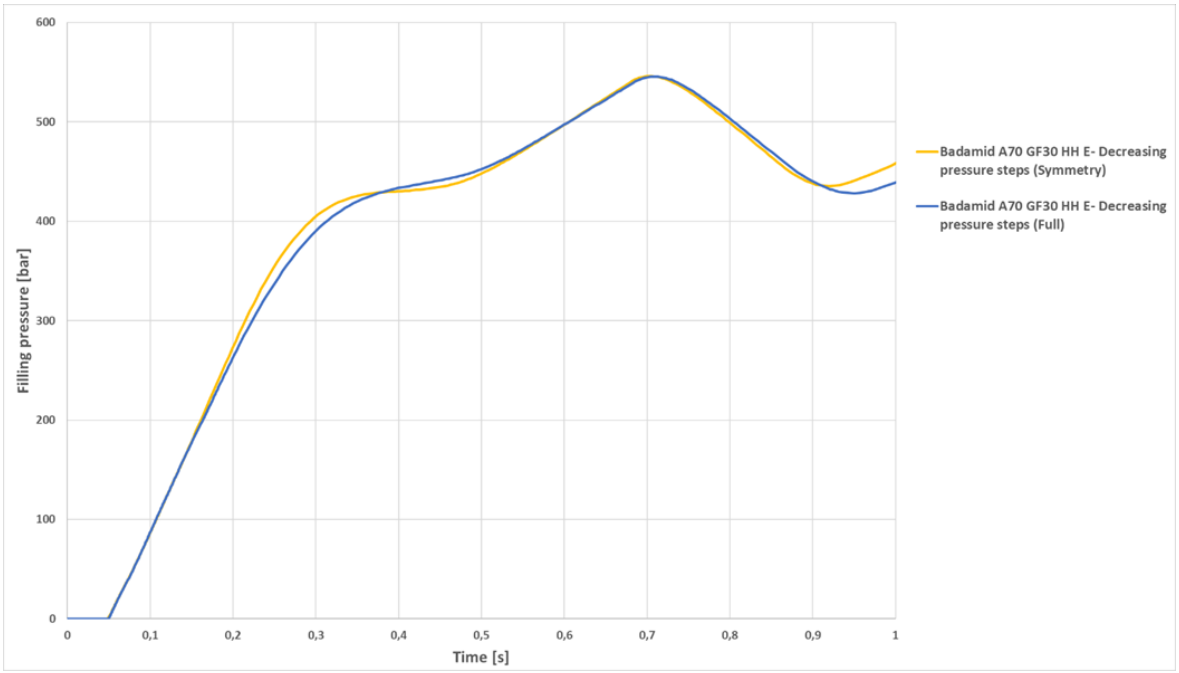

Figure 62: Symmetry vs Full Part Simulation of Badamid A70 GF30 HH E With Decreasing Pressure Steps PVT Data

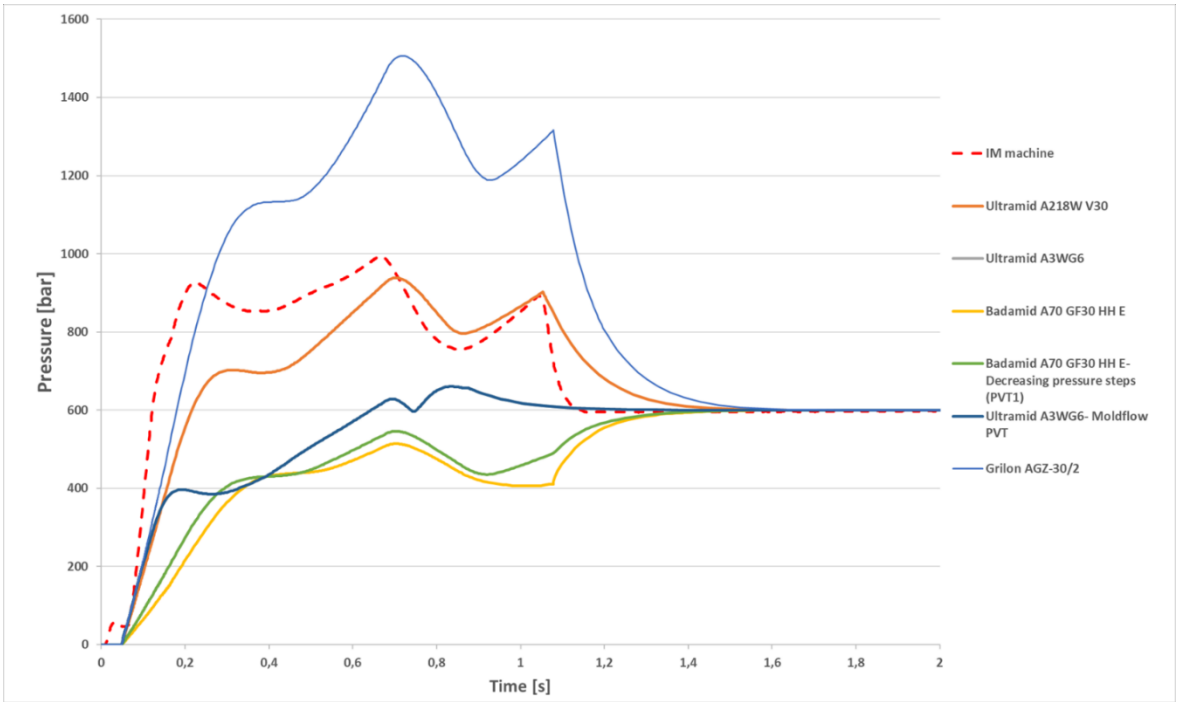

Figure 63: Comparison of the Filling Pressure of PA66 GF30 From Different Suppliers

4.4 Comparison of Simulation Filling Results With Actual IM Process

We compared the filling pattern of the two parts from the Moldex3D simulation and the actual IM process. We took the IM parts at different ram positions to show whether the simulation filling pattern matched the part's filling. The results of the filling pattern comparison are shown in Figure 64. We can see from the results that the tool's filling system is not balanced. The two housing parts are filled at different times due to different volumes and geometry. Figure 63 shows three pressure peaks on the IM PA66 GF30 material (dotted red line).

When designing the IM tool, one must consider the advantages and disadvantages of using two different parts on the same mould. Having just one mould will reduce the costs of the prototype parts. However, by using an unbalanced filling system, we may experience some unbalance due to the difference in material flow compared to filling each part separately. The two cavities' cycle times and mould wear also vary due to the uneven pressure distribution. In our case, the examined tool was designed only for the prototype phase.

The filling pattern of both housing parts is quite comparable. At the ram position of 50 mm and 40 mm for the upper part, we can see that the simulation shows a much more ideal flow of the material than the actual flow at that time. A similar difference can be seen when comparing the filling pattern of the lower housing at 45 mm and 60 mm. These differences are minimal and could result from differences in the actual cavity dimensions and cavity surface temperature compared to the CAD model. Also, the

material flow is much harder to predict when we have a four-cavity tool with two different housing parts. In the IM simulation, the runner system, the cooling channels, and the cavity geometry are perfectly symmetric; thus, the flow is more uniform. Whereas in the actual mould, the material flow is never equal. Also, the difference in the geometry of the two cavities can contribute to the uneven filling of the part. For example, in some sections of the part, the material flow of the upper housing could be much higher than the lower housing. In the next section, the upper housing flow could slightly decrease as well as the lower housing if the difference in the thicknesses of the two parts is high.

In conclusion, we can see that the part-filling pattern from the simulation is comparable to the actual IM process. We expect some deviation due to differences in geometry, IM parameters, and symmetry between the cavities. Nevertheless, IM simulation can give us a good prediction of the part-filling pattern.

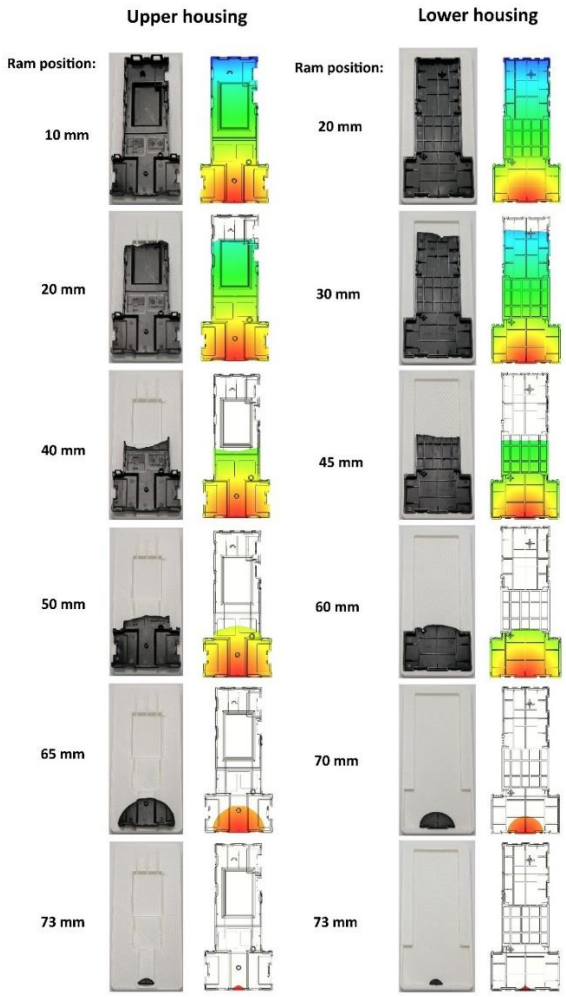

Figure 64: Filling Pattern Comparison of IM Upper Housing (left) and Lower Housing (right) With the Moldex3D Simulation

4.5 Comparison of Simulation Results With Actual IM Process and the Specified Part Dimensions

To compare the simulation results with the actual dimensions of two IM housings, we used the 3D dimensional analysis software PolyWorks (Innovmetric). We based our simulation on the scaled model used on the IM tool, and we compared the deformed 3D model from Moldex3E with the original CAD model according to the drawing. We aligned the deformed 3D model from Moldex3D using the datum reference ABC frame alignment for both housing parts. We expected some dimensions to be out of tolerance from the dimension analysis since the tool was designed for another PA66 GF30 material. By the time of writing our thesis, the tool was still in the prototype phase and was still undergoing some required corrections. Also, the drawing on which we based most of our measured dimensions might differ in future. Thus, some measurement features, datums, and tolerances might change when finalising the serial production tool and drawing. We did not include all the measured features from the drawing, as other more reasonable features could better describe the deformation of the part. We included some additional flatness measurements on the most problematic area of the part, which we could easily compare with the scanned part.

At first, we compared the warpage total displacement values of the simulated runs using different material cards and modifications, as shown in

Table 27. Warpage total displacement represents the maximum shape distortion of the part from its intended design. High total warpage displacement values may indicate a bad approximation of the part deformation. Our initial material card showed very high warpage values, so we made several tests to improve the measured PVT data. However, even with the PVT measurement made with decreasing pressure steps (mod PVT), the deformation was still too high compared to the measurement results from other PA66 GF30 material cards. We made several simulations using PVT data from two Ultramid material cards, using linear specific heat and only HPCR-measured data for the viscosity — none of the above produced satisfactory results; all results showed lower warpage total displacement values. Later, we made two additional measurements using our modified PVT and Ultramid A3WG6 PVT data with the reference relative crystallinity used by other PA66 GF30 material cards. All PA66 GF30 material cards mentioned in the master's thesis use reference relative crystallinity data described by the Nakamura model.

Table 27: IM Simulation Measured Warpage Total Displacement Values of Different Material Cards

Material Card	Warpage Total Displacement for Upper Housing [mm]	Warpage Total Displacement for Lower Housing [mm]
Ultramid A218W V30	0.724	0.688
Ultramid A3WG6 -Moldex PVT	0.677	0.649
Ultramid A3WG6 Moldflow PVT	0.677	0.649
Badamid A70 GF30 HH E	0.932	1.000
Badamid A70 GF30 HH E – mod PVT	0.773	0.831
Badamid A70 GF30 HH E – mod PVT and Ultramid A281W V30 Viscosity	0.845	0.841
Badamid A70 GF30 HH E - A3WG6 PVT	0.825	0.773
Badamid A70 GF30 HH E - A218W V30 PVT	0.939	0.940
Badamid A70 GF30 HH E - Modified PVT and Linear Specific Heat	0.582	0.506
Badamid A70 GF30 HH E - Modified PVT and HPCR Viscosity	0.790	0.830
Badamid A70 GF30 HH E - Modified PVT and Reference Rel. Crystallinity	0.526	0.520
Badamid A70 GF30 HH E - A3WG6 PVT and Reference Rel. Crystallinity	0.595	0.558

Next, we compared the measurement of the dimension of the two scanned parts and the deformed models from Moldex3D. Table 28 and Table 29 in Appendix 6 show the measured features of the two CT-scanned IM housing parts. Measured objects which are inside tolerance are coloured green, and measured objects which are outside tolerance are coloured red; all the measurement results are included in Appendix 7. The two IM parts are labelled A70 GF30 HH E cavity 1 and cavity 2, coloured orange and light blue. Different material cards were tested, along with our created material card with PVT made using decreasing pressure steps and PVT from Ultramid A3WG6. Also, we made additional simulations and measurements using the reference relative crystallinity data used by other PA66 GF30 material cards.

Figure 65 compares the results for the length and width of the upper housing. The results are generally quite similar. As we can see, our created material card with modified PVT and Ultramid A218W V30 shows a higher deviation compared to all other analysed material cards. Such a significant deviation from other measurements would indicate that the IM simulation for this material card gives a bad approximation of the material warpage and shrinkage. Bad warpage approximation could result from the high difference between isobars in the materials PVT data.

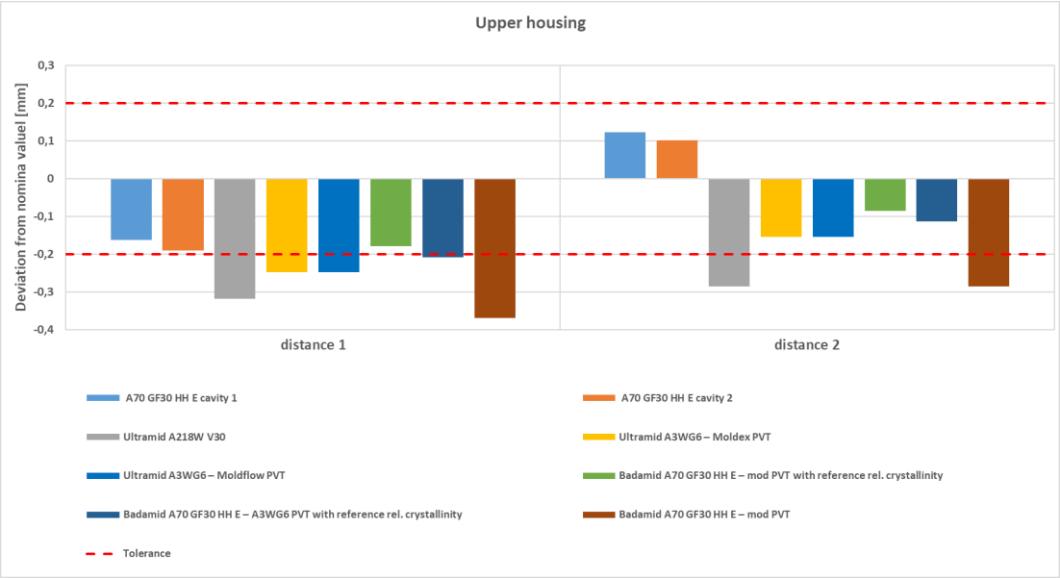

Figure 65: Upper Housing Distance 1 and 2 Results Comparison

Figure 66 compares all other distances made according to the drawing. Distances 3, 4, and 5, which describe the distance between the outer surfaces, are not comparable to the IM parts. Such a high difference between the measured distances could indicate that the IM simulation showed much smaller deformation of measured surfaces. The difference in shrinkage between the material cards is another potential factor. Also, the actual cavity dimensions cannot be precisely the same as the dimensions of the CAD model due to manufacturing accuracy. The comparison of distances 6, 7, and 8 also shows differences between the IM parts and the IM simulation results. Distance results for the Ultramid A3WG6 with PVT data from Moldex3D and Moldflow are identical.

Figure 66: Upper Housing Distances 3–8 Comparison

Figure 67 shows a comparison of the measured cone position according to datum A B C. We can see that the results are comparable between the different material cards.

Interestingly, the simulated results for the position of cone 1 underestimate the deviation, whereas there is an overestimation for the position of cone 2. We expected that because the simulation did not predict such high warpage of the datum plane A and all the connected datum features would show a higher difference between the IM part and the deformed model in the simulation. With the increase of the deformation of the datum plane A, all other features aligned to datums A, B and C would be affected. To reduce the measurement error due to alignment and the datum position, we also measured the flatness of the top surfaces. From our experience with the part and its assembly, we needed the top surface to be as flat as possible. The surface extraction parameters for the flatness comparison were set to include all surface points. Thus, we could directly compare the actual deformation of the part with the maximum approximated deformation from the IM simulated parts.

Figure 67: Upper Housing Cone Position A B C Comparison

Figure 68 shows the flatness result comparison. We can see that the measured flatness for most of the simulated material cards is quite similar. The IM simulation generally showed lower flatness values than the two IM parts. Our created material card with modified PVT data coloured brown showed the best comparison with the two IM housings out of all the simulated material cards. The results for the two Ultramid A3WG6 with PVT data from Moldex3D and Moldflow are identical. Two of our created material cards using the reference relative crystallinity data are comparable with the results of the Ultramid material cards. As we can see, our material card, coloured brown, which uses the measured relative crystallinity data, shows a better match with the two IM housings compared with our material card with references to relative crystallinity, which is coloured green. However, we recommend investigating each measured material property and improving the measurement results to approximate the material behaviour better. To some extent, we are limited by the available mathematical models in Moldex3D and the time and resources for such research.

Figure 68: Upper Housing Flatness Comparison

We compared the lower housing measurement results to confirm or refute our findings. Figure 69 shows the lower housing distance result comparison. The resulting trend is similar to the upper housing results shown in Figure 65. IM simulation results show lesser distance results compared to the IM part. Our primary focus is on the flatness measurement results, which better describe the part warpage.

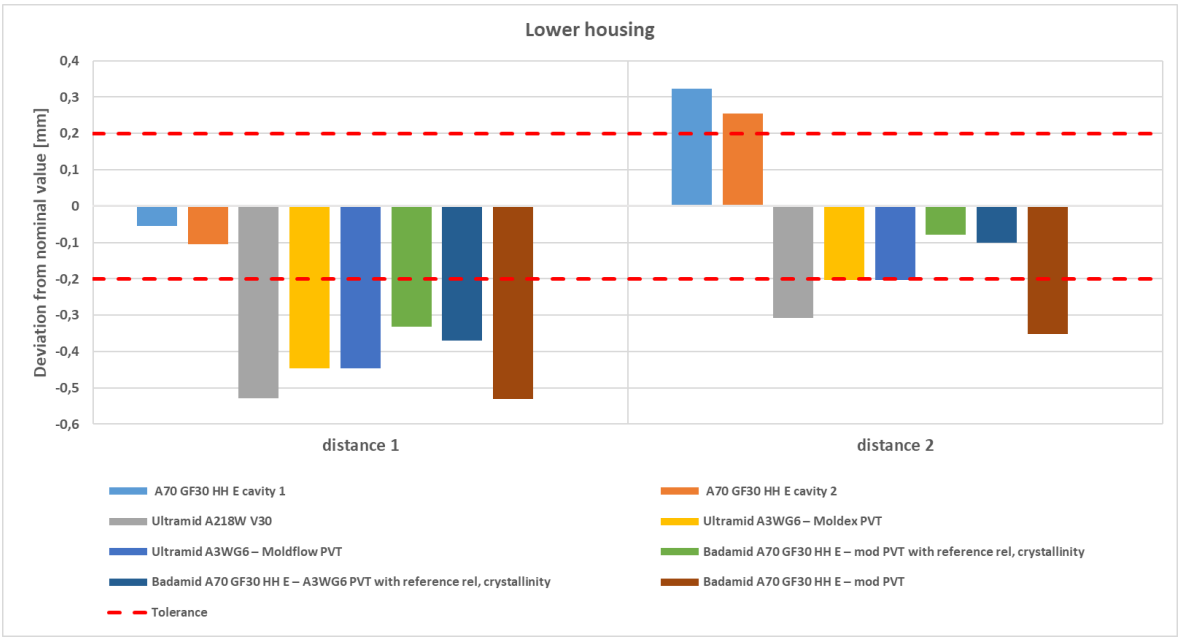

Figure 69: Lower Housing Distance Comparison

Figure 70 shows the cone position comparison. From the comparison of the position of cone 5, we can see that most of the material cards display a good comparison of the actual position of cone 6. The simulation results generally showed a much higher cone 5 position deviation than the actual IM part. The two material cards, coloured grey

and brown, compare best with the IM parts. We cannot consider all the process-effecting factors in the IM simulation, such as the environmental complexity, complex interactions between the material properties, hardware limitations, and limitations of the mathematical models available in the simulation; thus, we expected some deviation.

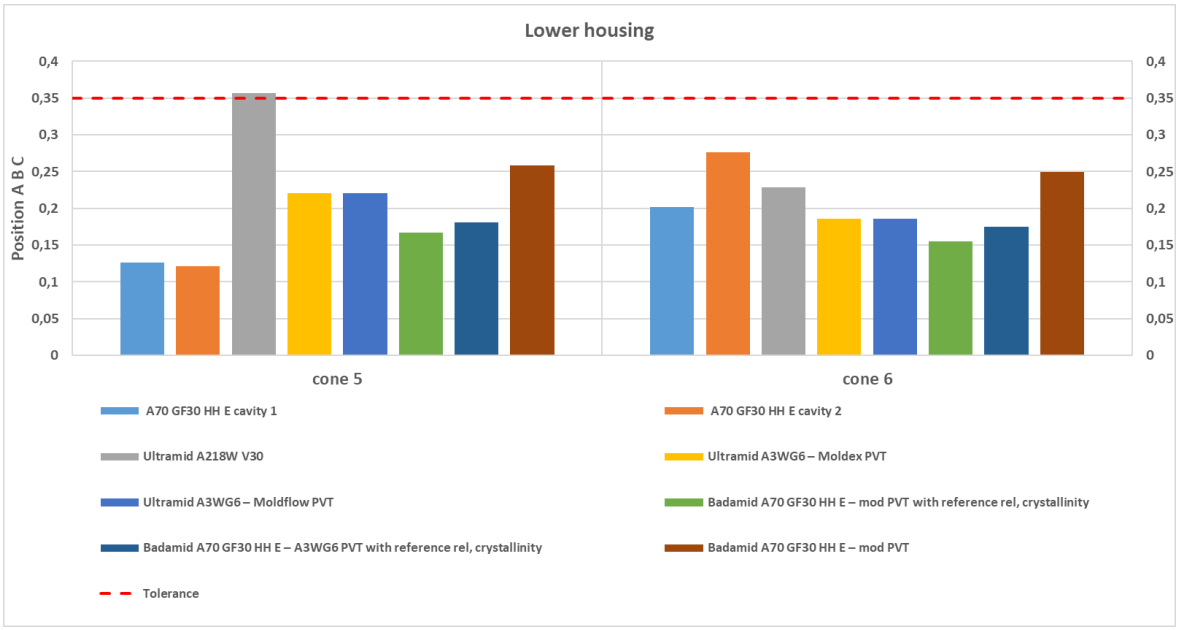

Figure 70: Lower Housing Cone Position Comparison

Figure 71 and Figure 72 show the comparison of the surface profile measurement results, i.e. that the material card coloured grey and brown provide the best comparison with the actual IM parts. We expected some deviation from the actual IM parts because multiple factors are not considered in the IM simulation. However, our created material card generally provided a solid approximation compared to other material cards. The Ultramid A3WG6 material cards with PVT data from Moldex3D and Moldflow are identical. Also, we can see the effect of relative crystallinity data on the warpage results by comparing the brown column representing our created material card and the green column representing our created material card with reference relative crystallinity data. Surface profile measurement results in Figure 72 show similar results. In general, the IM simulation calculated lesser deformation than the IM part. Best comparison of the alternate material cards was obtained using Ultramid A218W V30.

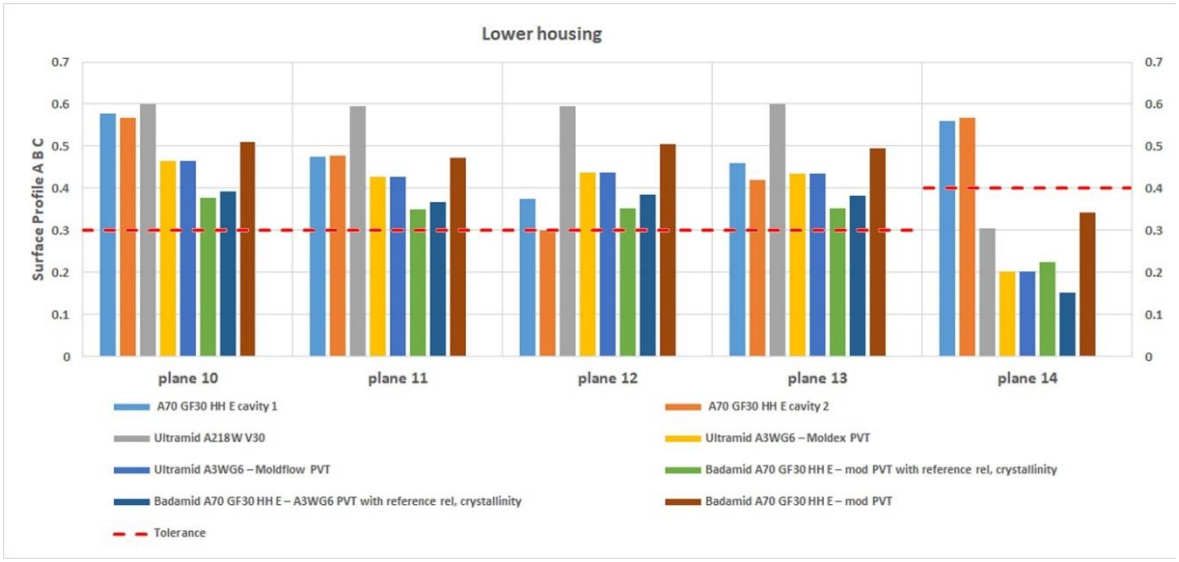

Figure 71: Lower Housing Surface Profile Comparison – Part 1

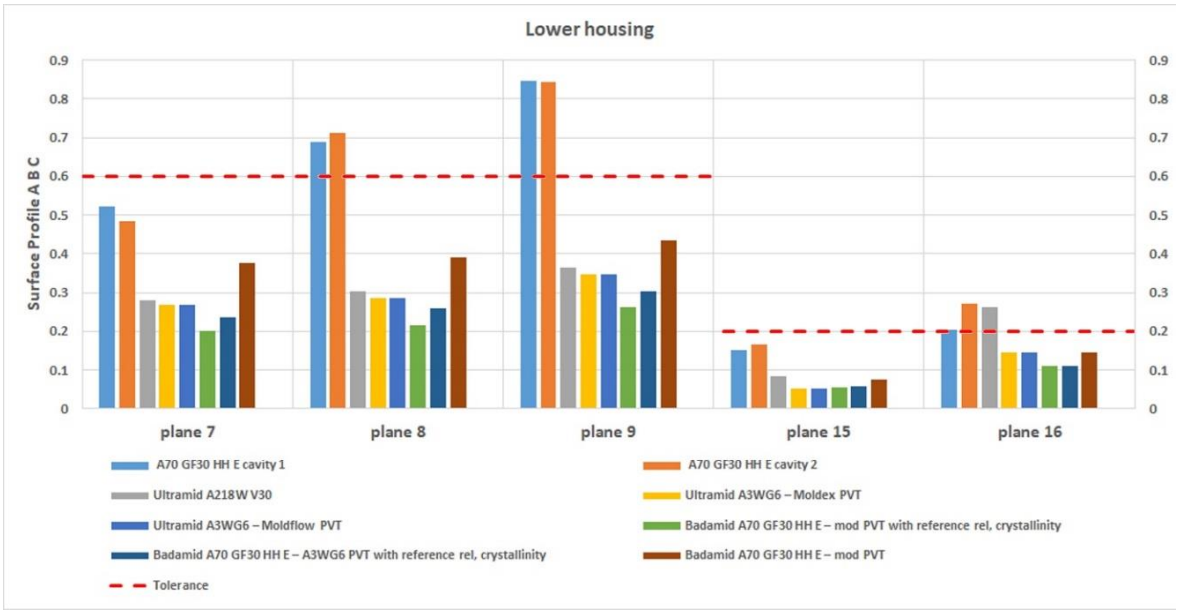

Figure 72: Lower Housing Surface Profile Comparison – Part 2

Lastly, we compared the flatness results of the top surface of the upper housing, shown in Figure 73. Interestingly, we can see that the Datum plane A, plane 25, and plane 26 flatness results are comparable to the IM parts. Our created material card, coloured brown, shows a slight overestimation of the flatness of datum plane A and plane 25. The simulation measured results for the flatness of plane 26 show a slight underestimation of the actual plane 26 flatness. The columns, coloured yellow, blue, and brown, are comparable with the IM parts. We also included a measurement of the whole top surface, where we set the extraction parameters to get the worst-case scenario results meaning extracting all the data points of the measured surface. As we can see, our created material showed a good match comparing the flatness of plane 32 of the two IM parts. Other material cards showed lower flatness but were similar. The green column shows much smaller flatness measurement, which would indicate

poor comparison of the actual deformation of the part. From all flatness results, we can say that the trend of the measured flatness is somewhat comparable. The IM part exhibits some deformation of the top plane due to two edges of the part deforming towards the outside of the part. This behaviour is shown by the flatness of plane 32 results of the two IM parts and our created material made using only our measured values, coloured brown. The two of our created material cards using the reference relative crystallinity values generally showed comparable results but did not give a good approximation of the deformation extremes of the actual part. The Ultramid material card showed a similar trend. They were generally comparable, but the comparison was not good regarding some highly deformed small surfaces or defects. The material card coloured dark grey showed a good approximation of the deformation extremes in most cases, but it was still not good compared to the two IM parts.

Figure 73: Lower Housing Flatness Comparison

We can conclude that no material card ideally approximates the deformation for both housing parts. Based on the results, specifying a material that would be most suitable for further IM simulation analysis using the Badamid A70 GF30 HH E material would be difficult. Ultramid A218W V30 showed a good match for the lower housing, while Ultramid A3WG6 had some suitable matches for the upper housing comparison. Results from our created material card Badamid A70 GF30 HH E with modified PVT did match the deformation trends and the extremes of the actual IM part. However, the created material card did not provide a perfect approximation. The differences between the two Ultramid A3WG6 material cards using Moldflow and Moldex PVT data were minimal; thus, we can conclude that PVT data should be of good quality.

For R&D purposes, we recommend using multiple materials and comparing the deformation trends. Also, our created material card could be improved by investing additional time and resources. There are several factors which we did not consider.

Regarding the PVT data, we did not consider the change in viscosity with cooling rate and time. The distance between the isobars remains relatively high. With additional measurements or a different measurement procedure, we could improve the accuracy of the measured results. Our viscosity data did not include the D3 parameter, which defines the pressure dependence of the viscosity. Testing the material card on some in-production phase parts which use the same PA66GF30 material would be meaningful. By comparing the IM simulation with the part in serial production, we could better understand the actual difference in the IM approximation because the deformation is much smaller. When comparing IM parts which exhibit high deformation, it is difficult to accurately measure and analyse part dimensions, as the deformation can introduce errors and distortions in the measuring process, leading to inaccurate dimensional analysis of the part.

4.6 Full Factorial Design of Experiment

Four factors were considered in the 24 full factorial designs, each with two levels. The DOE resulted in 16 unique combinations of the PVT, viscosity, thermal conductivity, and crystallization rate varied by the CV shown in Table 17. Our research aimed to examine the effect of each varied material property on the calculated filling pressure, total warpage displacement, and the dimensions of the two housing parts. To achieve this goal, we simulated all possible combinations of the two levels for each factor to comprehensively analyse the main effects and interactions between the variables.

Figure 74 shows the effect of each of the four material properties on the filling pressure at 0.3 and 0.7 seconds. We have measured the pressure at a stated time because this is the point where the pressure curves are at peak. As we can see from the figure, the viscosity variation showed the highest effect on the filling pressure. We expected high dependency of the filling pressure on the viscosity because with higher viscosity, the resistance of the material increases and vice versa. Also, the variation of the crystallization rate at two-time sections showed no change in the calculated filling pressure values. We expected a small effect of the crystallization rate on the filling pressure since crystallization occurs when the material cools down or changes the state of matter. The PVT and the thermal conductivity variation showed minimal effect on the filling pressure value. Generally, the highest filling pressure results were obtained at maximum thermal conductivity and viscosity. Comparing the PVT data curve at the two-time steps, we noticed a reverse response at the two measured time sections. Overall, the effect of the PVT data on the filling pressure at the selected time sections was minimal.

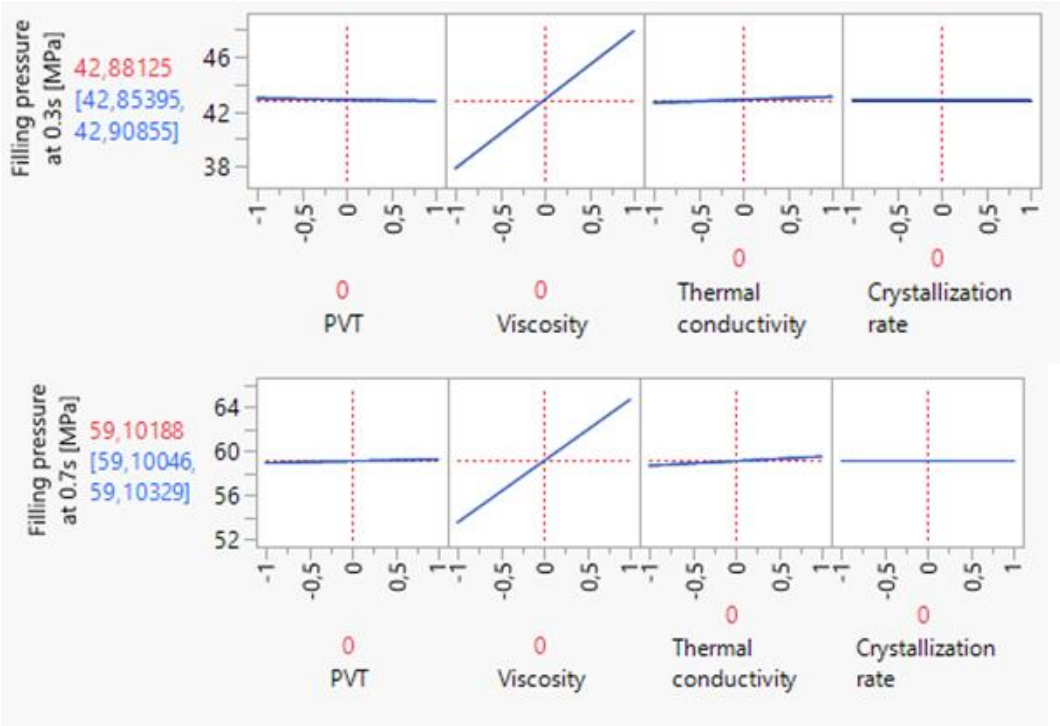

Figure 74: Effect of the Four Material Properties on the Filling Pressure

Next, we compared the effect of the four material properties on the total warpage displacement values of the two-housing parts, shown in Figure 75. The predicted behaviour of the two housing parts is identical. We can confirm that the input data is okay since the behaviour of the two housing parts should be the same. Using the full factorial design with two levels, we get a linear response between the measured data points. The actual behaviour is not linear, but for our DOE, this was sufficient. As we can see from the figure, the crystallization rate and the PVT data significantly impact the approximated warpage total displacement. With the increase of the crystallization rate, the molten material in the cavity solidifies quickly, which results in a high degree of crystallinity and higher shrinkage. Also, with a high crystallization rate, the molten material has less time to orient. Thus, the molecular structure orientation becomes more random, decreasing the warpage. The effect of the thermal conductivity and viscosity was comparable. We obtained the highest approximated total warpage displacement at minimal viscosity, PVT, thermal conductivity, and crystallization rate values. With the decreased thermal conductivity, the material retains heat for longer, compared to a higher thermal conductivity value. With lower heat transfer, the crystallization rate decreases and causes the relaxation of internal stress and higher molecular orientation, which can result in higher warpage.

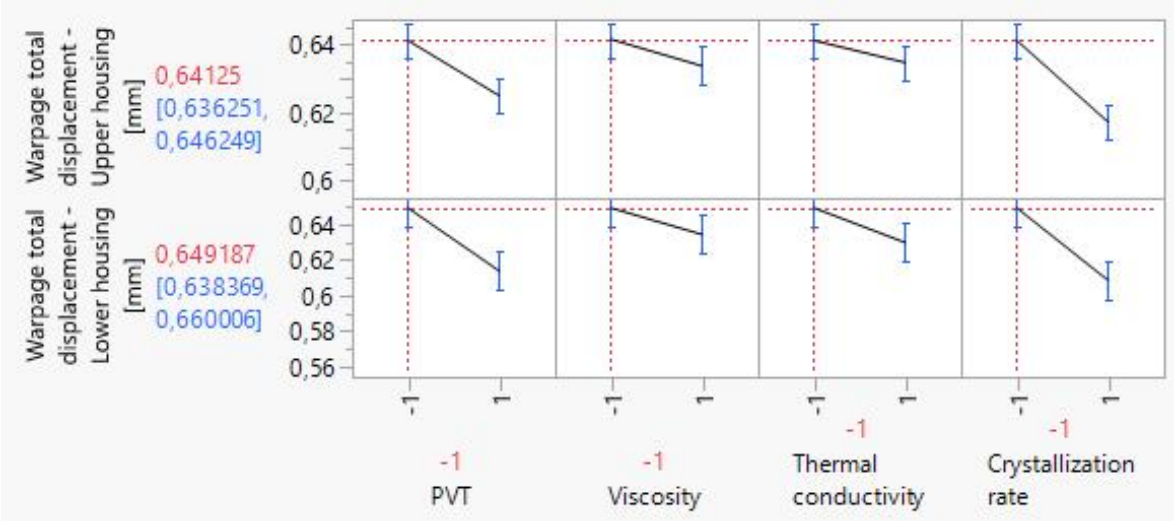

Figure 75: Effect of the Four Material Properties on the Warpage Total Displacement Value for Both Housing Parts

Figure 76 and Figure 77 show the effect of the four varied material properties on the flatness of the top surface of the lower and upper housing. Comparing the two figures, we see a similar trend in the results. The crystallization rate and the PVT had the most significant effect on the flatness of the two measured surfaces. With the increase in the crystallization rate, the molten material solidifies much faster, resulting in a higher degree of crystallinity. The polymer chains have less time to orient at higher crystallization rates, resulting in a more uniform surface shrinkage. The increase in PVT data also significantly affected the measured flatness value. The thermal conductivity and viscosity effects are smaller than the PVT data and crystallization rate. With higher thermal conductivity, the polymer assimilates heat much faster, which results in faster cooling and crystallization rate and, consequently, lower measured flatness values. Also, we varied the viscosity data for a much higher CV value than the thermal conductivity. We can conclude that the viscosity did not significantly affect the measured flatness results out of the four material properties in our case.

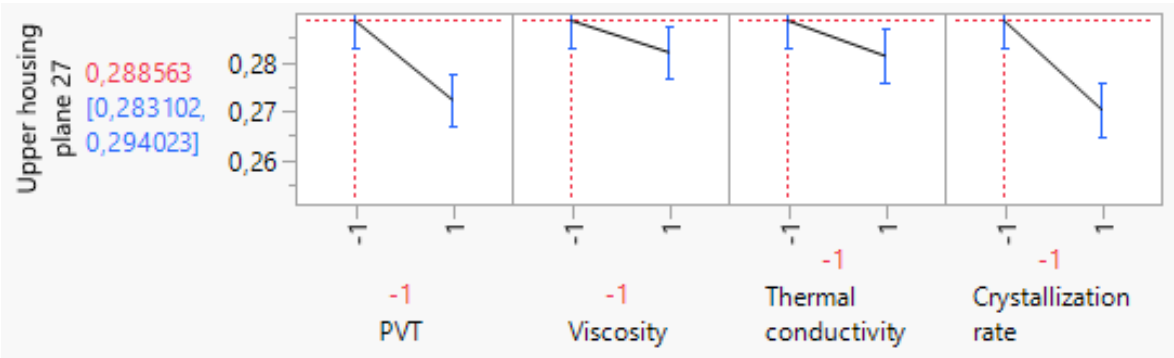

Figure 76: Effect of the Four Material Properties on the Upper Housing Plane 27 Flatness

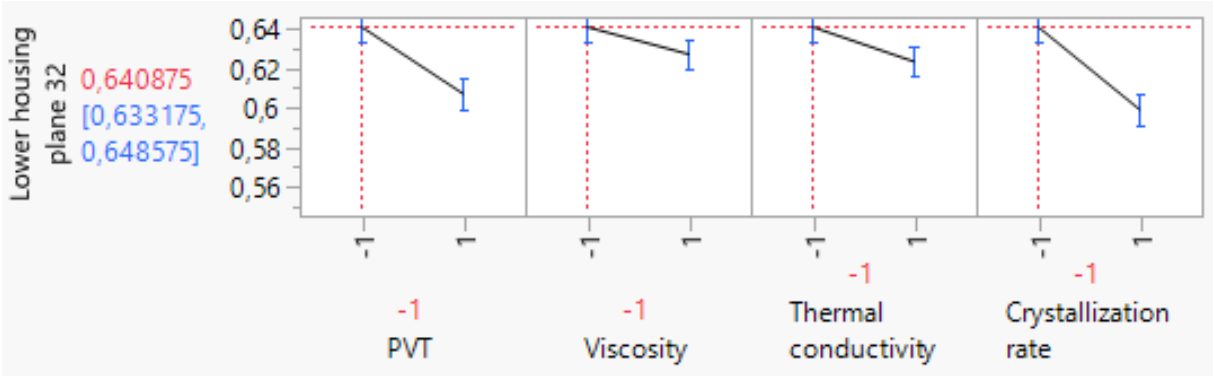

Figure 77: Effect of the Four Material Properties on the Lower Housing Plane 32 Flatness

In conclusion, the viscosity data significantly affects the approximated filling pressure. The crystallization rate does not affect this stage of the IM process, whereas the thermal conductivity and PVT showed minimal effect on the measurement results. The analysis of the estimated warpage total displacement factors and flatness of the top plane for both housings showed similar trends. Based on our high variation of the viscosity data, we conclude that viscosity does not significantly affect these measurement results compared to the other three material properties. Thermal conductivity with increased values showed lower estimated warpage and flatness, but the impact was less significant than those of the PVT data and crystallization rate. We observed lower flatness and total warpage values with the increased PVT data.

With our DOE, we found that the crystallization rate and the PVT data significantly impact the flatness and total warpage approximation. A higher crystallization rate leads to a less oriented polymer structure due to faster cooling and higher crystallization, reducing warpage. The results from our DOE help us understand the correlation between the four factors and their effects on the filling pressure, total warpage estimation, and flatness. This information will be useful for further optimisations of the material card data and for understanding the influence of the material properties on each result. The results obtained are another indicator that a comprehensive material characterisation and a good understanding of the behaviour of polymeric materials are required to produce a satisfactory quality material card. Also, producing the material card is time and resource-consuming, as much testing is required to verify the material card thoroughly.

5 CONCLUSION

In the first part of the master's thesis, we analysed the variation of the composition of several PA66 GF30 batches. We compared the influence of different batches on the mechanical and thermal properties. In the second part of the master's thesis, we characterised the material Badamid A70 GF30 HH E and produced a material card in Moldex3D simulation software. The quality of the material card was checked by comparing the filling pattern, the pressure curves, and the dimensions of the deformed model with the actual IM process and two housing parts. Additionally, we conducted a DOE to show the effect of the material properties from the material card on the filling pressure, total warpage displacement, and flatness of the top surface of the part.

In this section, we briefly summarise the key findings of our research, focusing on the thermal and mechanical analysis of different PA66 GF30 batches and the creation and verification of our created material card. The following findings highlight the significant outcomes of our study:

Analysis of the thermal and mechanical properties of different batches: We observed some variation in the material composition by examining the material batches. In particular, the composition of glass fibres and polymeric material exhibited a variation of approximately ± 0.5%. The thermal and mechanical testing showed some deviation between the measured batches but were generally very small.

Creation and verification of the material card: To examine and understand the effect of the material card on the IM simulation results, we created a material card. We made the material card based on the material producer's TDS and the measured PVT, viscosity, thermal conductivity, specific heat, and relative crystallinity data. We designed the IM to match the actual IM condition and parameters as closely as possible. Nevertheless, we have observed deviations in the simulation results from the actual IM part. Most notably, the estimated filling pressure curves showed significantly smaller values than the IM machine. The alternate material Ultramid A218W V30 showed the best comparison to the actual filling pressure curve.

The dimensional comparison showed some deviation from the IM part. We compared several alternative material cards and made some variations of our data, but none represented a perfect comparison. The Ultramid A218W V30 and Ultramid A3WG6 showed an acceptable comparison. Unfortunately, they did not provide a satisfactory comparison of the flatness of the top surface of the two analysed parts, which represents an important feature. Our created material card showed comparable results but did not provide a perfect approximation of all the measured features of the IM parts.

With the IM filling pattern analysis, we found that the simulated part filling matches the actual part produced through injection moulding. This result shows that our material card is reliable in predicting the tool's flow behaviour and material distribution.

With the DOE, we have shown that viscosity data is crucial for approximating the filling pressure. Regarding the part warpage analysis, the crystallization kinetics and the PVT data are essential in approximating material behaviour.

In future work, some material properties could be re-characterised in collaboration with the Moldex3D laboratory. With their help and knowledge, we could better understand, prevent and optimise the material card. Using newer mathematical models, which include more influencing parameters on the material behaviour, would improve the quality of our material card. For example, the PVT data represents the material behaviour at one constant instead of a variable cooling rate. Also, our viscosity data did not include the pressure dependence parameter (D3). Due to the complexity and time required to produce a quality material card, we recommend that companies seek the service of the IM simulation companies that specialise in this field. Because these companies understand the background behind the simulation software, they have a lot of experience with material card creation and can provide a good analysis of the measured data.

With our research, we have analysed the accuracy of the IM simulation, the effect of material data in the software library on the results and the mechanical, and thermal properties variation between different batches. None of the examined material cards perfectly approximated the actual material behaviour. No material card will flawlessly define the material's behaviour during the IM process, as many assumptions and simplifications are required in the simulation to ease the complexity of the calculation. IM simulations use data from several material properties in correlation with each other; because of this correlation, there will always be some difference when using alternate materials cards due to different compositions. We also have no insight into the actual mathematics the simulation software uses, as it operates with complex algorithms and computational methods. However, through numerous validation and verification processes, we can confirm the reliability of the IM simulation. We have insight into the mathematical model and the values of their parameters used by the simulation. This information is crucial as it tells engineers which parameters are accounted for in the mathematical model and which are excluded. The field of IM simulation is continuously evolving, and so are the mathematical models.

Simulation software is a must-have for companies involved in plastic processing. Although no simulation is 100% reliable, we can use simulation software to see the deformation trends and potential problems in the development phase of a product. In conclusion, we must never unthinkingly trust the simulation and its results but approach it critically.

REFERENCES

[1] S. Sharma, An Introduction to Molecular Dynamics Simulation of Polymer Composites, first ed., Nova Science Publishers, New York, 2020. https://doi.org/10.52305/LWUR4972.

[2] M.N. Subramanian, Polymer Materials and their Processing, in: Basics of Polymers: Fabrication and Processing Technology, first ed., Momentum Press Engineering, New York, 2015: pp. 21–49.

[3] R.J. Young, P.A. Lovell, Introduction to Polymers, third ed., CRC Press, Boca Raton, 2011.

[4] H. Pivšek, Umetnost brizganja, 2. izdaja, PROFIDTP, Ljubljana, 2018.

[5] V. Goodship, Practical Guide to Injection Moulding, second ed., Smithers Rapra, Shrewsbury, 2017. https://akugue.com/pdf/practical-guide-to-injection-moulding-pdf-pdf-4739704 (accessed February 14, 2023).

[6] J.E. Mark, Physical Properties of Polymer Handbook, second ed., Springer Science+Business Media, New York, 2006.

[7] T.P. Sathishkumar, S. Satheeshkumar, J. Naveen, Glass fiber-reinforced polymer composites - A review, Journal of Reinforced Plastics and Composites. 33 (2014) 1258–1265. https://doi.org/10.1177/0731684414530790.

[8] C.D. Han, Injection Molding, in: Rheology and Processing of Polymeric Materials: Volume 2: Polymer Processing, first ed., Oxford University Press, Oxford, 2006: pp. 351–376. https://doi.org/10.1093/OSO/9780195187830.001.0001.

[9] T. Ageyeva, S. Horváth, J.G. Kovács, In-Mold Sensors for Injection Moulding: On the Way to Industry 4.0, Sensors. 19 (2019) 1–21. https://doi.org/10.3390/s19163551.

[10] P. Kennedy, R. Zheng, Flow Analysis of Injection Molds, second ed., Hanser Publication, Cincinnati, 2013. https://doi.org/10.3139/9781569905227.fm.

[11] A. Gnatowski, A. Kijo-kleczkowska, J. Krzywanski, P. Lemanski, E. Kopciuszewska, Computer Simulations of Injection Process of Elements Used in Electromechanical Devices, Materials. 15 (2022) 1–6. https://doi.org/10.3390/ma15072511.

[12] M.-L. Wang, R.-Y. Chang, C.-H. (David) Hsu, Molding Simulation: Theory and Practice, first ed., Hanser Publications, Cincinnati, 2018. https://doi.org/10.3139/9781569906200.FM.

[13] C.D. Han, Relationships Between Polymer Rheology and Polymer Processing, in: Rheology and Processing of Polymeric Materials: Volume 1: Polymer Rheology, first ed., Oxford University Press, Oxford, 2007: pp. 3–11. https://doi.org/10.1093/OSO/9780195187823.001.0001.

[14] J.D. Menczel, R.B. Prime, Thermal Analysis of Polymers: Fundamentals and Applications, first ed., John Wiley and Sons, New Jersey, 2008. https://doi.org/10.1002/9780470423837.

[15] I.M. Ward, J. Sweeney, W. Sweeney, Yielding and Instability in Polymers, in: Mechanical Properties of Solid Polymers Third Edition, third ed., John Wiley & Sons, Chichester, 2013.

[16] M.N. Subramanian, Thermal Analysis, in: Basics of Polymers, Volume II: Instrumental Methods of Testing, first ed., Momentum Press, New York, 2019: pp. 107–117. https://web-s-ebscohost-com.nukweb.nuk.uni-lj.si/ehost/ebookviewer/ebook/ZTAwMHh3d19fMjAyNzkzM19fQU41?sid=612b056a-1185-4522-8c90-98defee740d8@redis&vid=7&format=EB&rid=4 (accessed March 27, 2023).

[17] N.M. Nurazzi, M.R.M. Asyraf, M. Rayung, M.N.F. Norrrahim, S.S. Shazleen, M.S.A. Rani, A.R. Shafi, H.A. Aisyah, M.H.M. Radzi, F.A. Sabaruddin, R.A. Ilyas, E.S. Zainudin, K. Abdan, Thermogravimetric analysis properties of cellulosic natural fiber polymer composites: A review on influence of chemical treatments, Polymers (Basel). 13 (2021) 1–9. https://doi.org/10.3390/polym13162710.

[18] M.R.M. Asyraf, N.M. Nurazzi, M.N.F. Norrrahim, K.Z. Hazrati, A. Ghani, F.A. Sabaruddin, S.H. Lee, S.S. Shazleen, M.R. Razman, Thermal properties of oil palm lignocellulosic fibre reinforced polymer composites: a comprehensive review on thermogravimetry analysis, Cellulose. 30 (2023) 2753–2770. https://doi.org/10.1007/s10570-023-05080-4.

[19] T.R. Crompton, Thermogravimetric Analysis, in: Thermal Methods of Polymer Analysis, first ed., ISmithers Rapra Publishing, Shrewsbury, 2013: pp. 37–46.

[20] N. Saba, M. Jawaid, O.Y. Alothman, M.T. Paridah, A review on dynamic mechanical properties of natural fibre reinforced polymer composites, Constr Build Mater. 106 (2016) 149–155. https://doi.org/10.1016/j.conbuildmat.2015.12.075.

[21] M.A. Bashir, Use of Dynamic Mechanical Analysis (DMA) for Characterizing Interfacial Interactions in Filled Polymers, Solids. 2 (2021) 108–120. https://doi.org/10.3390/SOLIDS2010006.

[22] D. Dunson, Characterization of Polymers using Dynamic Mechanical Analysis (DMA), Material Science. (2017) 1–8. https://www.eag.com/wp-content/uploads/2017/09/M-022717-Characterization-of-Polymers-using-Dynamic-Mechanical-Analysis.pdf (accessed July 5, 2023).

[23] K.P. Menard, N.R. Menard, Dynamic Mechanical Analysis; Third Edition, third ed., CRC Press, Boca Raton, 2020.

[24] D. Ratna, Thermal properties of thermosets, in: Guo Q (Ed.), Thermosets: Structure, Properties and Applications, first ed., Woodhead Publishing, Cambridge, 2012: pp. 62–70. https://doi.org/10.1533/9780857097637.1.62.

[25] Mettler Toledo, Essential Applications for the Thermal Analysis of Polymers, (2023) 1–14. https://www.mt.com/in/en/home/library/applications/lab-analytical-instruments/thermal-analysis-of-polymers.html (accessed May 6, 2023).

[26] C. Schick, Differential scanning calorimetry (DSC) of semicrystalline polymers, Anal Bioanal Chem. 395 (2009) 1589–1611. https://doi.org/10.1007/s00216-009-3169-y.

[27] I. Fraga, S. Montserrat, J.M. Hutchinson, TOPEM, a new temperature modulated DSC technique: Application to the glass transition of polymers, J Therm Anal Calorim. 87 (2007) 119–124. https://doi.org/10.1007/S10973-006-7969-4/METRICS.

[28] Khan Academy, What is thermal conductivity?, (2017). https://www.khanacademy.org/science/physics/thermodynamics/specific-heat-and-heat-transfer/a/what-is-thermal-conductivity (accessed June 7, 2023).

[29] H. Chen, V. V. Ginzburg, J. Yang, Y. Yang, W. Liu, Y. Huang, L. Du, B. Chen, Thermal conductivity of polymer-based composites: Fundamentals and applications, Prog Polym Sci. 59 (2016) 41–85. https://doi.org/10.1016/j.progpolymsci.2016.03.001.

[30] J.M. Choung, S.R. Cho, Study on true stress correction from tensile tests, Journal of Mechanical Science and Technology. 22 (2008) 1039–1051. https://doi.org/10.1007/s12206-008-0302-3.

[31] J. Wang, PVT Properties of Polymers for Injection Molding, Some Critical Issues for Injection Molding. (2012) 1–11. https://doi.org/10.5772/35212.

[32] J. Wang, C. Hopmann, C. Kahve, T. Hohlweck, J. Alms, Measurement of specific volume of polymers under simulated injection molding processes, Mater Des. 196 (2020) 1–11. https://doi.org/10.1016/j.matdes.2020.109136.

[33] S.A. Suárez, A. Naranjo, I.D. López, J.C. Ortiz, Analytical review of some relevant methods and devices for the determination of the specific volume on thermoplastic polymers under processing conditions, Polym Test. 48 (2015) 215–231. https://doi.org/10.1016/j.polymertesting.2015.10.009.

[34] J. Wang, C. Hopmann, M. Schmitz, T. Hohlweck, J. Wipperfürth, Modeling of pvT behavior of semi-crystalline polymer based on the two-domain Tait equation of state for injection molding, Mater Des. 183 (2019) 1–10. https://doi.org/10.1016/j.matdes.2019.108149.

[35] E. Sasimowski, Ł. Majewski, T. Jachowicz, M. Sąsiadek, Experimental determination of coefficients for the Renner model of the thermodynamic equation of state of the poly(Butylene succinate) and wheat bran biocomposites, Materials. 14 (2021) 1–11. https://doi.org/10.3390/ma14185293.

[36] T. Jachowicz, I. Gajdos, V. Krasinskiy, Numerical Modeling of p-v-T Rheological Equation Coefficients for Polypropylene with Variable Chalk Content, Open Engineering. 9 (2020) 668–674. https://doi.org/10.1515/eng-2019-0076.

LIST OF FIGURES

TABLE LIST

LIST OF SYMBOLS USED

A - area of the plate
C_p - specific heat capacity
E - modulus of elasticity
E' - storage modulus
E'' - loss modulus
E^* - complex modulus
F - an external force
f - correction factor accounting for the latent heat of fusion with temperature increase
$\dot{\gamma}$ - shear rate
η - viscosity
η_0 - zero-shear rate viscosity
k - thermal conductivity in Fourier's law of heat conduction
$K(t)$ - non-isothermal crystallization rate constant
λ - thermal conductivity
m - mass
n - power law index
N_2 - Nitrogen
O_2 - Oxygen
Q - heat
R - universal gas constant
σ_M - tensile strength
t - time
T - temperature
T_c - crystallization temperature
T_g - glass transition temperature
T_m - melting temperature
T_∞ - the temperature at which the crystallization stops
τ_{xy} - *shear stress*
τ^* - critical shear stress
τ_y - yield stress
$t_{1/2}$ - crystallization half time
U^* - activation energy of the crystallising units to transport across the phase boundary
V - velocity
x - thickness
Y - the distance between plates
ΔH_c - enthalpy of crystallization
ΔH_m - enthalpy of melting
$\triangle T$ - temperature change
ε_B - elongation at break
ε_M - elongation at tensile strength
$tan\ \delta$ - phase angle

LIST OF ABBREVIATIONS USED

ABS - Acrylonitrile butadiene styrene
ASA - Acrylonitrile styrene acrylate
CT - Computerised tomography
CV - Coefficient of variation
DNA - Deoxyribonucleic acid
DSC - Differential scanning calorimetry
DSC TOPEM – Temperature modulated differential scanning calorimetry technique
DTA - Differential thermal analysis
DTG - Derivative thermogravimetry
GF - Glass fibre
HPCR - High-pressure capillary rheometer
IM - Injection moulding
MFR - Melt flow rate
MTPS - Modified transient plane source method
MVR - Melt volume rate
PA - Polyamide
PC - Polycarbonate
PE - Polyethylene
PET - Polyethylene terephthalate
PMMA - Polymethyl methacrylate
PP - Polypropylene
PS - Polystyrene
PVT - Pressure-Volume-Temperature
RNA - Ribonucleic acid
TDS - Technical datasheet
TGA - Thermogravimetric analysis
TTS - Time-temperature superposition

APPENDIX

The appendices in the master's thesis provide additional information and data regarding the measurements and Moldex3D material card data and a comprehensive understanding of the discussed topics. The Appendix titles are:

- Appendix 1: Material Card Data.
- Appendix 2: Tensile Test Graphs.
- Appendix 3: DSC Results.
- Appendix 4: DSC TOPEM Results.
- Appendix 5: Material Card Data Comparison With Other PA66 GF30 Material Cards.
- Appendix 6: Measured Features of Both Housing Parts
- Appendix 7: Comparison of IM Simulation Results With Measured Part Dimensions.

Appendix 1: Material Card Data

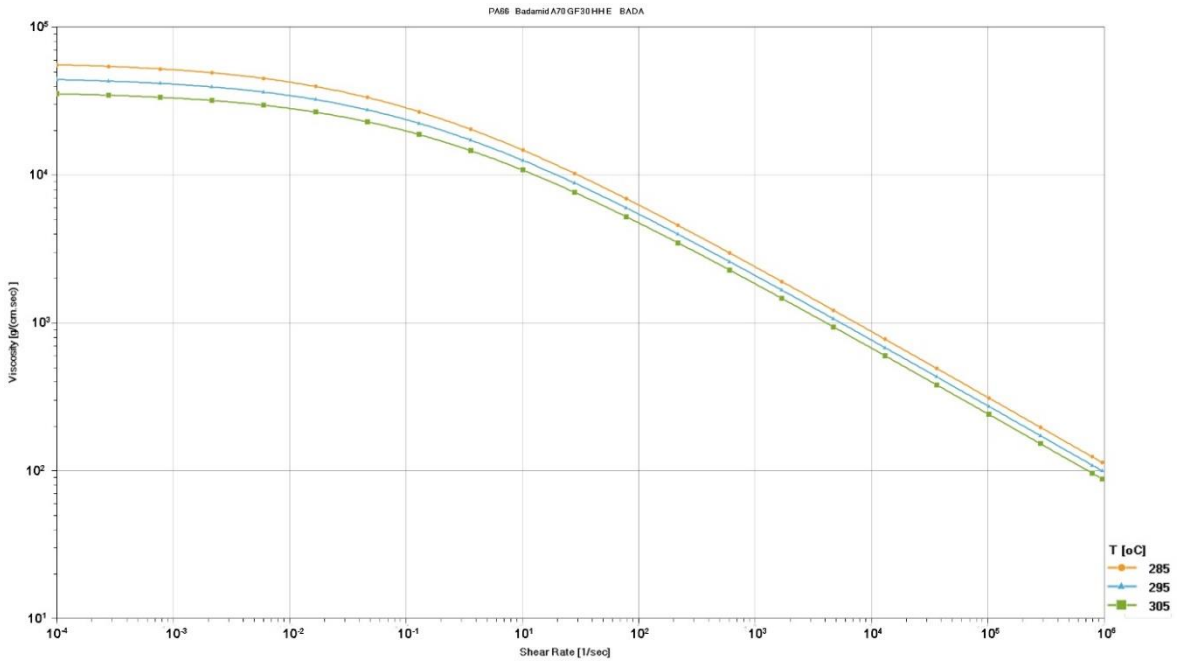

Figure 78: Viscosity as a Function of Shear Rate

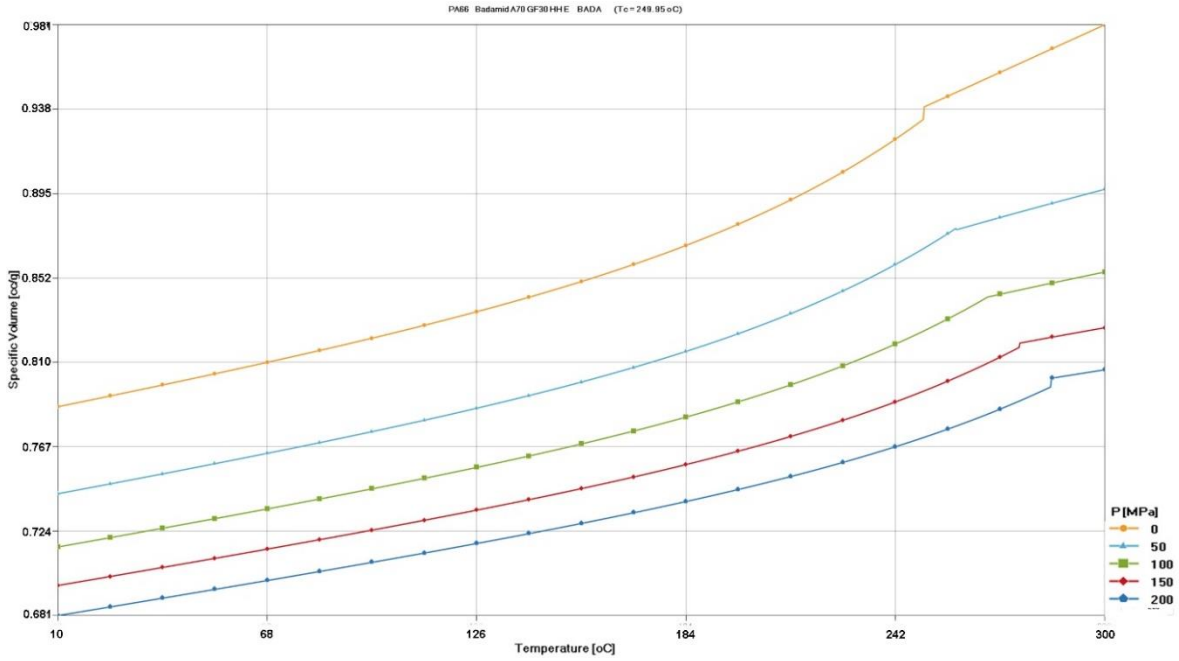

Figure 79: PVT Diagram

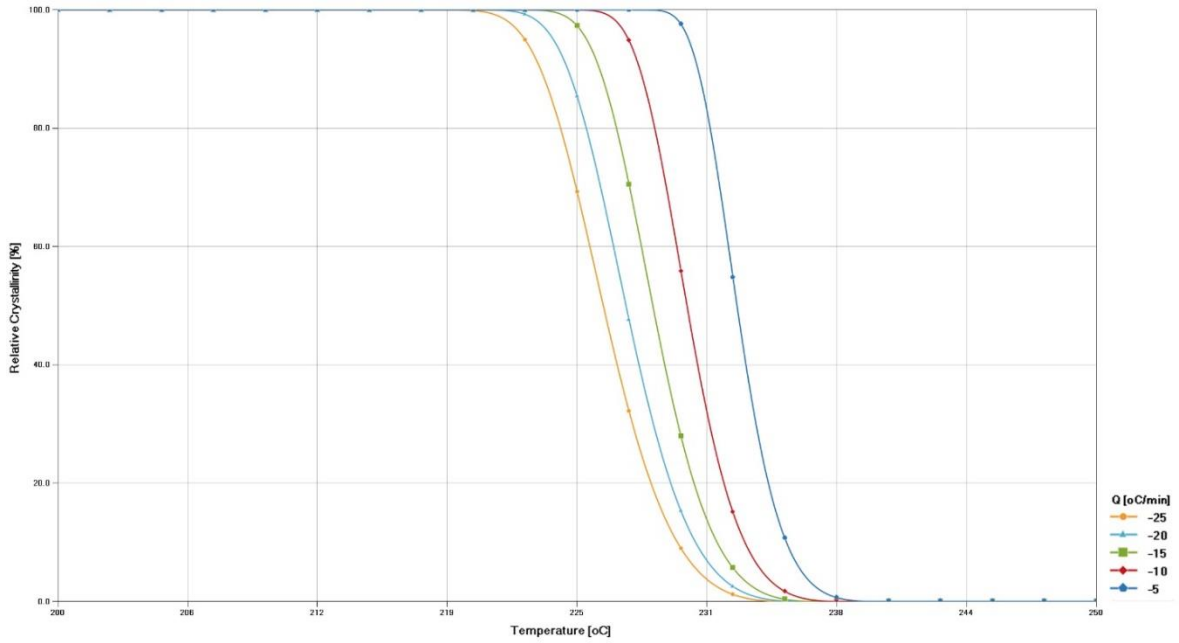

Figure 80: Relative Crystallinity as a Function of Temperature

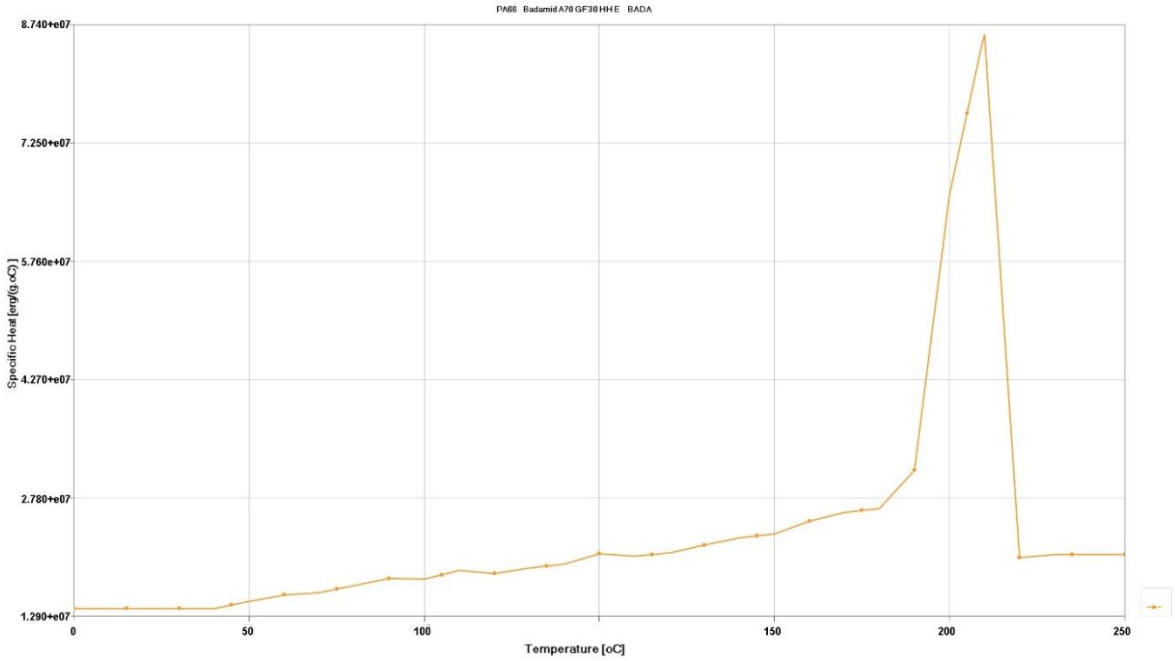

Figure 81: Specific Heat as a Function of Temperature

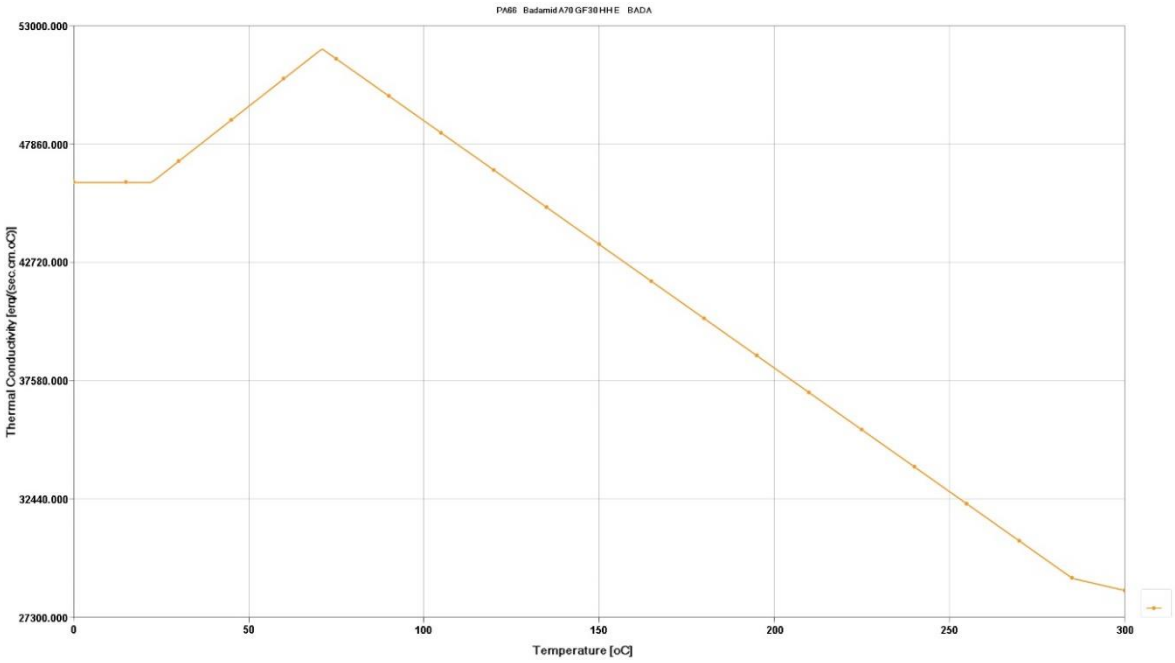

Figure 82: Thermal Conductivity as a Function of Temperature

Appendix 2: Tensile Test Graphs

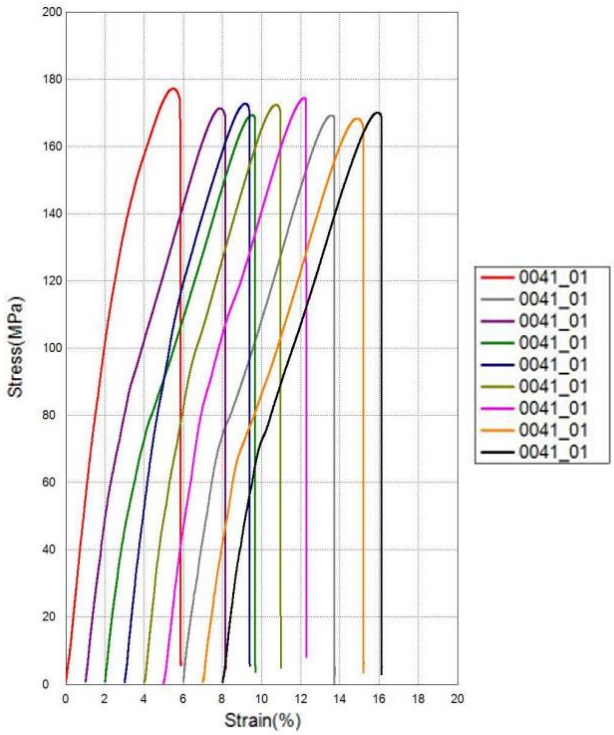

Figure 83: Tensile Test Results for Sample 01

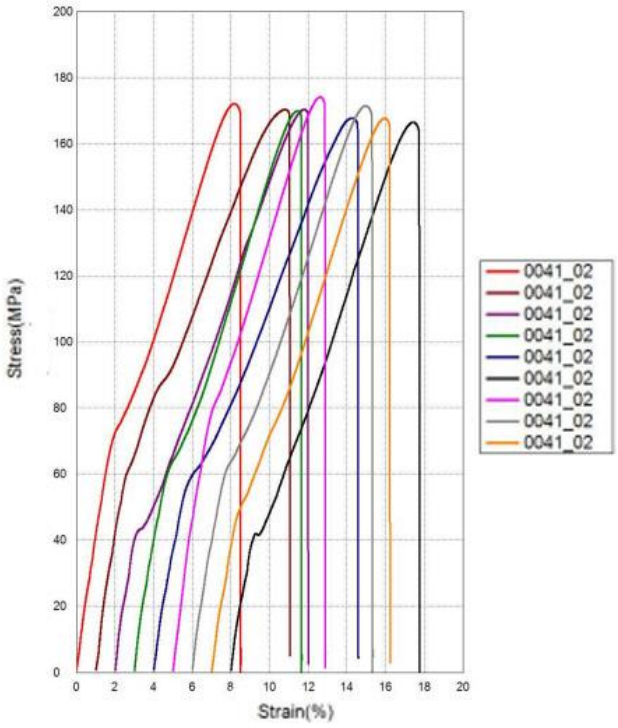

Figure 84: Tensile Test Results for Sample 02

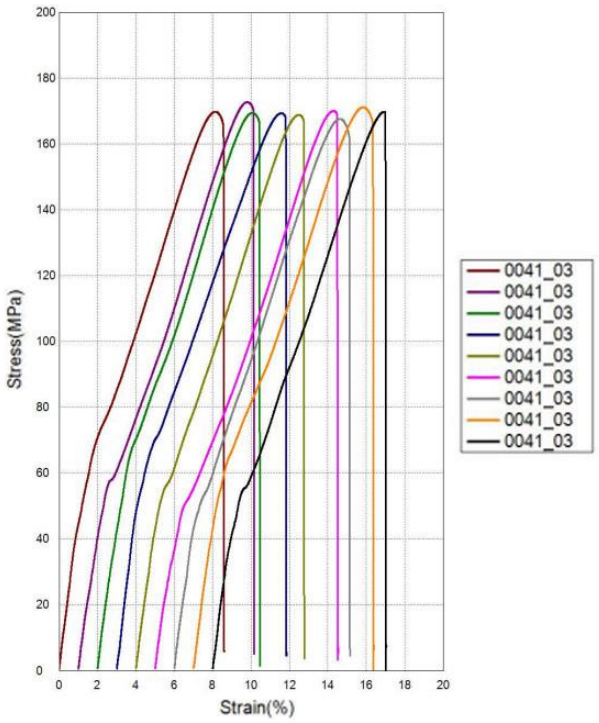

Figure 85: Tensile Test Results for Sample 03

Appendix 3: DSC Results

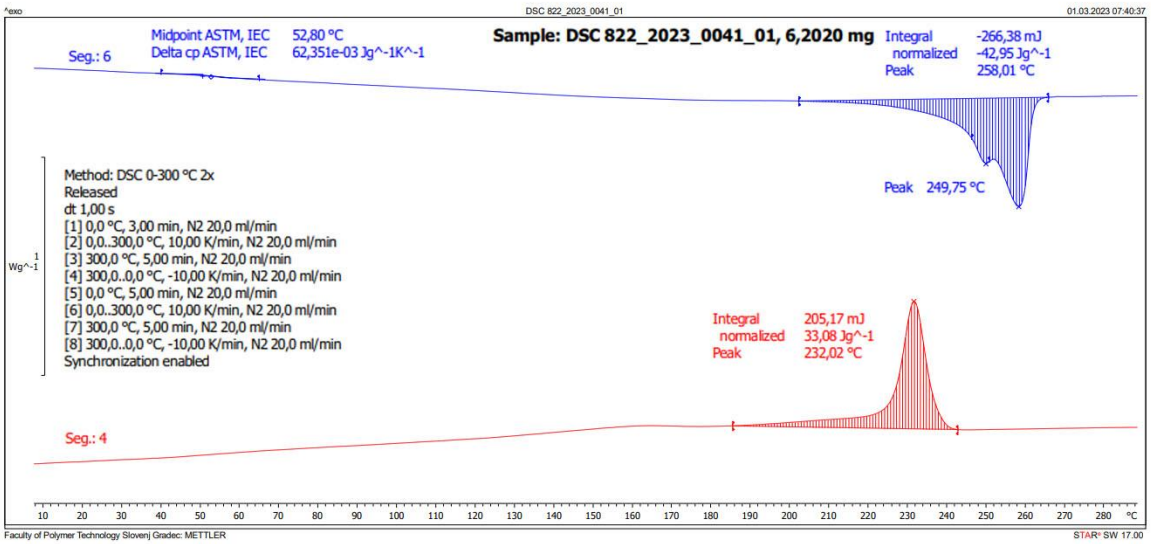

Figure 86: DSC Scan of Sample 01

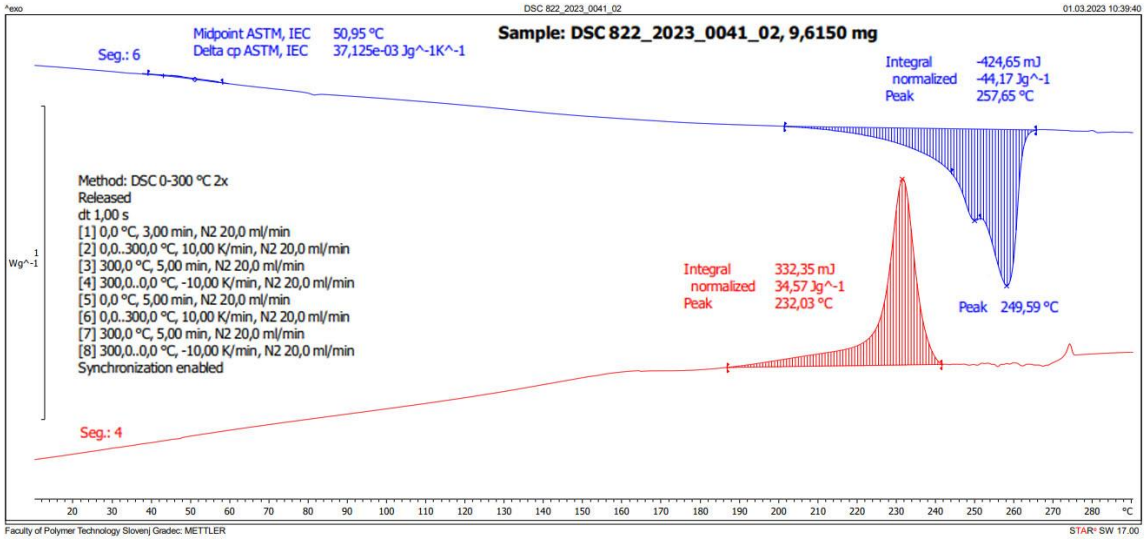

Figure 87: DSC Scan of Sample 02

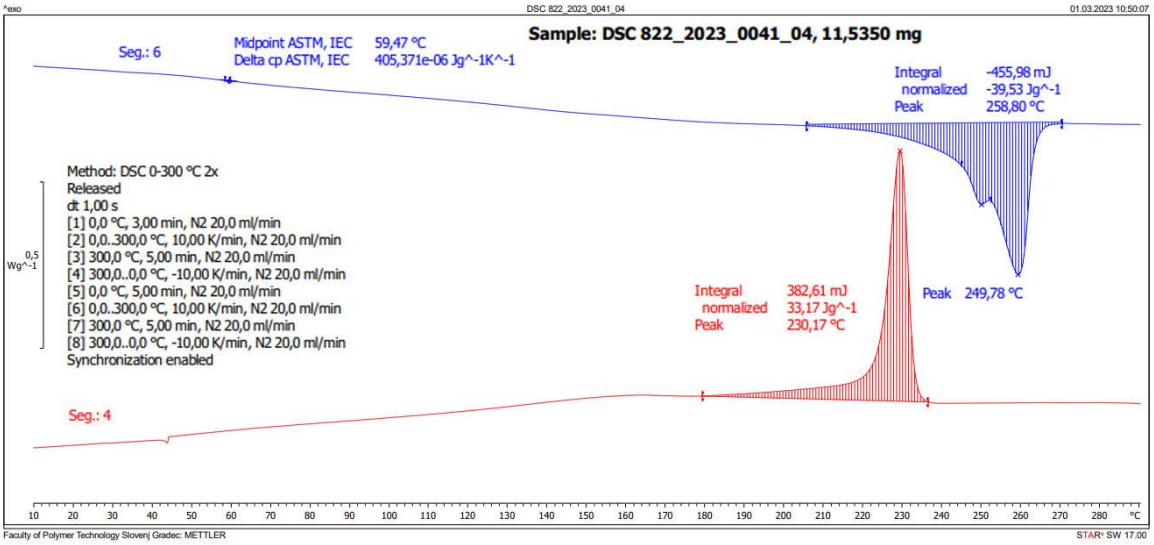

Figure 88: DSC Scan of Sample 04

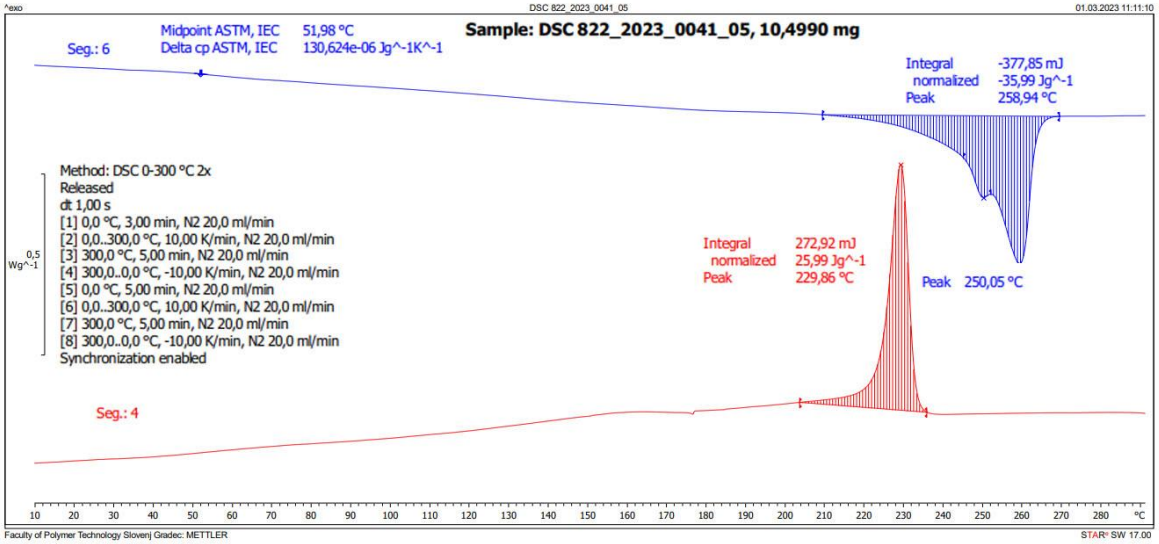

Figure 89: DSC Scan of Sample 05

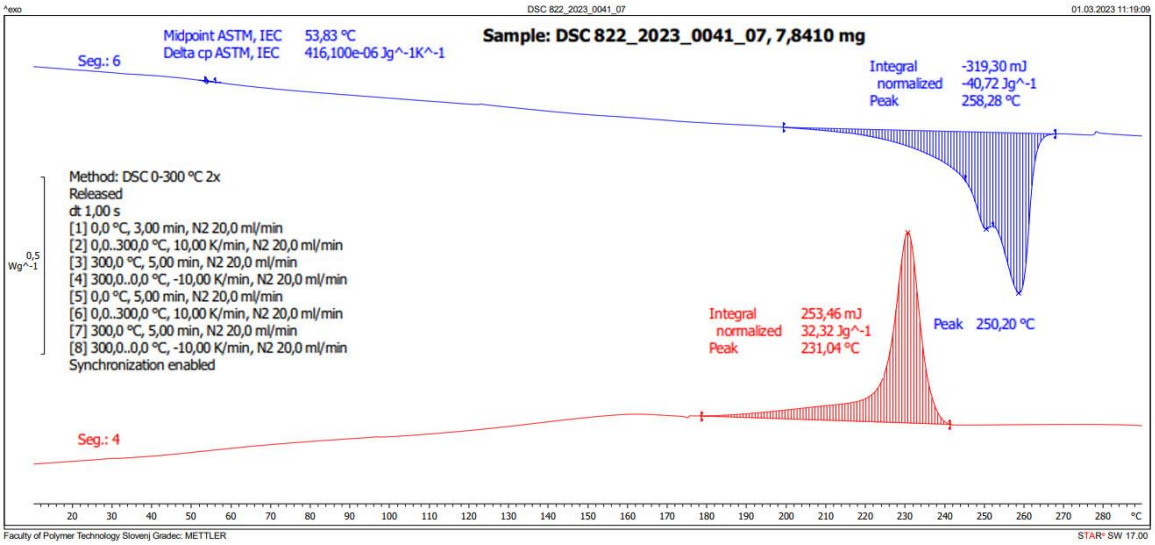

Figure 90: DSC Scan of Sample 07

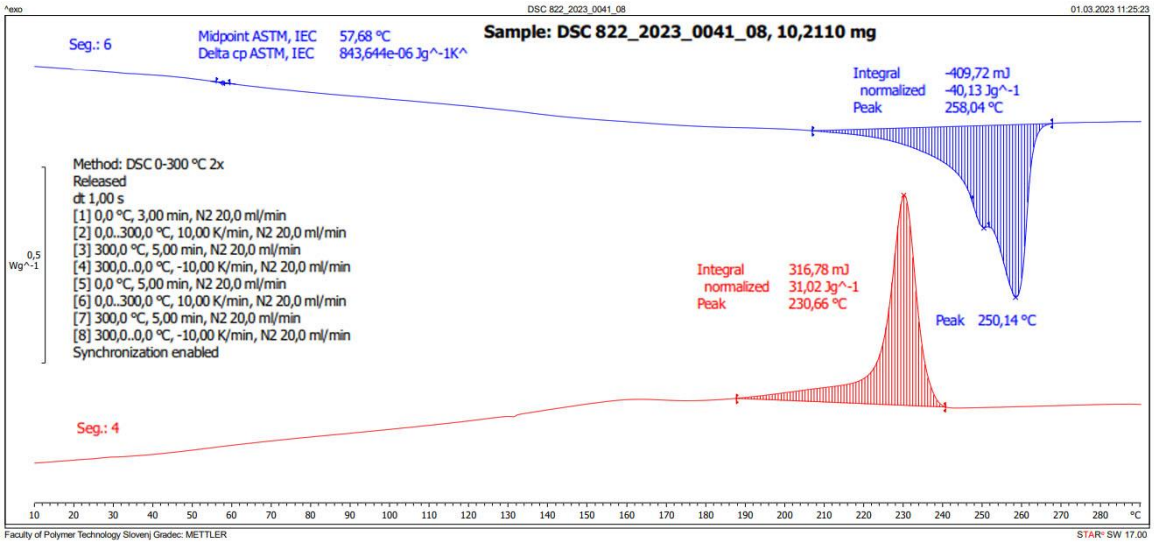

Figure 91: DSC Scan of Sample 08

Appendix 4: DSC TOPEM Results

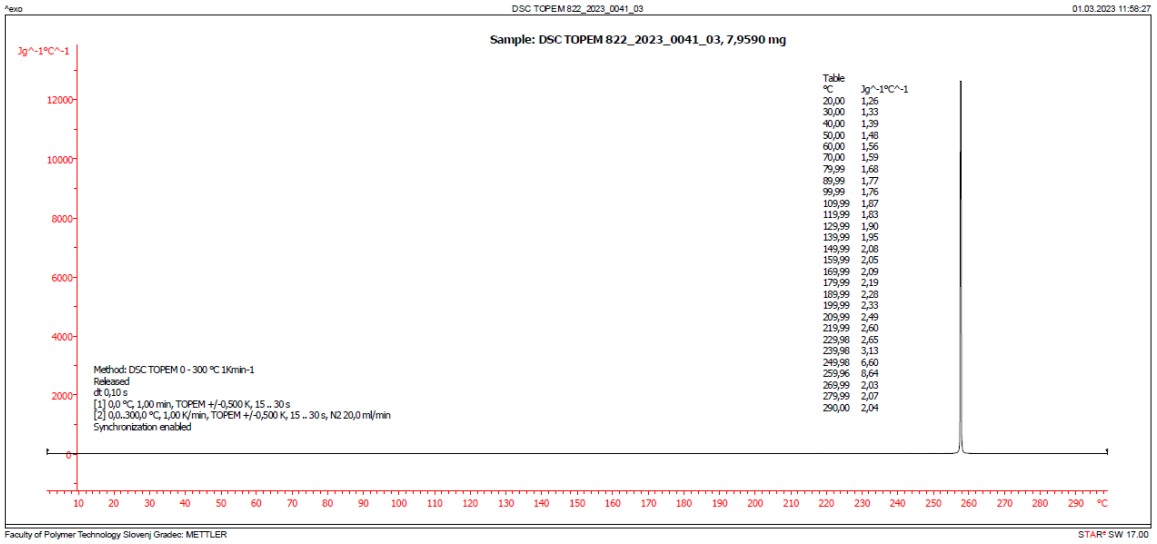

Figure 92: DSC TOPEM Specific Heat Capacity Measurement for Sample 03

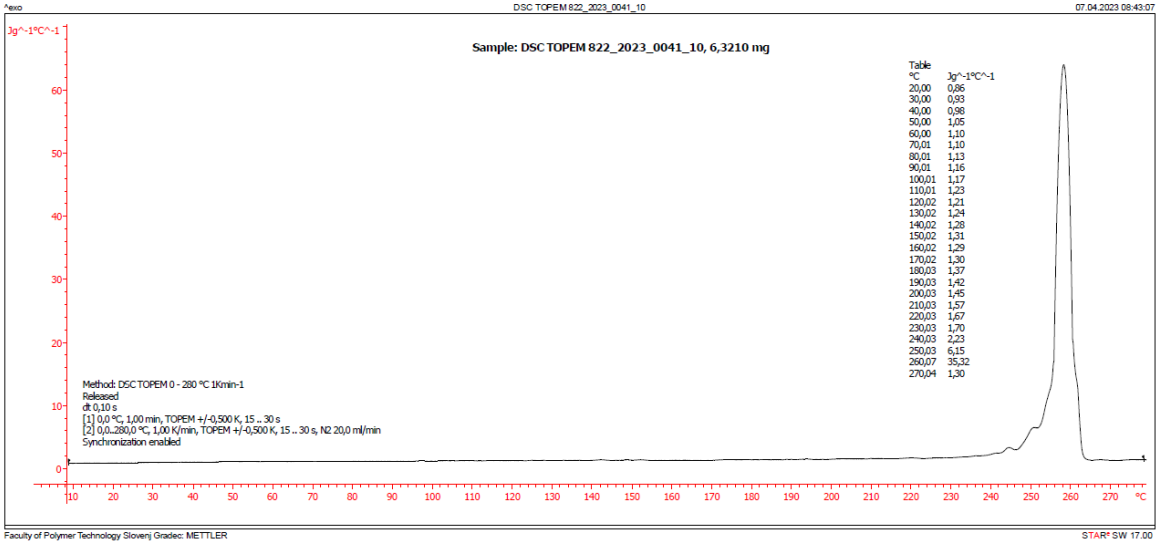

Figure 93: DSC TOPEM Specific Heat Capacity Measurement for Sample 10

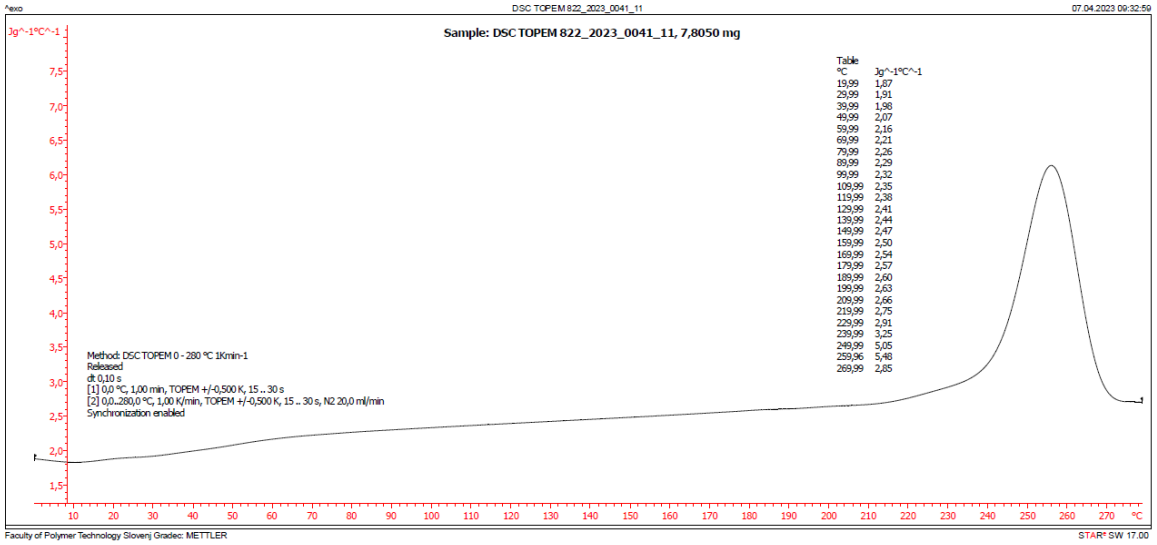

Figure 94: DSC TOPEM Specific Heat Capacity Measurement for Sample 11

Appendix 5: Material Card Comparison With Alternate Material Cards

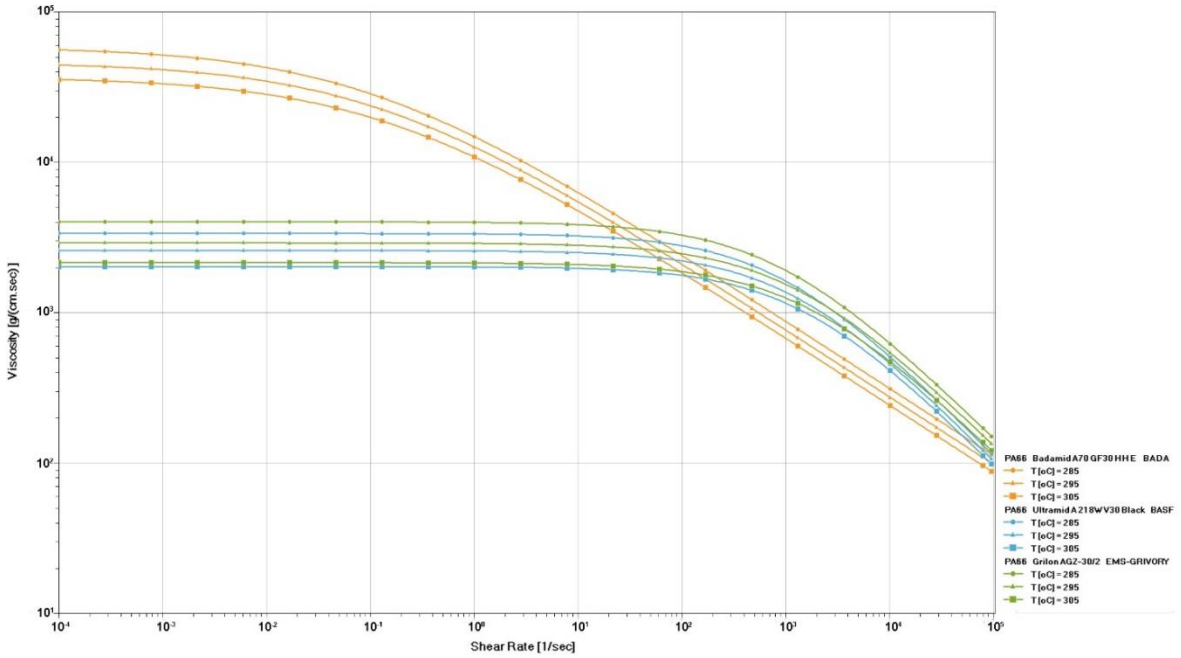

Figure 95: Comparison of Viscosity Curves of Three Different PA66 Types

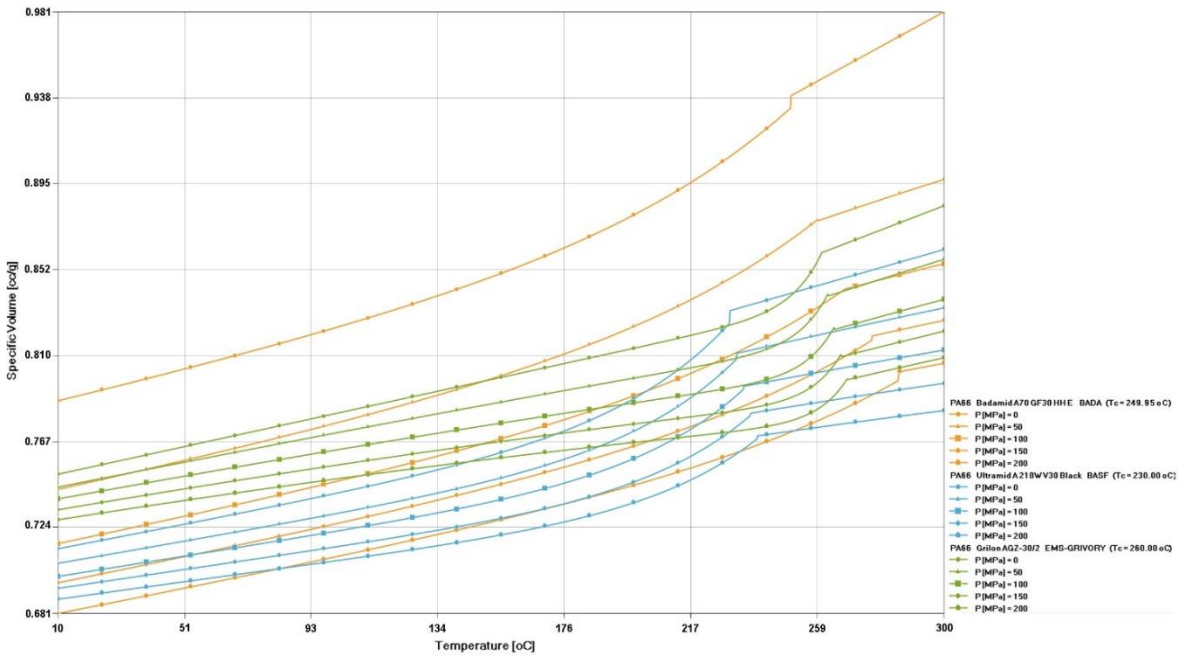

Figure 96: Comparison of the PVT-Diagrams of Three Different PA66 Types

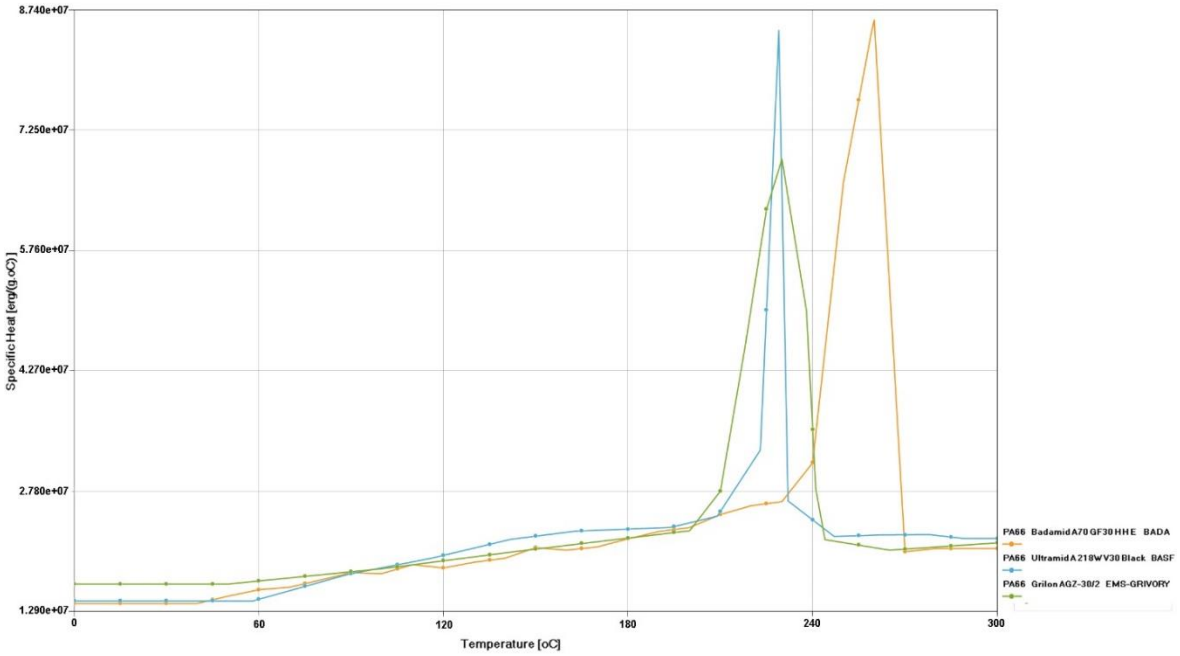

Figure 97: Comparison of Specific Heat Curves of Three Different PA66 Types

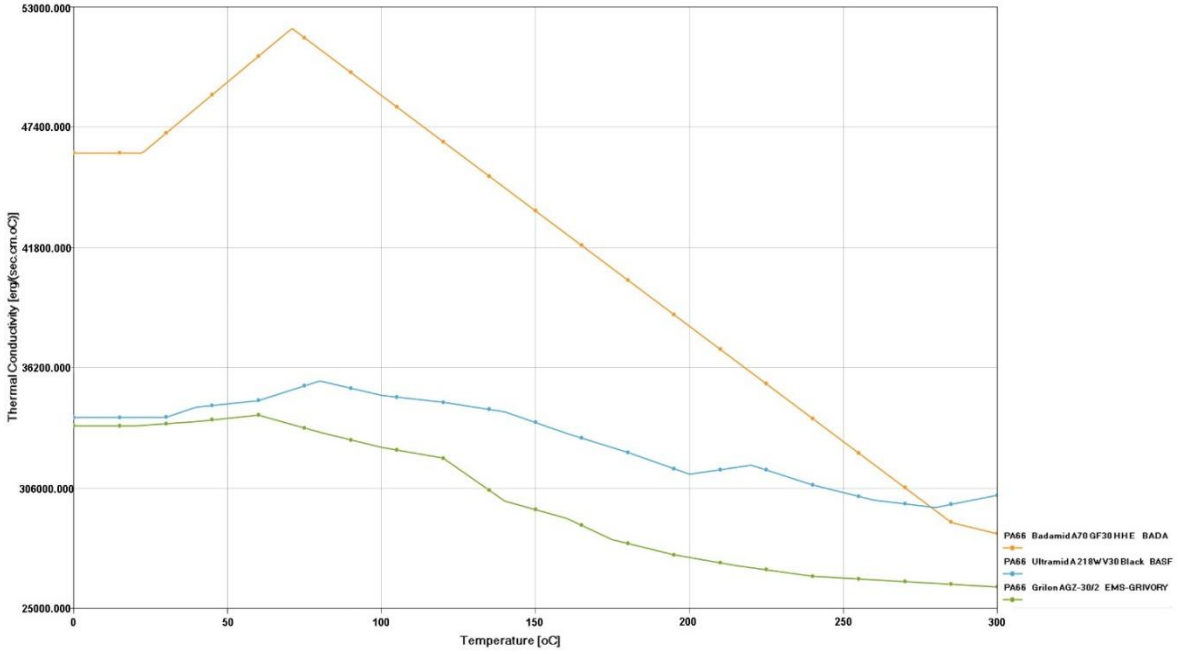

Figure 98: Comparison of Thermal Conductivity of Three Different PA66 Types

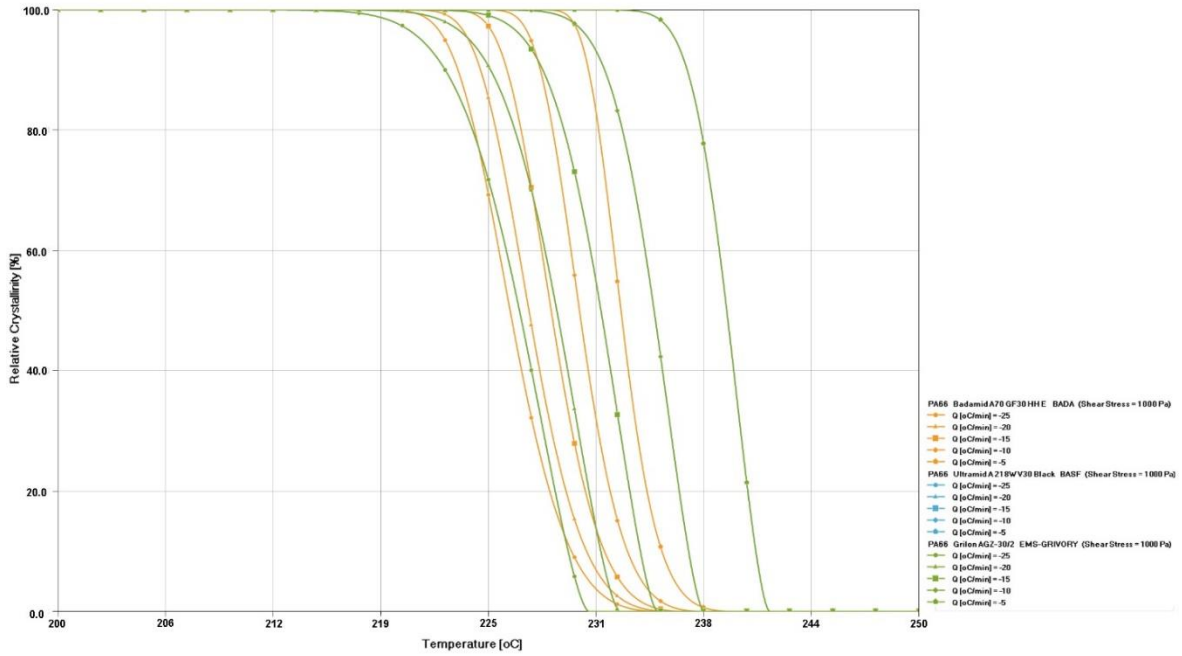

Figure 99: Comparison of Relative Crystallinity Curves of Three Different PA66 Types

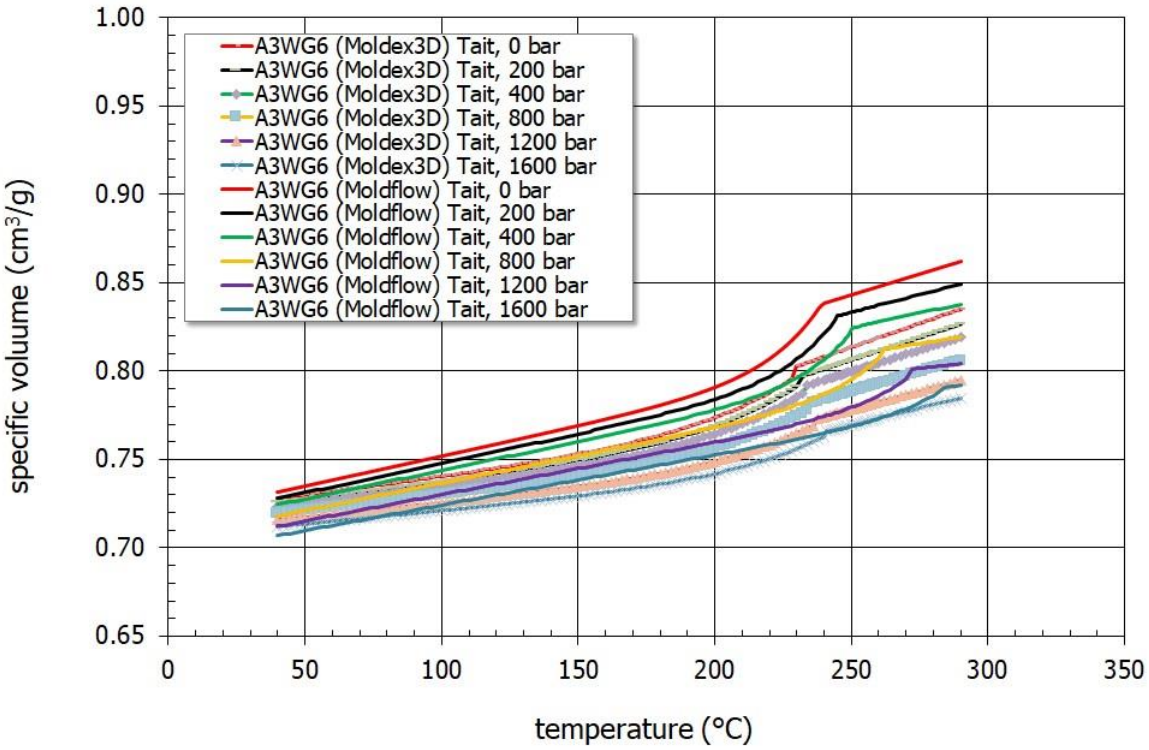

Figure 100: Ultramid A3WG6 Moldex3D vs. Moldflow PVT Data

Appendix 6: Measured Features of Both Housing Parts

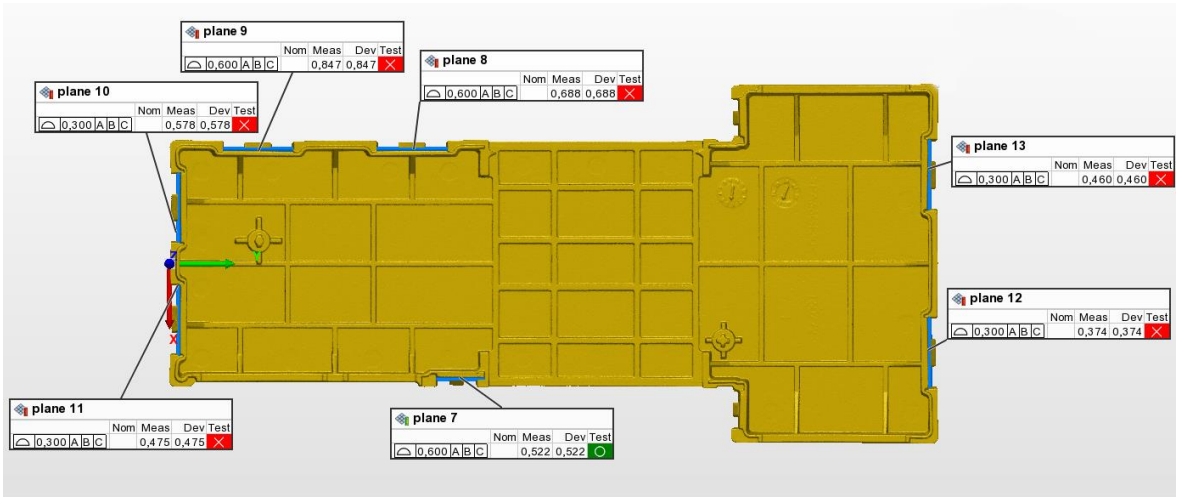

Figure 101: Control View 1 for the Lower Housing

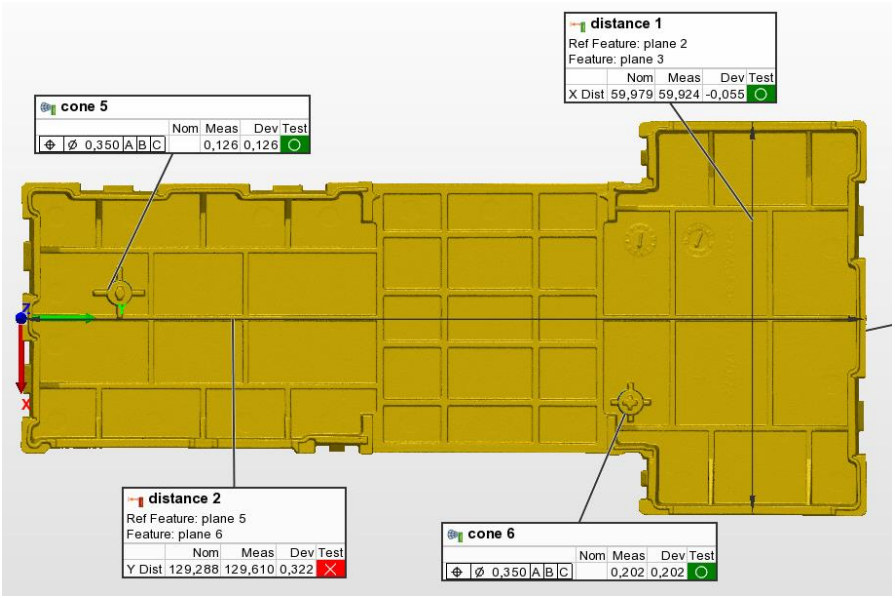

Figure 102: Control View 2 for the Lower Housing

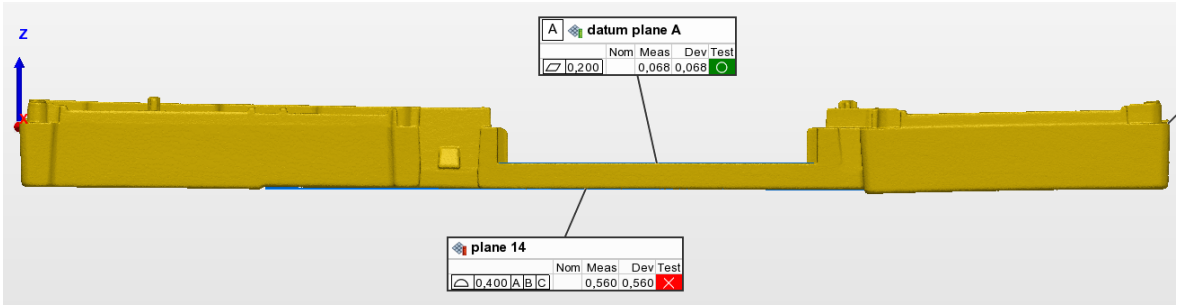

Figure 103: Control View 3 for the Lower Housing

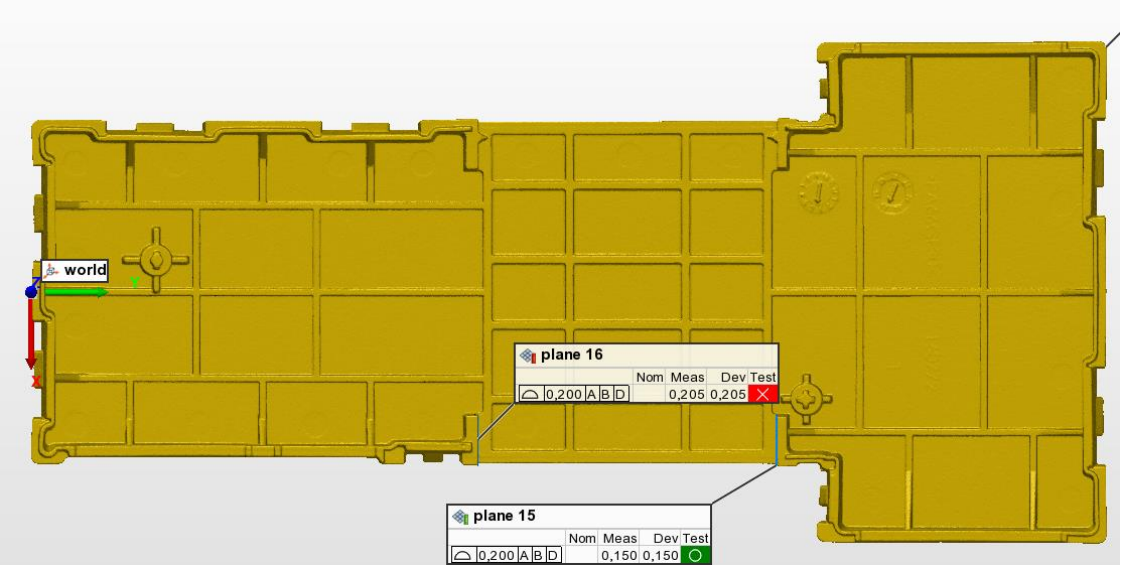

Figure 104: Control View 4 for the Lower Housing

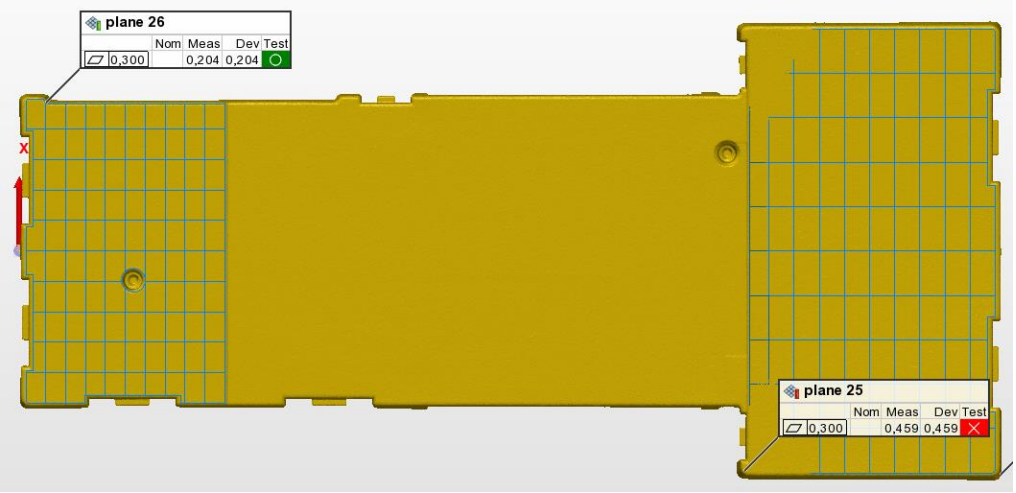

Figure 105: Control View 5 for the Lower Housing

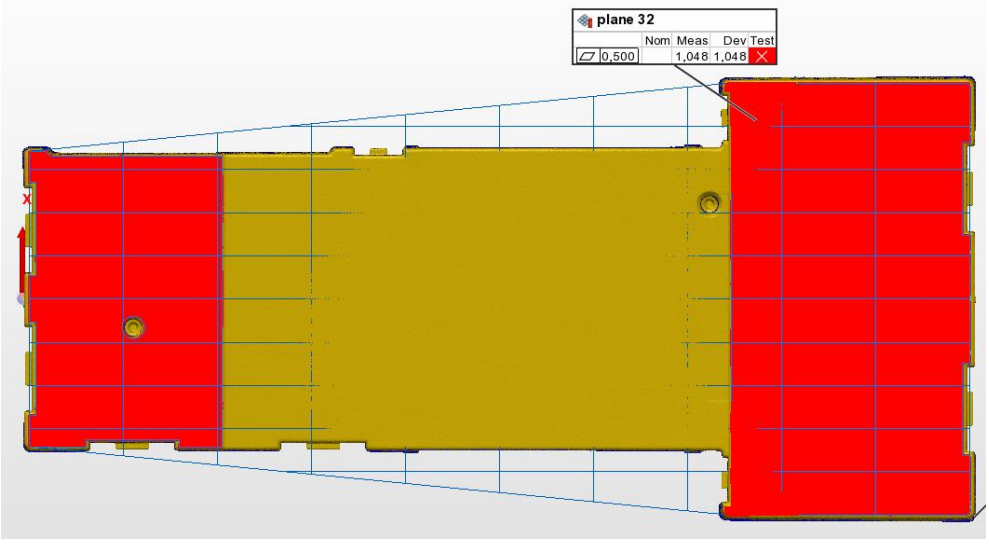

Figure 106: Control View 6 for the Lower Housing

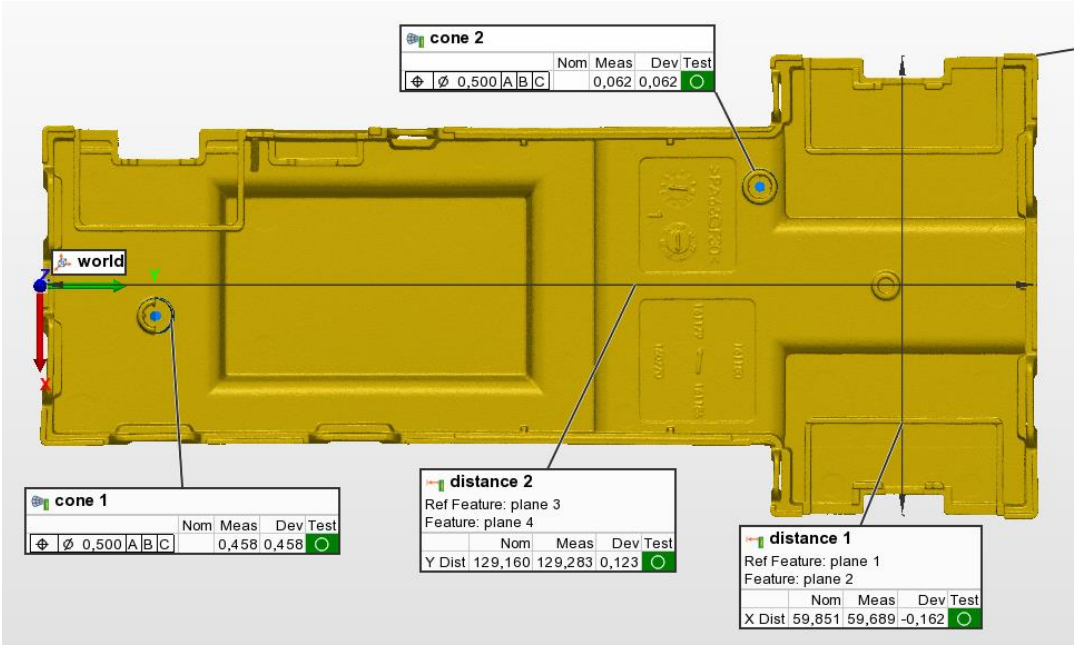

Figure 107: Control View 1 for Upper Housing

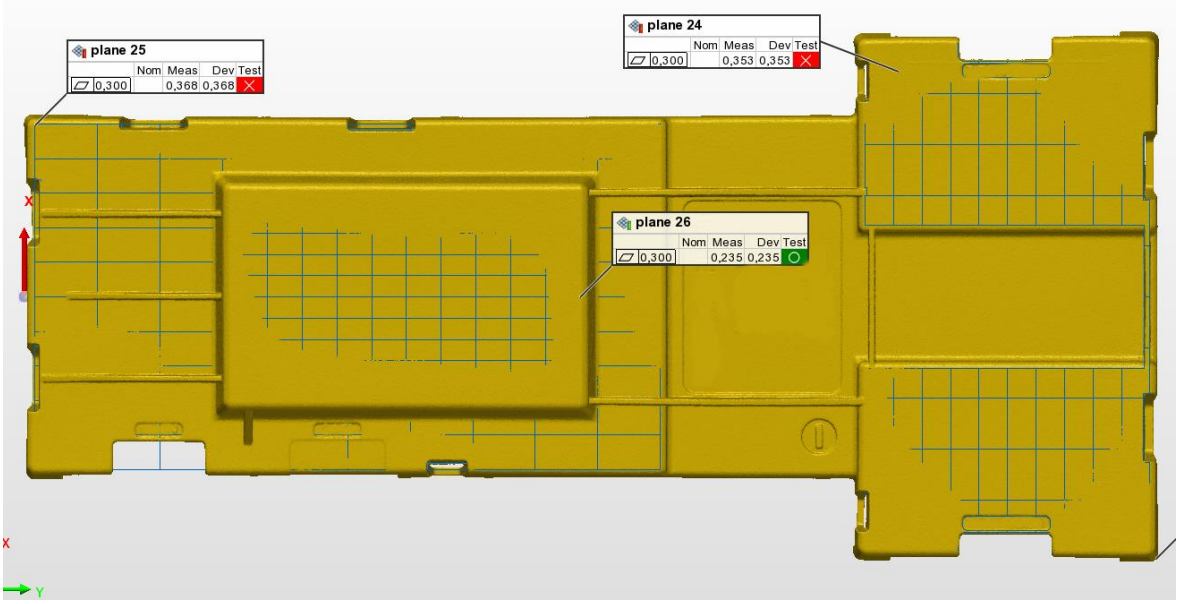

Figure 108: Control View 2 for Upper Housing

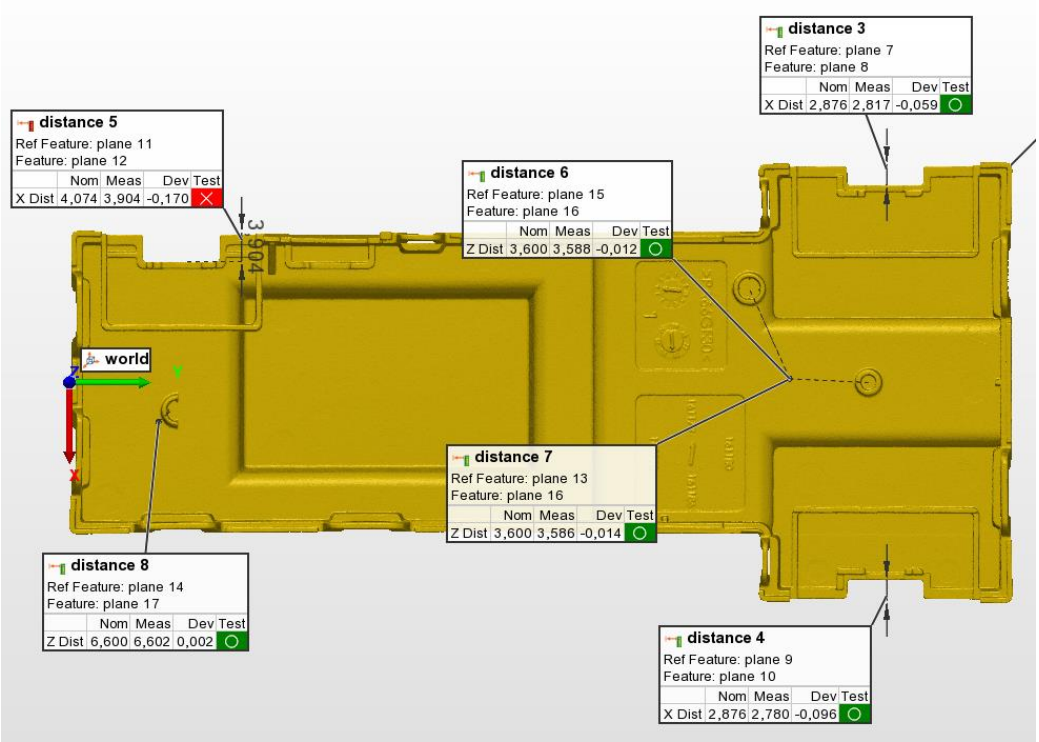

Figure 109: Control View 3 for the Upper Housing

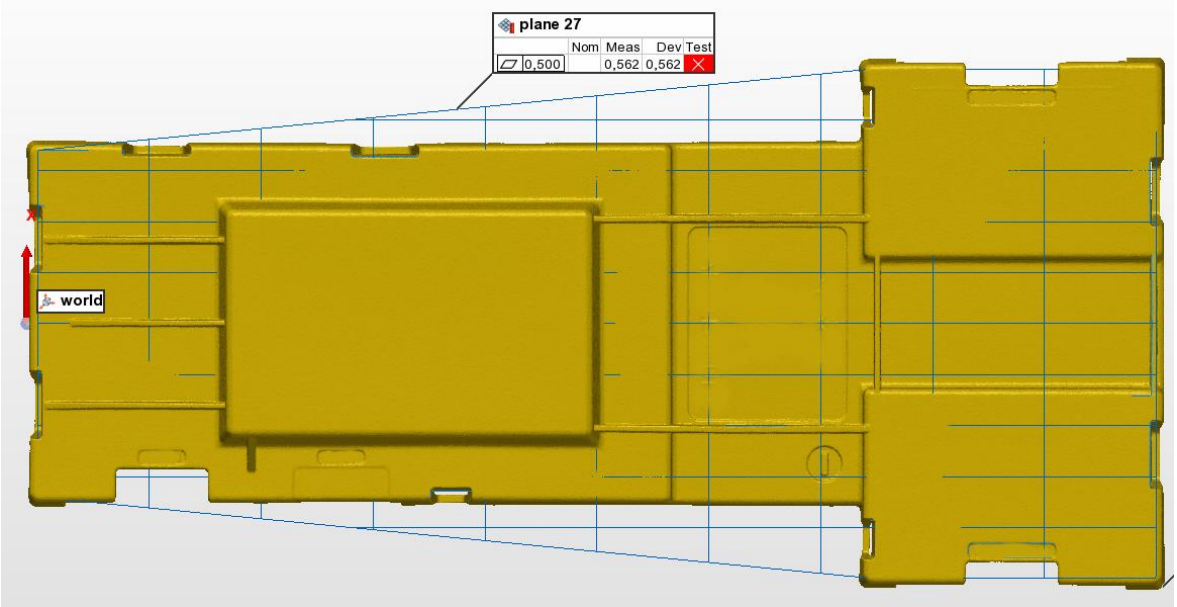

Figure 110: Control View 4 for the Upper Housing

Appendix 7: Comparison of IM Simulation Results With Measured Part Dimensions

Table 28: Measurements Results for the Upper Housing

Object	Control [mm]	Nominal Value [mm]	Tolerance [mm]	IM Badamid A70 GF30 HH E Cavity 1 [mm]	IM Badamid A70 GF30 HH E Cavity 2 [mm]
Distance 1	X Distance	59.851	±0.200	59.689	59.660
Distance 2	Y Distance	129.160	±0.200	129.283	129.261
Cone 1	Position A B C	/	0.500	0.458	0.428
Cone 2	Position A B C	/	0.500	0.062	0.087
Datum Plane A	Flatness	/	0.170	0.433	0.474
Distance 3	X Distance	2.876	±0.100	2.817	2.810
Distance 4	X Distance	2.876	±0.100	2.780	2.768
Distance 5	X Distance	4.074	±0.100	3.904	3.906
Distance 6	Z Distance	3.600	±0.100	3.588	3.555
Distance 7	Z Distance	3.600	±0.100	3.586	3.650
Distance 8	Z Distance	6.600	±0.100	6.602	6.620
Plane 24	Flatness	/	0.300	0.353	0.362
Plane 25	Flatness	/	0.300	0.368	0.378
Plane 26	Flatness	/	0.300	0.235	0.249
Plane 27	Flatness	/	0.500	0.562	0.540

Table 29: Measurements Results for the Lower Housing

Object	Control [mm]	Nominal Value [mm]	Tolerance [mm]	IM Badamid A70 GF30 HH E Cavity 1 [mm]	IM Badamid A70 GF30 HH E Cavity 2 [mm]
Datum Plane A	Flatness		0.200	0.068	0.083
Distance 1	X Distance	59.979	±0.200	59.924	59.874
Distance 2	Y Distance	129.288	±0.200	129.610	129.542
Plane 7	Surface Profile A B C	/	0.600	0.522	0.483
Plane 8	Surface Profile A B C	/	0.600	0.688	0.713
Plane 9	Surface Profile A B C	/	0.600	0.847	0.843
Plane 10	Surface Profile A B C	/	0.300	0.578	0.567
Plane 11	Surface Profile A B C	/	0.300	0.475	0.477
Plane 12	Surface Profile A B C	/	0.300	0.374	0.300
Plane 13	Surface Profile A B C	/	0.300	0.460	0.419
Plane 14	Surface Profile A B C	/	0.400	0.560	0.567
Plane 15	Surface Profile A B D	/	0.200	0.150	0.167
Plane 16	Surface Profile A B D	/	0.200	0.205	0.271
Plane 25	Flatness	/	0.300	0.459	0.448
Plane 26	Flatness	/	0.300	0.204	0.236
Plane 32	Flatness	/	0.500	1.048	1.045
Cone 5	Position A B C	/	0.350	0.126	0.121
Cone 6	Position A B C	/	0.350	0.202	0.276

Table 30: IM Simulation Dimension Results of the Upper Housing; Part 1

Object	Control [mm]	Nominal Value [mm]	Tolerance [mm]	Ultramid A3WG6 – Moldex PVT [mm]	Ultramid A3WG6 – Moldflow PVT [mm]	Ultramid A218W V30 [mm]
Distance 1	X Distance	59.851	±0.200	59,603	59,603	59,533
Distance 2	Y Distance	129.160	±0.200	129,005	129,005	128,874
Cone 1	Position A B C	/	0.500	0,103	0,103	0,218
Cone 2	Position A B C	/	0.500	0,178	0,178	0,21
Datum Plane A	Flatness	/	0.170	0,114	0,114	0,124
Distance 3	X Distance	2.876	±0.100	2,9	2,9	2,894
Distance 4	X Distance	2.876	±0.100	2,904	2,904	2,898
Distance 5	X Distance	4.074	±0.100	4,049	4,049	4,042
Distance 6	Z Distance	3.600	±0.100	3,548	3,548	3,539
Distance 7	Z Distance	3.600	±0.100	3,493	3,493	3,491
Distance 8	Z Distance	6.600	±0.100	6,603	6,603	6,602
Plane 24	Flatness	/	0.300	0,244	0,244	0,257
Plane 25	Flatness	/	0.300	0,131	0,131	0,134
Plane 26	Flatness	/	0.300	0,06	0,06	0,064
Plane 27	Flatness	/	0.500	0,252	0,252	0,277

Table 31: IM Simulation Dimension Results of the Upper Housing; Part 2

Object	Control [mm]	Nominal Value [mm]	Tolerance [mm]	Badamid A70 GF30 HH E – mod PVT With Reference Rel. Crystallinity [mm]	Badamid A70 GF30 HH E – A3WG6 PVT With Reference Rel. Crystallinity [mm]	Badamid A70 GF30 HH E – Mod PVT [mm]
Distance 1	X Distance	59.851	±0.200	59,672	59,643	59,481
Distance 2	Y Distance	129.160	±0.200	129,074	129,047	128,875
Cone 1	Position A B C	/	0.500	0,052	0,099	0,195
Cone 2	Position A B C	/	0.500	0,131	0,157	0,228
Datum Plane A	Flatness	/	0.170	0,115	0,109	0,134
Distance 3	X Distance	2.876	±0.100	2,893	2,898	2,903
Distance 4	X Distance	2.876	±0.100	2,896	2,899	2,907
Distance 5	X Distance	4.074	±0.100	4,054	4,054	4,057
Distance 6	Z Distance	3.600	±0.100	3,544	3,536	3,557
Distance 7	Z Distance	3.600	±0.100	3,508	3,501	3,468
Distance 8	Z Distance	6.600	±0.100	6,604	6,602	6,61
Plane 24	Flatness	/	0.300	0,222	0,247	0,334
Plane 25	Flatness	/	0.300	0,115	0,124	0,144
Plane 26	Flatness	/	0.300	0,056	0,055	0,069
Plane 27	Flatness	/	0.500	0,223	0,255	0,339

Table 32: IM Simulation Dimension Results of the Lower Housing; Part 1

Object	Control [mm]	Nominal Value [mm]	Tolerance [mm]	Ultramid A218W V30 [mm]	Ultramid A3WG6 – Moldex PVT [mm]	Ultramid A3WG6 – Moldflow PVT [mm]
Datum Plane A	Flatness	/	0.200	0,123	0,145	0,145
Distance 1	X Distance	59.979	±0.200	59,45	59,532	59,532
Distance 2	Y Distance	129.288	±0.200	128,981	129,084	129,084
Plane 7	Surface Profile A B C	/	0.600	0,281	0,268	0,268
Plane 8	Surface Profile A B C	/	0.600	0,304	0,285	0,285
Plane 9	Surface Profile A B C	/	0.600	0,363	0,347	0,347
Plane 10	Surface Profile A B C	/	0.300	0,599	0,465	0,465
Plane 11	Surface Profile A B C	/	0.300	0,596	0,426	0,426
Plane 12	Surface Profile A B C	/	0.300	0,594	0,438	0,438
Plane 13	Surface Profile A B C	/	0.300	0,599	0,435	0,435
Plane 14	Surface Profile A B C	/	0.400	0,304	0,202	0,202
Plane 15	Surface Profile A B D	/	0.200	0,084	0,052	0,052
Plane 16	Surface Profile A B D	/	0.200	0,262	0,144	0,144
Plane 25	Flatness	/	0.300	0,601	0,612	0,612
Plane 26	Flatness	/	0.300	0,149	0,178	0,178
Plane 32	Flatness	/	0.500	0,648	0,616	0,616
Cone 5	Position A B C	/	0.350	0,357	0,221	0,221
Cone 6	Position A B C	/	0.350	0,229	0,186	0,186

Table 33: IM Simulation Dimension Results of the Lower Housing; Part 2

Object	Control [mm]	Nominal Value [mm]	Tolerance [mm]	Badamid A70 GF30 HH E – Mod PVT [mm]	Badamid A70 GF30 HH E – mod PVT With Reference Rel. Crystallinity [mm]	Badamid A70 GF30 HH E – A3WG6 PVT With Reference Rel. Crystallinity [mm]
Datum Plane A	Flatness	/	0.200	0,193	0,064	0,075
Distance 1	X Distance	59.979	±0.200	59,448	59,648	59,608
Distance 2	Y Distance	129.288	±0.200	128,937	129,21	129,187
Plane 7	Surface Profile A B C	/	0.600	0,376	0,202	0,236
Plane 8	Surface Profile A B C	/	0.600	0,392	0,216	0,258
Plane 9	Surface Profile A B C	/	0.600	0,435	0,261	0,304
Plane 10	Surface Profile A B C	/	0.300	0,511	0,378	0,393
Plane 11	Surface Profile A B C	/	0.300	0,473	0,35	0,368
Plane 12	Surface Profile A B C	/	0.300	0,505	0,351	0,385
Plane 13	Surface Profile A B C	/	0.300	0,496	0,351	0,382
Plane 14	Surface Profile A B C	/	0.400	0,341	0,224	0,151
Plane 15	Surface Profile A B D	/	0.200	0,074	0,055	0,057
Plane 16	Surface Profile A B D	/	0.200	0,144	0,109	0,111
Plane 25	Flatness	/	0.300	0,672	0,493	0,559
Plane 26	Flatness	/	0.300	0,17	0,097	0,103
Plane 32	Flatness	/	0.500	0,672	0,503	0,564
Cone 5	Position A B C	/	0.350	0,258	0,167	0,181
Cone 6	Position A B C	/	0.350	0,249	0,155	0,175